Detector Simulations for the ATHENA X-ray Observatory

Detektorsimulationen für den Athena-Satelliten

Der Naturwissenschaftlichen Fakultät
der Friedrich-Alexander-Universität Erlangen-Nürnberg
zur Erlangung des Doktorgrades Dr. rer. nat.
vorgelegt von

Thorsten Brand

aus Nürnberg

ERLANGEN CENTRE
FOR ASTROPARTICLE
PHYSICS

FRIEDRICH-ALEXANDER
UNIVERSITÄT
ERLANGEN-NÜRNBERG

NATURWISSENSCHAFTLICHE
FAKULTÄT

Als Dissertation genehmigt
von der Naturwissenschaftlichen Fakultät
der Friedrich-Alexander-Universität Erlangen-Nürnberg

Tag der mündlichen Prüfung:	10. Mai 2017

Vorsitzender des Promotionsorgans:	- Prof. Dr. Georg Kreimer
Gutachter:	- Prof. Dr. Jörn Wilms
Gutachter:	- Prof. Dr. Richard Willingale

Abstract

I present the results of detector simulations for the *Athena* mission. *Athena* is a planned X-ray observatory to be launched in 2028. The mission will provide data to give us a better understanding about the evolution of the universe, especially the formation of the large-scale structures.
In our current understanding, structure formation is largely influenced by the so-called dark matter which can not be observed directly by electromagnetic radiation, and the cosmological constant, also known as the dark energy. Together, dark matter and dark energy sum up to more than 95% of the total energy density of the universe. This means that only less than 5% of the energy density is baryonic and can be observed directly using the methods of astronomy. To improve our understanding of the evolution of the universe, *Athena* will perform surveys and deep observations. These allow us to search for undetected intergalactic matter and to give us new information about structure formation and how it is influenced by highly energetic processes.
To achieve these goals, *Athena* will have one large X-ray mirror with an effective area of around $2\,\mathrm{m}^2$ at an energy of 1 keV. *Athena* features two scientific instruments located in the focal plane. The Wide Field Imager (WFI) provides a large field of view of 40' × 40' for the observation of extended sources and surveys and also holds a small, high count-rate capable sensor for observations of bright sources. The second instrument is the X-ray Integral Field Unit (X-IFU), which provides an energy resolution of 2.5 eV for photon energies below 7 keV, at the cost of a smaller field of view of 5' and a slightly worse angular resolution.
In this work I present the implementation of detector effects for both instruments in the SIXTE simulation framework. These effects have an influence on the measured spectra. The resulting implementation is used for different scientific studies performed for the instruments. One of them is to test X-IFU's capability to observe the previously undetected gas filaments between galaxy clusters which are thought to be responsible for the missing 30% of baryonic matter in the local universe. This Warm-Hot Intergalactic Medium (WHIM) can best be found by faint absorption lines in the spectra of bright background sources such as the afterglows of Gamma-Ray Bursts (GRBs). To quantify the X-IFU's capability to detect and measure these lines, SIXTE has been used to simulate a large number of model GRB afterglows with WHIM absorption lines. The resulting data has been analysed using a blind line search. The results show that the mission as planned will be able to identify WHIM filaments using GRB afterglows with a starting flux at the beginning of the observation of more than $3 \times 10^{-11}\,\mathrm{erg\,cm^{-2}\,s^{-1}}$.
In a second study, the capability of the WFI to observe bright sources has been examined. For high count-rates, the basic assumptions for X-ray data reduction fail. Usually, the time between two events at the same pixel of a detector is large enough to separate them by a short-enough frame length. This enables the analysis software to assume that the charge created in a pixel is proportional to only a single photon's energy. However, as the count-

rate increases, the probability of two photons hitting the same spot on the detector in one frame increases, which leads to a confusion of the measured count-rate and photon energy. This effect is known as pile-up and can be limited by an elaborate analysis which rejects certain data patterns. However, this leads to a blinding of the detector at high count-rates. Both the corruption of the energy measurement and the drop in detection efficiency are unwanted detector features which need to be limited. In the study presented in this thesis, I performed simulations for the WFI to describe the count-rate dependent throughput and pile-up behaviour of the sensor. The results show that by mounting the small sensor of the WFI 35 mm out of the focal plane, the detector is able to observe sources with a brightness of around 10 Crab with less than 1% of pile-up and more than 90% of throughput. This position has already been included in the newest design of the instrument.

To help in optimising the implementation of DEPFET-specific detector effects, measurements of two prototype sensors have been conducted. During the read-out of the sensor, each row of pixels is active for a short period. When a photon hits a pixel during this time, the energy measurement is corrupted. The reconstructed energy exhibits a systematic behaviour caused by the implementation of the read-out of a DEPFET. The data taken for the two prototype sensors have been analysed to describe the dependence of the measured energy on the amount of charge induced for a certain interval of the read-out sequence. The results show that during the end of the clear of the read-out, the measured energy rises nearly exponentially from zero to the real energy with an energy dependent time constant. However, a kink during this rise has been identified, such that the whole rise can be described best by the sum of two exponential functions. This knowledge can be taken into account for future improvement of the detector's energy reconstruction algorithms.

Zusammenfassung

In dieser Arbeit stelle ich die Ergebnisse von Detektorsimulationen für die *Athena*-Mission vor. *Athena* ist ein geplantes Röntgenteleskop, welches im Jahr 2028 gestartet werden soll. Die Mission wird uns Daten zum besseren Verständnis über die Entwickling des Universums liefern, insbesondere der Bildung von großräumigen Strukturen.
In unserem aktuellen Verständnis ist die Bildung dieser Strukturen stark von der sogenannten dunklen Materie beeinflusst, die nicht direkt mit Hilfe elektromagnetischer Strahlung beobachtet werden kann, und der kosmologischen Konstante, die besser als dunkle Energie bekannt ist. Zusammen machen die dunkle Materie und Energie mehr als 95% der gesamten Energiedichte des Universums aus. Das bedeutet, dass nur weniger als 5% der Energiedichte baryonisch ist und damit direkt mit den Methoden der Astronomie beobachtet werden kann. Um unser Verständnis für die Entwicklung des Universums zu verbessern, wird *Athena* großräumige und tiefe Beobachtungen durchführen. Dies erlaubt es uns, nach bislang undetektierter Materie im intergalaktischen Raum zu suchen, und neue Informationen über die Strukturbildung im Universum und die Rolle von hochenergetischen Prozessen zu erhalten.
Um diese Ziele zu erreichen, wird *Athena* mit einem großen Spiegel für Röntgenstrahlung mit einer effektiven Fläche von $2\,\mathrm{m}^2$ bei einer Energie von 1 keV ausgestattet sein.
Der Satellit beherbergt zwei wisenschaftliche Instrumente, welche in der Fokalebene sitzen. Der Wide Field Imager (WFI) hat ein großes Gesichtsfeld von $40' \times 40'$ für die Beobachtung von ausgedehnten Quellen und großflächigen Belichtungen. Außerdem verfügt er über einen Sensor, welcher auch bei hohen Zählraten helle Quellen beobachten kann. Das zweite Instrument ist die X-ray Integral Field Unit (X-IFU), welche eine Energieauflösung von 2.5 eV bei Photonenenergien unter 7 keV erreicht. Im Gegenzug hat sie ein geringeres Gesichtsfeld von 5' und eine leicht schlechtere räumliche Auflösung.
In dieser Arbeit stelle ich den Einbau von Detektoreffekten für beide Instrumente in die Simulationssoftware SIXTE vor. Diese Effekte beeinflussen das von den Instrumenten gemessene Energiespektrum. Die damit erweiterte Software wird für verschiedene wissenschaftliche Studien für die Instrumente eingesetzt. Eine dieser Studien ist es, zu testen, ob die X-IFU die bislang undetektierten Gasfilamente zwischen Galaxienhaufen nachweisen können wird, welche möglicherweise die fehlenden 30% baryonischer Materie im nahen Universum ausmachen. Dieses Warm-Hot Intergalactic Medium (WHIM) kann am einfachsten durch die schwachen Absorptionslinien in den Spektren heller Hintergrundquellen, wie dem Nachleuchten von Gammastrahlenausbrüchen (GRBs), gefunden werden. Um die Nachweis- und Vermessungsqualität für diese Linien mit der X-IFU zu quantifizieren, wurde eine hohe Anzahl an GRB-Nachleuchten mit WHIM-Absorptionslinien mit SIXTE simuliert. Die Simulationsdaten wurden anschließend mit einer Blindsuche für Linien analysiert. Es zeigt sich, dass die Mission, wie sie geplant ist, WHIM-Filamente nachweisen können wird, wenn das Nachleuchten bei Beginn der Beobachtung heller als $3 \times 10^{-11}\,\mathrm{erg\,cm^{-2}\,s^{-1}}$ ist.

In einer zweiten Studie wurde die Leistungsfähigkeit des WFI, helle Quellen zu beobachten, untersucht. Bei hohen Zählraten gelten die grundlegenden Annahmen der Analyse von Röntgendaten nicht mehr. Normalerweise liegen zwei aufeinanderfolgende Ereignisse zeitlich weit genug auseinander, um sie mit einer genügend kurzen Rahmendauer zu trennen. Dies erlaubt die Annahme, dass die Ladungsmenge, welche in einem Pixel erzeugt wurde, proportional zur Energie eines einzelnen Photons ist. Bei steigender Zählrate steigt jedoch die Wahrscheinlichkeit, dass zwei Photonen den Detektor an der selben Stelle während eines Rahmens treffen, was zu einer fehlerhaften Rekonstruktion der Zählrate und Photonenenergie führt. Dieser Effekt ist unter dem Namen Pile-up bekannt und kann durch eine aufwändige Analyse vermindert werden, durch die bestimmte Datenmuster verworfen werden. Dies führt jedoch zu einem Erblinden des Detektors bei hohen Zählraten. Beide Effekte, die fehlerhafte Energiebestimmung und die verminderte Detektionseffizienz sind unerwünschte Detektoreffekte, welche so niedrig wie möglich gehalten werden sollten. In der Studie, die in dieser Arbeit vorgestellt wird, habe ich Simulationen durchgeführt, um die Zählratenabhängigkeit der Detektionseffizienz und des Pile-up Verhaltens des Sensors zu untersuchen. Es wird gezeigt, dass der Detektor Quellen mit einer Helligkeit von 10 Crab mit einem Pile-up-Anteil von unter 1% und mehr als 90% Durchsatz beobachten kann, wenn der kleine Sensor des WFI 35 mm außerhalb der Fokalebene montiert wird. Diese Positionierung ist bereits im neuesten Design des Instruments eingeplant.
Um die Beschreibung der DEPFET-spezifischen Detektoreffekte in der Simulation zu optimieren, wurden Messungen an zwei Prototypsensoren durchgeführt. Während des Auslesens des Sensors ist jede Pixelzeile für eine kurze Zeitspanne aktiviert. Wenn ein Photon ein Pixel während dieser Zeit trifft, wird die Photonenenergie fehlerhaft gemessen. Die rekonstruierte Energie ist nicht zufällig, sondern zeigt ein systematisches Verhalten, welches durch die spezielle Umsetzung der Auslesesequenz des DEPFETs vorgegeben ist. Die Daten, die mit den beiden Prototypsensoren aufgenommen wurden, werden auf das Verhalten der gemessenen Energie bezüglich der induzierten Ladungsmenge hin für einen bestimmten Teil der Auslesesequenz untersucht. Die Ergebnisse zeigen, dass die gemessene Energie während des Endes des Clear-Intervalls nahezu exponentiell von Null auf den tatsächlichen Wert steigt. Dabei ist die Zeitkonstante energieabhängig. Allerdings wurde ein Knick in der Kurve registriert, sodass der gesamte Anstieg am besten durch die Summe zweier Exponentialfunktionen modelliert werden kann. Dieses Ergebnis kann dazu verwendet werden, die Energierekonstruktionsalgorithmen zu verbessern.

Contents

1 Introduction 1
- 1.1 A short history of X-ray observatories . . . 1
- 1.2 The *Athena* science case . . . 4
- 1.3 Structure of the thesis . . . 10

2 *Athena*: Europe's next X-ray observatory 13
- 2.1 The design of the *Athena* Observatory . . . 13
- 2.2 *Athena*'s Optics . . . 14
- 2.3 *Athena*'s Instruments . . . 17

3 Simulations for *Athena* 25
- 3.1 SIXTE: Simulating an X-ray Observatory . . . 26
- 3.2 The Detector Model of the WFI . . . 31
- 3.3 The Detector Model of the X-IFU . . . 37

4 Detection of WHIM filaments with the X-IFU 43
- 4.1 Simulation of WHIM filaments in SIXTE . . . 43
- 4.2 Detection of faint absorption lines . . . 47
- 4.3 What *Athena* can see . . . 49

5 Optimisation studies for the WFI 57
- 5.1 Pile-up: Blinding the Detector . . . 57
- 5.2 The Bright Source Performance . . . 61
- 5.3 Optimisation of the WFI's Small Sensor . . . 66

6 Measurements at the SPIX II-Experiment at MPE 71
- 6.1 The setup of the SPIX II experiment . . . 72
- 6.2 Measurements for two sensors . . . 74
- 6.3 Data extraction . . . 76
- 6.4 The Temporal Behaviour of *P05_W81_Q10* . . . 80
- 6.5 The Temporal Behaviour of *P05_WS80_Q10* . . . 88
- 6.6 Discussion and Comparison of the two Sensors . . . 95

7 Summary and Conclusions 99

Bibliography 102

A Appendix 107
- A.1 Operating Voltages for the SPIX II-Measurements . . . 107

List of Acronyms

ADC	Analog-to-Digital Converter
ADU	Analog-to-Digital Unit
ADR	Adiabatic Demagnetization Refrigerator
AGN	Active Galactic Nuclei
ARF	Auxiliary Response File
ASIC	Application-Specific Integrated Circuit
Athena	Advanced telescope for high energy astrophysics
BAT	Burst Alert Telescope
CAD	Computer-Aided Design
CCD	Charge-Coupled Device
CDF	Concurrent Design Facility
CDM	Cold Dark Matter
CERN	European Organization for Nuclear Research
CFEE	Cold Front End Electronics
CMB	Cosmic Microwave Background
CryoAC	Cryogenic Anti-Coincidence
Dec	Declination
DEPFET	Depleted p-channel Field Effect Transistor
DUT	Device Under Test
EW	Equivalent Width
eROSITA	extended ROentgen Survey with an Imaging Telescope Array
ESA	European Space Agency
FET	Field-Effect Transistor
FITS	Flexible Image Transport System
Geant	Geometry and tracking
GRB	Gamma-Ray Burst
HEW	Half Energy Width
ICPU	Instrument Control and Power Distribution Unit
IXO	International X-ray Observatory
JT	Joule-Thomson
LPA	Large Pixel Array
MIP	Movable Instrument Platform
MPE	Max-Planck-Institut für extraterrestrische Physik
MOSFET	Metal-Oxide-Semiconductor Field-Effect Transistor
PCB	Printed Circuit Board
PDF	Probability Density Function
PSF	Point Spread Function
RA	Right Ascension
RMF	Redistribution Matrix File
rms	root mean square
ROAn	ROOT Offline Analysis
SIMPUT	SIMulation inPUT
SIXTE	SImulation of X-ray TElescopes

SNR	Supernova Remnant
SPA	Small Pixel Array
SPO	Silicon Pore Optics
SPIX	Single PIXel
SRG	Spectrum-Roentgen-Gamma
TES	Transition Edge Sensor
ToO	Target of Opportunity
UV	Ultraviolet
VERITAS	VErsatile Readout based on Integrated Trapezoidal Analog Shapers
WFEE	Warm Front End Electronics
WFI	Wide Field Imager
WHIM	Warm-Hot Intergalactic Medium
X-IFU	X-ray Integral Field Unit
XLF	X-ray Luminosity Function
XML	Extensible Markup Language
XRT	X-Ray Telescope
ZIF	Zero Insertion Force

1 Introduction

This thesis is the result of my work on simulations for one of Europe's next big projects in astronomy: *Athena*. *Athena* is an X-ray observatory which is planned to be launched in 2028[1] to deliver answers to some of the biggest questions of our understanding of the universe. The true meaning and impact of these questions can only be understood in the context of the developments of the scientific field, so this chapter gives an insight into the history of X-ray astronomy, before taking a deeper look into the science goals of the *Athena* mission.

1.1 A short history of X-ray observatories

For thousands of years, astronomy has been limited by the astronomer's body, having two eyes sensitive only in the optical regime and being bound to the surface of the Earth. However, in their imagination humans started to step outside the Earth's atmosphere, up to a view from above, long before rockets were developed. This capability to transform the two-dimensional appearance of the night sky into a three-dimensional universe has led to different theories about the structure of our world, as for example the structure of our solar system.

As mighty as human's capability for abstraction is, it needs some input to come to the right conclusions. In the case of X-ray astronomy, such an input did not exist until the first half of the 20th century. Only then, both X-ray detectors and rockets suited to carry them above the atmosphere were developed. In 1895, Wilhelm Röntgen was the first to write a scientific paper on a new kind of radiation (Röntgen, 1896), which expanded the electromagnetic spectrum known to scientists to the X-ray regime. It took fifty more years until rockets were developed far enough to enter outer space. This was first achieved with the Aggregat 4, better known as the V-2 missile developed as a weapon in the Second World War by a group around Wernher von Braun (Dornberger, 1952). After the war,

[1] `http://sci.esa.int/cosmic-vision/54517-athena/`

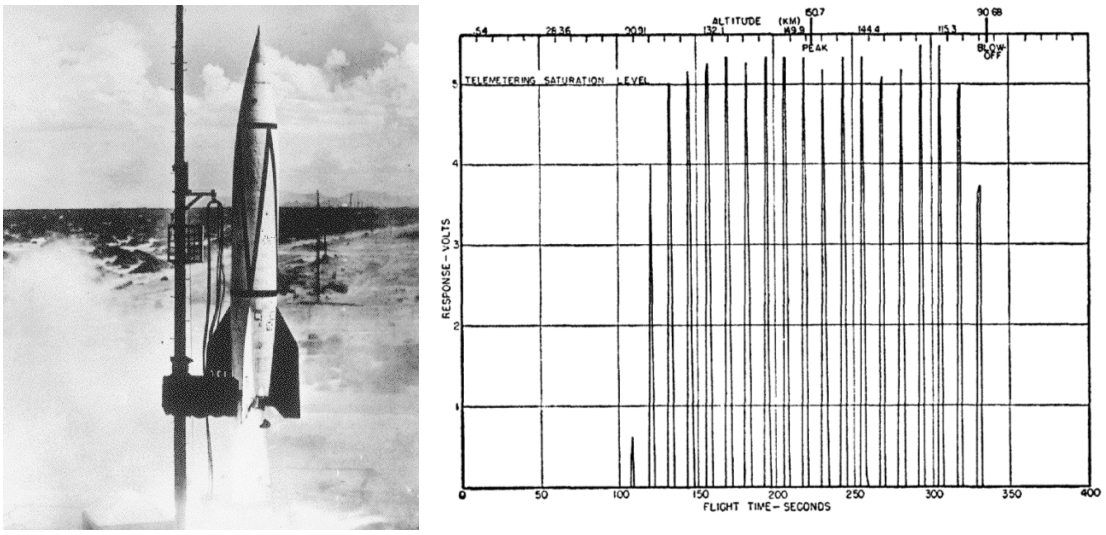

Figure 1.1: Left: A post-war V-2 rocket at launch. The warhead is located at the top. After the war, captured rockets had the explosive charge substituted with scientific instruments such as the X-ray photon counters of flight No. 49. Image from `https://history.msfc.nasa.gov/rocketry/29.html`. **Right**: The raw data of an X-ray photon counter over time, taken during the flight of the rocket. Each peak represents the sun moving through the field of view while the rocket spins around its axis. Figure from Friedman et al. (1951).

both the USA and the USSR tried to learn as much from the V-2 program as possible by studying the design and flight of the rocket and by basing new developments on it (Chertok & Siddiqi, 2005; Kennedy, 2006).

Some of the rockets were used for scientific experiments not directly related to the development of rockets by replacing the explosive payload in the warhead with scientific instruments. With photon counters carried by such V-2 rockets, the first records of solar X-rays were taken in 1949 (Friedman et al., 1951). A plot of the data gathered by V-2 No. 49 on 1949 September 29, is shown in Fig. 1.1. In the following years, little changed for the methods of X-ray astronomy. Sounding rockets were developed further. The discovery of the first cosmic X-ray source, Sco X-1, in 1962 was made with Geiger counters lifted with an Aerobee rocket (Giacconi et al., 1962). This flight allowed to take data at altitudes of over 80 km, but for only 350 s.

Only in the 1970's, X-ray astronomy received the tools necessary for efficient scientific observations with long exposure times and good angular resolution. With *Uhuru* (Giacconi et al., 1971), the first satellite dedicated to X-ray astronomy was launched on December 12, 1970. *Uhuru* was equipped with two sets of proportional counters placed behind collimators with a resolution of $0.52° \times 5.2°$ and $5.2° \times 5.2°$. By spinning around its axis, the satellite surveyed the X-ray sky in the 1.7 keV–18 keV band to compile a catalogue with the positions and intensities of 339 sources, featuring, for example, Seyfert galaxies and galaxy clusters (Giacconi et al., 1972, 1974; Forman et al., 1978). In the same decade, the first evidence for an iron emission line was found with *Ariel 5* in an observation of the Perseus Cluster, indicating the presence of a hot plasma (Mitchell et al., 1976). In 1978,

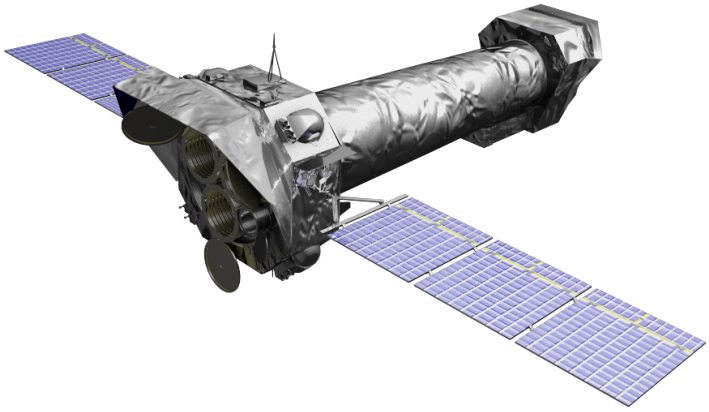

Figure 1.2: An artistic view of *XMM-Newton*. The three X-ray telescopes are mounted in the service module. They focus the radiation to the focal plane platform at the other end of the 10 m long spacecraft. Energy is supplied by solar panels, which give it a span of 16 m. Image courtesy of C. Carreau and ESA (`http://xmm-tools.cosmos.esa.int/external/xmm_science/gallery/images/XMM_SC_02.png`).

the first X-ray telescope with the capability to truly image the sky with focussing optics was launched on board *HEAO 2* (Giacconi et al., 1979; Giacconi, 1980). The difficulty with high-energetic radiation such as X-rays is the inability of conventional mirrors to reflect the photons. Collimators only select radiation from a certain region on the sky by blocking the rest, but can not provide a focused image. *HEAO 2* finally used a Wolter I-type mirror (Wolter, 1952) which uses the effect of grazing reflection and features four nested surfaces with a total effective area of 400 cm^2 at 0.25 keV and 30 cm^2 at 4 keV. At a focal length of 3.4 m, it provides a picture of the sky with a Point Spread Function (PSF) of 2″ rms (Giacconi et al., 1979).

Another big step in the technological history of high-energy astronomy was the first use of Charge-Coupled Device (CCD) detectors for X-ray detection on board the *ASCA* spacecraft (Tanaka et al., 1994). With this development, all important technologies for the main parts of modern X-ray telescopes had been established. The combination of Wolter mirrors and CCD sensors is still in use in modern X-ray observatories, such as *Chandra* (Weisskopf et al., 2000) and *XMM-Newton* (Jansen et al., 2001, see Fig. 1.2). *XMM-Newton* was launched on 1999 December 10, and is in operation for 17 years to the date of this thesis. It is equipped with three Wolter I mirrors, each of which has a focal length of 7.5 m and a maximum diameter of 70 cm. They provide an effective area of approximately 1400 cm^2 at 1 keV each and an angular resolution of 4.5″–6.6″ at 1.5 keV, depending on the telescope. Each of the telescopes focusses X-rays towards its own detector. The satellite is equipped with three cameras with slightly different construction. Two of the cameras consist of seven MOS-CCDs (Turner et al., 2001), the third is composed of twelve pn-CCDs on a single wafer (Strüder et al., 2001). The mirrors of *XMM-Newton* are located in the Service Module inside the launch vehicle adaptor interface ring. The detectors are housed on the instrument platform at the other end of the spacecraft (Jansen et al., 2001). The next X-ray all-sky survey mission with the eROSITA-instrument on the Russian satellite *SRG* will also be equipped with the combination of CCD-detectors and Wolter optics (Predehl et al., 2010). The eROSITA instrument features seven individual telescopes, which each focus on their own camera to monitor the sky.

1.2 The *Athena* science case

From a technical point of view, *Athena* as described in the following chapter is a logical step forward from current X-ray observatories like *XMM-Newton*. However, the reason for the construction of a scientific satellite is not primarily the improved technological development. Instead, each mission is seen as a tool to gather information about specific scientific questions. *Athena* is the proposed tool to answer the questions raised by the Science Theme of the Hot and Energetic Universe as described by Nandra et al. (2013) in the context of ESA's Cosmic Vision program (Nandra et al., 2014). This Science Theme is meant to gain a better understanding of the evolution of the universe. The topic is structured into two main science goals. The first is to understand the evolution of the large scale structures in today's universe, consisting of galaxy groups and clusters. *Athena* aims to trace their formation back to redshifts of $z \approx 2-3$ (Nandra et al., 2013). The second topic goes back even further in the history of the universe, up to $z \approx 6-10$. The goal here is to observe the evolution of black holes at the time of the first formation of galaxies and to describe the feedback from black holes on the evolution of the structures surrounding them (Nandra et al., 2013).

Because of the interconnection between the science goals and the technical implementation of the *Athena* mission, it is very important to understand the scientific questions which have to be answered by the instruments. To get the best mission possible, each of the science topics has to be analysed and translated into technical requirements of the individual parts of the spacecraft. In the next sections, the science case for *Athena* will be presented, following the *Athena* White Paper (Nandra et al., 2013) and Mission Proposal (Nandra et al., 2014).

1.2.1 Large-scale structure formation

In 1989, Geller & Huchra (1989) found that there exist structures in the universe which are larger than galaxies, groups of galaxies and even larger than galaxy clusters. With the discovery of this so-called cosmic web the picture of our cosmos changed and opened the question how such large-scale structures have formed. During the past decades, a series of ambitious N-body simulations were performed with the goal of comparing the outcome of different cosmological models to the observed universe (Springel et al., 2005; Boylan-Kolchin et al., 2009; Angulo et al., 2012). These simulations, of which the Millennium simulation is a typical example, model the evolution of the universe from the first inhomogeneities as seen today in the Cosmic Microwave Background (CMB) until the present. This approach allows to test our current understanding of the mechanisms involved.

However, to get a detailed picture of the processes which form the structures, a well-established foundation of observational data is necessary. This requirement motivates the first of *Athena*'s science topics, the quest for answers on how the large-scale structures have formed in our universe. Structure formation is a temporal process, but in astronomy and especially cosmology, scientists are mostly limited to static pictures, as the time scales

in which notable changes evolve are very long. This difficulty requires the observation of a multitude of sources with a broad variety of distances. Fortunately, due to the finite speed of light, the observation of a source far away gives us a glance of the past such that we can trace the evolution of the universe not directly but by comparing the properties of different sources at different distances and thus at different points in the past.

In our recent understanding, the evolution of the universe driven by gravitation can be well described by the so-called Λ-Cold Dark Matter (CDM) model (Alam et al., 2016, and references therein). This model assumes a spatially flat universe dominated by the influence of the cosmological constant Λ and cold dark matter [2]. According to observations of the CMB, only around 30% of the energy density of the universe is concentrated in matter (Planck Collaboration et al., 2016). These measurements also show that only about 15% of the matter in the universe is baryonic, and 84% form what is known as the dark matter, the nature of which is not yet understood. The large fraction of dark matter makes it especially difficult to understand the universe's evolution, as most of the matter forming it can not be observed directly. *Athena*'s mission is to trace the development of the observable large-scale structures in the universe back to $z \approx 2-3$ (Nandra et al., 2013) to shed light on the early evolution. In its proposed survey program, *Athena* is meant to find 50 massive galaxy groups at redshifts larger than 2. In order to be able to search effectively for such structures, a large effective area and a large field of view with a good angular resolution are required (Nandra et al., 2014). Besides the morphology which can be examined with images from a survey, it is also very important to understand the dynamics in the clusters. *Athena* must therefore be able to determine the velocities of the gas contained in galaxy clusters to a very high accuracy. The gas velocity can be measured by line shifting or broadening due to the redshift induced by the motion of the gas (Ettori et al., 2013). This task requires a well-calibrated instrument with a very high spectral resolution which is able to cover a relatively large field of view (Nandra et al., 2014).

To truly understand the processes involved in structure formation, also the feedback effects from already developed objects to the surrounding medium need to be understood. Simulations modelling the evolution of structures need to take into account, for example, the energy released by supernovae (Kauffmann et al., 1999). Such events reheat the surrounding gas and lead, for example, to a higher rate of star formation. A similar effect can be observed for Active Galactic Nuclei (AGN), which eject parts of the energy gained by accretion back into the surrounding medium, heating the cluster gas (Sijacki et al., 2007; Volonteri et al., 2016). *Athena* will address also these mechanisms by measuring entropy profiles of the cluster gas (Ettori et al., 2013). This again requires a high angular resolution and a large field of view. Furthermore, the regions in which the jets of AGN interact with the surrounding medium must be analysed spectroscopic but spatially resolved. High-quality spectral data will give details about the mechanical energy deposited by the feedback process and the temperature distribution of the gas (Croston et al., 2013). This science goal again requires an imaging instrument with a high spectral resolution (Nandra et al., 2014).

[2] Cold in this context means a particle velocity which is low compared to the speed of light.

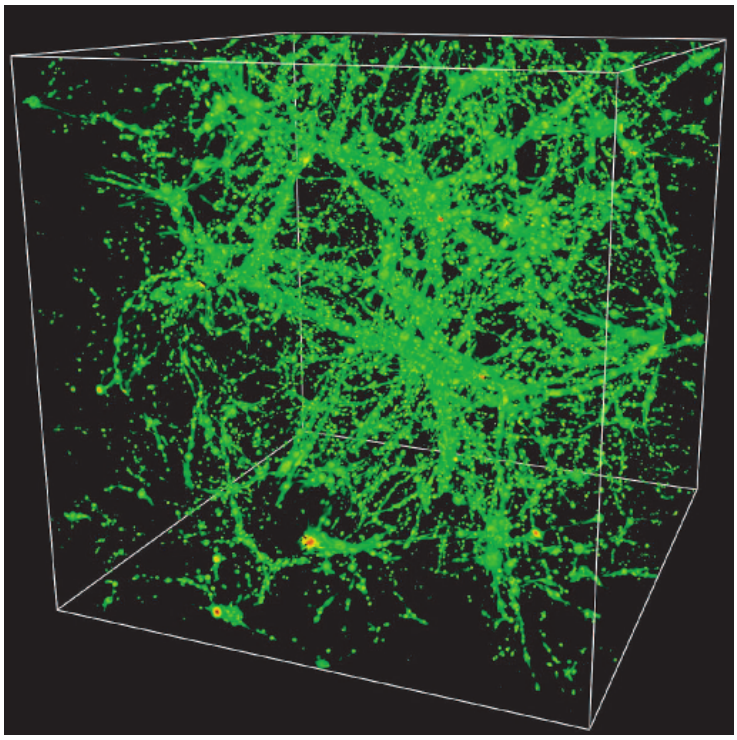

Figure 1.3: The spatial density distribution of the warm-hot gas as the outcome of the simulations performed by Cen & Ostriker (2006). The simulation cube depicts a volume of $85\,h^{-1}$ and shows the distribution as expected at $z = 0$. The gas has temperatures between $10^5 - 10^7$ K. Colour-coded is the density of the gas: the green, yellow and red colours translate to values of 10-20, 100 and 1000 times the mean baryon density of the universe at $z = 0$. The points of very high density depict the locations where galaxies are formed. The low-density gas builds a web between these regions. Illustration taken from Cen & Ostriker (2006).

Another difficulty in our current understanding is that a large fraction of around 30% of all baryons in the local universe has still not been traced by observations (Shull et al., 2012). Parts of these yet unobserved baryons are thought to form the Warm-Hot Intergalactic Medium (WHIM). Simulations predict that this matter follows the structure of the cosmic web, forming low-density filaments along it, as depicted in Fig. 1.3. The matter in these filaments is heated up to temperatures of $10^5 - 10^7$ K by shock fronts caused by the cosmic structure formation and by feedback effects as described above (Cen & Ostriker, 2006). Thus, their temperature is so high that they can only be observed at X-ray energies. As has been shown by Yoshikawa et al. (2003), the bremsstrahlung and line emission of most WHIM filaments is very weak. Instead, *Athena* aims to detect this matter by its absorption lines which can be measured in the energy spectrum of a bright background source such as an AGN or Gamma-Ray Burst (GRB) afterglow (Kaastra et al., 2013). The goal is to find 200 filaments in the spectra of 25 nearby AGN and 40 distant GRBs by tracing the faint absorption lines such as the O VII or O VIII features. In approximately 30% of the detected absorption systems, *Athena* is expected also to detect weak emission lines, which can be used to measure the density of the gas, its ionisation, gas temperature, and other physical properties (Kaastra et al., 2013; Nandra et al., 2014). The very high signal to noise ratio required to detect and measure such faint features with equivalent widths of only up to around 0.28 eV (Branchini et al., 2009, E. Ursino, priv. comm.) necessitates a high effective area especially at low energies and a very high energy resolution. This observation approach also implies that the low energy threshold of the instrument must be sufficiently low such that the redshifted lines can be observed down to approximately 0.2 keV. Additionally, for being able to observe the WHIM in front

of GRB afterglows, the trigger efficiency to react on Target of Opportunity (ToO) events must be high.

Baryonic matter does not only evolve in its spatial distribution during the development of large scale structures, but its elemental composition also changes with time. In the current understanding, a large fraction of the heavy elements in the universe has its origin in supernova explosions. The standard classification knows two main categories of supernovae: Type Ia supernovae are thought to be the explosions of a white dwarf with a mass close to the Chandrasekhar limit in a binary system (Churazov et al., 2014). The white dwarf accretes mass from its companion until it exceeds a critical mass and launches an explosive burn of carbon or helium (Whelan & Iben, 1973; Woosley & Weaver, 1986; Hillebrandt et al., 2013). The other species of supernovae are caused by the events which happen to a massive star at the end of its life. When the equilibrium between the gravitational force and the gas pressure due to heating of the star's gas by nuclear reactions in the core can not be maintained due to various effects (Heger et al., 2003), the core of the star collapses. The infall of the matter due to the collapse releases energy which is partially transferred to the outer layers of the star (Woosley & Weaver, 1986), initiating the supernova explosion. Regardless which type of supernova, each of them carries kinetic energy and heavy elements into the surrounding medium, influencing the structure formation in its vicinity. However, for both models, details about the explosion mechanics are largely unknown. In order to improve our understanding of the processes, *Athena* will perform spatially resolved spectroscopy, measuring the abundances of heavy elements and velocity profiles of Supernova Remnants (SNRs). The data gained from these observations will give us information about the explosions and the chemical history of the universe up to a redshift of $z = 2$. This task requires a large field of view of the detectors and a low background due to charged particles (Decourchelle et al., 2013; Nandra et al., 2014).

1.2.2 Black hole evolution and feedback

Black holes represent the probably most extreme state of a physical object in our universe. Its matter is concentrated in a volume so small that due to the deep gravitational potential not even light can escape. However, many cosmic black holes can be observed indirectly during accretion processes when gravitational potential energy is partially converted into electromagnetic radiation. Supermassive black holes can be found in the centres of galaxies forming Active Galactic Nuclei (AGN). These objects are thought to have a strong influence on the evolution of galaxies and the structures in the universe (see Sect. 1.2.1).

The formation and growth of the supermassive black holes in the early universe is not yet understood. To investigate this topic, *Athena* will extend the sample of known AGN to redshifts of $z \approx 6-8$ or higher and to low intrinsic luminosities of $L_X \approx 10^{43}-10^{45}$ erg s^{-1} in a deep survey program in cooperation with optical and infrared observatories (Aird et al., 2013; Nandra et al., 2014). To perform a deep survey over a large area on the sky, *Athena* needs to have a large field of view and, at the same time, a good angular resolution, with a large affective area. Additionally, to constrain the positions of the

sources found in the survey to a high precision, the reconstructed astrometric error must be small. In connection to the development of these early AGN, the nature of the first generation of stars (which are the possible progenitors for the first supermassive black holes) needs to be determined. This task will be achieved by measuring the elemental abundances at high redshifts, which can be gained through the analysis of absorption features in distant GRB afterglows. As described for the search for WHIM, the observation of GRB afterglow requires a good ToO trigger efficiency for an instrument with a high effective area and good spectral resolution (Nandra et al., 2014).

Through different observations in a multitude of wavelengths, our picture of AGN has mostly converged into the so-called unified model (see, for example Urry & Padovani, 1995), in which a supermassive black hole accretes matter which forms an accretion disk. On the far side, the accretion disk connects to a torus-like gas distribution. When matter falls onto the black hole, parts of the gas can be ejected at the axis perpendicular to the accretion disk, forming jets. The high-energetic radiation produced during the accretion can be observed in the X-ray regime. However, the exact geometry of such systems can not be resolved directly due to the small apparent size of the active region. Also, details of the accretion processes and the evolution of the systems are still unknown.

To constrain the accretion geometry of AGN, a method called reverberation mapping can be applied (Uttley et al., 2014). When light is emitted isotropically from a point above the central black hole, it is scattered by the medium surrounding it. An observer will measure the initial flash of light and additionally the echo of the scattered light. The shape and length of this echo is a cumulative result of the different light travel times from the original source to the locations where the scattering occurred. As a result, the measurement of such features can give us information about the size and geometry of the matter distribution surrounding the black hole (Matt & Perola, 1992). Time signals of this kind were already measured in the past (for example by Fabian et al., 2009; Emmanoulopoulos et al., 2011; De Marco et al., 2013). *Athena* will perform observations of eight AGN which have already shown such features but for a wider frequency range, to determine the geometry of the system, especially of the innermost region and the disk-corona system (Dovciak et al., 2013). Furthermore, it will extend this examination to time lags of the Fe Kα line in galactic black hole binary systems. To achieve this goal, a large effective area over a broad energy range is required, and especially for the bright galactic sources, the detector needs to have a high count rate capability and a good spectral resolution at the region of the iron line (Nandra et al., 2014).

The measurement of the spin of black holes can also be used to constrain the processes which are involved during their growth. Berti & Volonteri (2008) showed that different scenarios like black hole merging or accretion generally lead to different spins of the resulting object. For example, they described how merging black holes do not automatically lead to a black hole with a high spin but only produce intermediate values in many cases. *Athena* will be used to measure the spin of supermassive black holes in the local universe as well as of galactic black holes by using the spin-sensitive Fe Kα line profile and the reflection continuum (Dovciak et al., 2013; Dauser et al., 2016). This objective again requires a large effective area around the iron line energy as well as good spectral resolution and count rate capability (Nandra et al., 2014).

To describe the evolution of AGN, the X-ray Luminosity Function (XLF) was introduced. This is the number density function of AGN at a certain redshift with a certain intrinsic luminosity (see, for example, Ueda et al., 2003, 2014). The development of the supermassive black holes which is encoded in this function can give us information about the conditions under which the black holes grow over time (Georgakakis et al., 2013). The determination of the XLF needs observations of a large sample of AGN with well-known parameters. Especially for heavily obscured AGN at cosmological distances, the observed flux is very low, leading to a biased sample. *Athena* will extend this sample to highly absorbed sources at redshifts up to $z \approx 3.5$, such that the models for the XLF can be improved. Such a survey needs again a large effective area over a broad energy range of approximately 1-6 keV with a good angular resolution and a large field of view and low particle background, as well as a good astrometric accuracy (Nandra et al., 2014).

The development of an AGN depends strongly on its time-dependent mass accretion, which allows it to grow further and also to release energy into the surrounding space as described before. Thus, the ejecta of an AGN can tell us about the accretion rate and processes. One of *Athena*'s goals is to find such outflows and to determine the mechanical energy which is released in the outflows of AGN at a broad redshift range between $z = 1$ to 4. This can be achieved by searching for ionised absorbers in the X-ray spectra and by measuring the line properties to determine the velocity of the gas. This project also sets requirements on the effective area of the telescope, and especially the measurement of the line properties will profit from a high spectral resolution down to low energies (Georgakakis et al., 2013; Nandra et al., 2014).

While the history of accretion must be studied back to high redshifts, the details of the accretion processes and the interaction between the outflows and winds of such systems with their environment can be best studied on nearby AGN. By precise measurements of the ejected gas mass, velocity and metal content of bright AGN, the total mechanical energy released during the accretion process can be determined. Furthermore, the way on which the released gas interacts with the surrounding medium, possibly leading to an increase in star formation, will be determined by using spatially resolved spectroscopy of nearby sources. In order to be able to conduct these measurements, *Athena* needs to provide a large effective area and the possibility to measure X-rays even at low energies, constraining the low-energy threshold (Cappi et al., 2013; Nandra et al., 2014).

1.2.3 *Athena* performance requirements

The science goals presented in the previous descriptions give requirements which must be translated to performance parameters of the spacecraft and its instruments. As has been discussed above, different science goals require a large field of view, a high count rate capability and also a very good spectral resolution. To achieve the goals, *Athena* is planned to have two scientific instruments, the Wide Field Imager (WFI) and the X-ray Integral Field Unit (X-IFU). The WFI is a large-area detector to provide the large field of view and has also a high count rate capability. The X-IFU will provide the capability to perform imaging spectroscopy with high spectral resolution. The requirements on the different aspects of the mission derived from the science goals are listed in the *Athena*

Table 1.1: The performance requirements for the *Athena* mission according to Nandra et al. (2014). The PSF's Half Energy Width (HEW) is the diameter of a circle projected onto the sky which encompasses half of the total flux of a point source due to the finite resolution of the optics.

Optical requirements	
Effective area at 1 keV	$2\,\mathrm{m}^2$
Effective area at 6 keV	$0.25\,\mathrm{m}^2$
On-axis PSF HEW below 8 keV	5"
Off-axis PSF HEW below 8 keV	10"
X-IFU requirements	
Spectral resolution	2.5 eV
Energy calibration accuracy	0.4 eV rms
Field of view (diameter)	5'
Low energy threshold	0.2 keV
Total optical filter attenuation at 1200 Å	Factor 10^{12}
WFI requirements	
Field of view	40' × 40'
Spectral resolution at 6 keV	150 eV
Count rate capability at 80% throughput	1 Crab
Charged particle background	$<5 \times 10^{-3}\,\mathrm{cts\,s^{-1}\,cm^{-2}\,keV^{-1}}$
Reconstructed astrometric error	1" (3σ)
Absolute astrometric error	3" (3σ)
Trigger requirements	
GRB trigger efficiency	40%
ToO reaction time	<4 hours

Mission Proposal (Nandra et al., 2014) and are summarised in Table 1.1. These values build the foundation for the design of the instruments, which will be described in the next chapters.

1.3 Structure of the thesis

Athena is currently in an early stage of its development, where many details about the scientific instrumentation are not yet fully decided, as will be seen for example for the configuration of the mirror system. The work presented in this thesis was conducted to test the performance characteristics of *Athena*'s instruments and to optimise specific design parameters. To introduce the observatory and its instruments, a closer look will be given onto the spacecraft's configuration as currently envisaged in the next chapter. It tries to give a primer on the technical construction and components of the satellite without going into too much functional details. The sensors of *Athena* are based upon relatively new technologies which have required modifications to the SIXTE simulation software. The physical foundation of the sensors which are relevant for the simulations presented hereafter will be explained in Chapter 3 together with a description of their implementation in the simulator. The descriptions given in this chapter complete the

picture given in Chapter 2.

Chapters 4 and 5 show two cases of detector simulations with different motivations. The simulations presented in Chapter 4 represent a test of the detector's capability to achieve a particular science goal, the search for WHIM. This is one of the tasks presented in Section 1.2.1 which pushes the X-IFU on its limits. Thus the detailed knowledge of the capabilities of the current design are extremely important for the further development of the instrument as well as for the interpretation of the real observation data which will be gained after the launch of the spacecraft.

Chapter 5, on the other hand, gives an example on how detector simulations can be used to optimise a specific detail of the instrument's configuration. In this chapter, a routine test, the bright source capability study, shows the improvement of a particular detector property by using a counter-intuitive setup, namely operating the detector out-of-focus. The outcome of this study led to a further investigation of the topic, which resulted in a optimisation of the out-of-focus position of the WFI's high-count rate capable sensor.

An approach of this kind requires a good understanding of the detector function such that the results of the simulations can be trusted. This means that the detector description in the simulations must be controlled and tested to a high standard, especially if the conclusions need to be quantified very accurately. In order to compare and extend the simulation's implementation of the detectors used for the WFI, Chapter 6 describes the analysis of data measured on prototype sensors for the instrument. The results of this analysis will be used in future studies. Finally, in the last chapter, a summary on the work performed in the course of this these is given.

2 *Athena*: Europe's next X-ray observatory

The design of the *Athena* X-ray observatory (Nandra et al., 2014) builds on the tradition from *XMM-Newton* (Jansen et al., 2001) and the *IXO* study (Barret et al., 2011), a candidate for the European Space Agency (ESA) Cosmic Vision L-class mission. *Athena* is currently in the Phase A of the mission lifetime cycle, with the Mission Adoption Review pending in 2019 to 2020 (Ayre et al., 2016). The scheduled launch date is 2028, when it will be placed in an orbit around the Lagrange point L2[1]. In the next section, the general design of the spacecraft will be presented, followed by a description of its optics and the two X-ray detectors.

2.1 The design of the *Athena* Observatory

Looking at the current design renderings of *Athena* as, for example, in Fig. 2.1, the conventional design of the spacecraft and the heritage from previous missions such as *XMM-Newton* (compare Fig. 1.2) is obvious. The spacecraft consists of three main components: The Service Module, recognisable by the large solar panels attached to it, the Fixed Metering Structure forming the telescope tube, and the Focal Plane Module (Ayre et al., 2016).

The Service Module houses the systems which are not part of the scientific payload that are needed to maintain the spacecraft. Additionally, as already seen on *XMM-Newton*, the X-ray mirrors are mounted to this structure inside the ring-shaped interface to the launch vehicle adaptor. Unlike the three individual mirrors of *XMM-Newton*, *Athena* features only a single but large mirror, combined with its support structure, the hexapod mount, star trackers as well as control systems in the Mirror Assembly Module (Ayre et al., 2016).

[1] `http://sci.esa.int/cosmic-vision/54517-athena/`

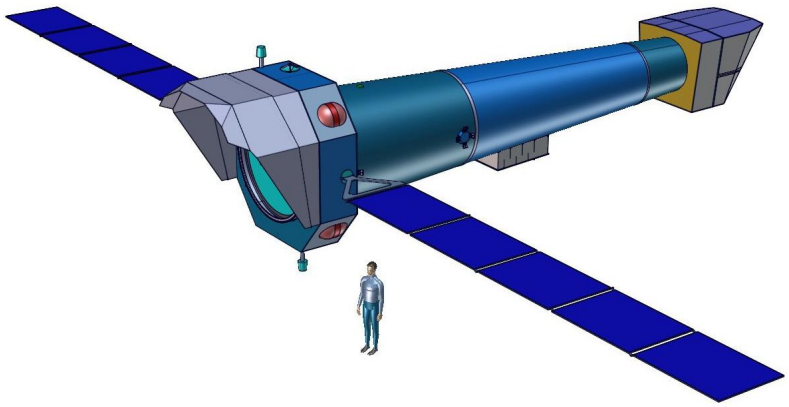

Figure 2.1: A rendering of the *Athena* spacecraft as planned in ESA's Concurrent Design Facility. At the front, the Service Module holds the mirror. The Focal Plane Module at the back houses both scientific instruments and is attached to the spacecraft via the Fixed Metering Structure. The spread across the solar panels is larger than 26 m, with a length from the tip of the sun shield to the end of the Focal Plane Module of almost 16 m. Image from Ayre et al. (2016).

The Fixed Metering Structure connects the Service Module to the Focal Plane Module and is designed to keep the instruments at the distance required to rest in the focal plane of the mirror (Nandra et al., 2014). In the Candidate Prime spacecraft designs, the actual Service Module is relocated to a place at the tube forming the Fixed Metering Structure (Ayre et al., 2016).

The Focal Plane Module sits at the rear end of the tube and houses the scientific payload, consisting of two instruments: The WFI (Meidinger et al., 2016) and the X-IFU (Barret et al., 2016). As the spacecraft carries only one mirror but two instruments rely on focussed X-ray light, a mechanism is needed to switch between the individual detectors. This is accomplished by the hexapod structure with which the mirror is connected to the spacecraft, as will be explaned in the next section.

2.2 *Athena*'s Optics

As discussed in Chapter 1 and defined in the *Athena* Mission Proposal (Nandra et al., 2014), the goal for *Athena*'s optical system is an effective area of 2 m^2 at 1 keV. The mirror layout follows the Wolter type I scheme (Wolter, 1952) as shown in Fig. 2.2. Due to the required grazing reflection, short ring–like sections of a paraboloid and hyperboloid surface are arranged in sequence. As the effective area of such mirror shells is small, a larger number of these paraboloid–hyperboloid units with different radii but the same focal length are nested in the final mirror. The mirror collects the X-ray photons and focusses them to the instruments mounted in the Focal Plane Module at a distance of 12 m. To achieve this requirement, a relatively new technology will be used: Silicon Pore Optics (SPO), which deliver a high effective area at a rather low mass (Collon et al., 2016). The Mission Proposal expects an improvement in the mass–to–effective area ratio of a factor of six in relation to traditional X-ray mirror designs as used for *XMM-Newton*.

Current papers list two design versions of the mirror: the proposed mirror as described

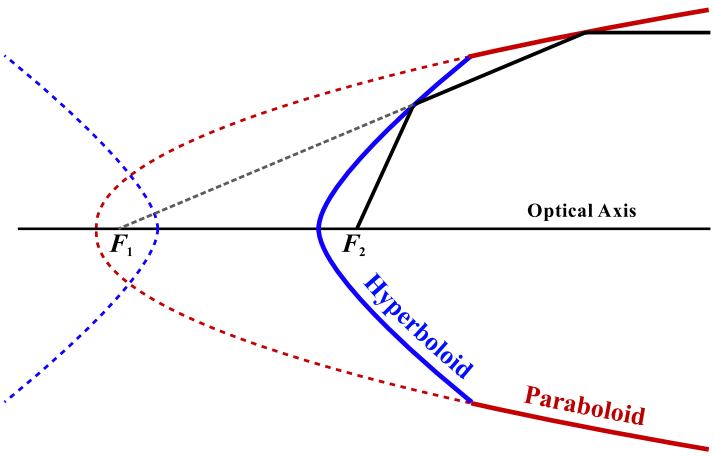

Figure 2.2: Scheme of a Wolter type I mirror system. A paraboloid mirror focusses light from infinity to a focal point F_1. As the reflection of X-ray photons requires grazing reflection and thus a flat angle of incidence, the focal length is large compared to the diameter of the usable section of the paraboloid mirror. A second mirror in the shape of a hyperboloid is used to shorten the focal length, shifting the focal point from F_1 to F_2. In reality, only short sections of both surfaces, at the region around the transition from paraboloid to hyperboloid, can be used. Modified after Wolter (1952).

above, and the outcome of the Concurrent Design Facility (CDF) study with a smaller mirror to fit inside the largest available standard adaptor to the launch vehicle, the Ariane 5. This limits the diameter of the mirror to be smaller than 2624 mm and the effective area decreases to a value between 1.37 m^2 to 1.56 m^2, depending on the exact design of the SPO modules (Ayre et al., 2016). Figure 2.3 illustrates the difference between the effective area of both mirror designs.

In contrast to conventional X-ray mirrors, where continuous rings are manufactured and nested in each other, SPO mirrors use small Mirror Modules, which are mounted in a design specific pattern to form a large mirror. The CDF–proposed mirror layout is illustrated in Fig. 2.4. It consists of 678 individual Mirror Modules arranged in 15 concentric rings around the mirror centre. The proposed mirror design extends this to 19 rings, which hold a total of 972 Mirror Modules. The four innermost rings consist of modules with a maximum width of 6 cm, the outer modules have a width of 10 cm (Ayre et al., 2016).

Each individual mirror module consists of four SPO stacks. These stacks are the core of the new technology: instead of manufacturing a large and very precise surface with the

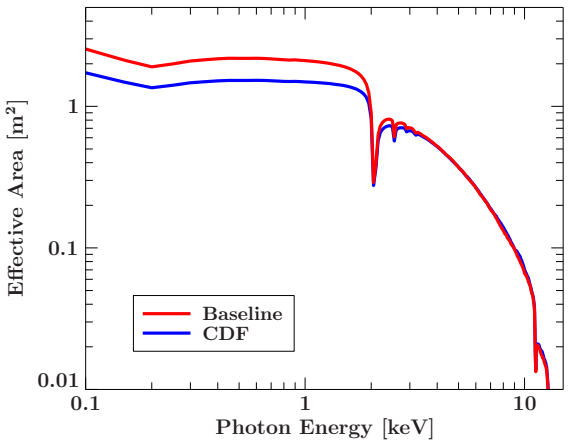

Figure 2.3: The effective on-axis mirror area of *Athena* as proposed (**red**) and as described in the CDF study (**blue**). The data shown in this plot are the results of ray-tracing simulations and have been provided by Richard Willingale. They assume a rib spacing of 2.3 mm with a rib thickness of 0.17 mm. The reflective surfaces are coated with Iridium and a B_4C overcoat. The aperture of the baseline design has a radius of 1469 mm with 19 rings of Mirror Modules, leading to an effective area of 2.1 m^2 at 1 keV. The CDF study features four rings less with a radius of 1190 mm for the aperture and an effective area of 1.5 m^2 at 1 keV. The dips at energies above 2 keV are absorption edges of Iridium.

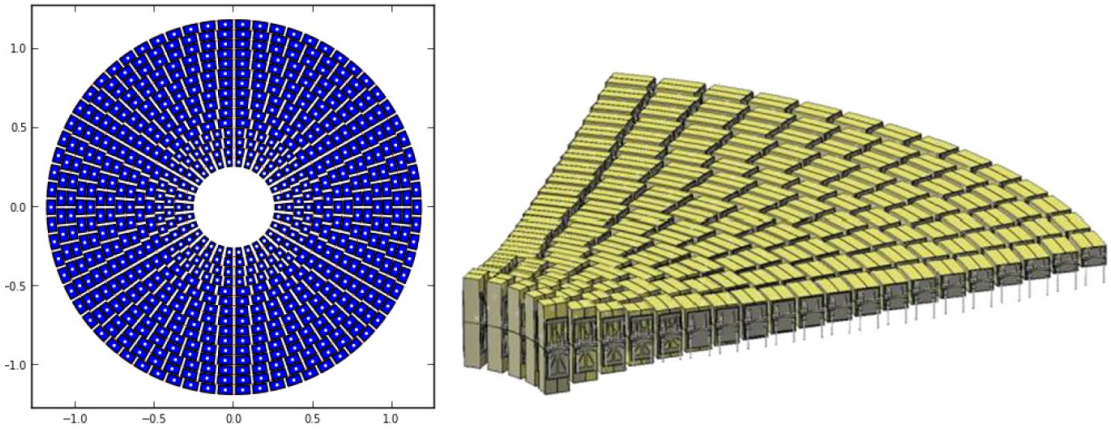

Figure 2.4: Left: The layout of the *Athena* mirror as seen from the front. Each white dot marks the centre of a mirror module (blue). **Right**: A perspective view of a section of the mirror. The individual mirror modules and their supporting structures can be seen. Images from Ayre et al. (2016).

right curvature to later place inside the mirror system, an SPO stack is made from simple plates of silicon. The silicon wafers used to produce this optical system can be acquired from the semiconductor industry and have a very high surface evenness of 0.1 nm rms and a high plan-parallelism better than 1 μm over a baseline of 0.3 m (Collon et al., 2016). These wafers are layers of almost mono–crystalline silicon with a thickness on the order of a millimetre. They are cut to a rectangular shape and grooves are etched into the material, leaving only thin ribs standing on a thin membrane. For each Mirror Module, several tens of these ribbed plates are stacked and bonded. Here, only the ribs of one plate connect to the next plate, while the grooves form pores in the final assembly. The smooth, unaltered surface of the wafers which is located between the ribs is coated with a highly reflective layer from Iridium and a B_4C overcoat before the stacking process, and serves as the actual mirror surface (Collon et al., 2016).

To achieve the curvature necessary for building a Wolter-type mirror (Wolter, 1952), the ribbed silicon plates are bent into shape during the stacking and bonding process. The result is a cube-like piece of silicon with a high number of embedded thin, reflective sectors of a Wolter I mirror as shown in Fig. 2.5. Due to the high number of modules necessary to form the complete mirror, the automation of the assembly process is being worked on (Wille et al., 2016).

As *Athena* provides one large mirror for both X-ray instruments, a mechanism is necessary to move the optical axis relative to the instruments. Different to the *Athena* Mission Proposal (Nandra et al., 2014), the current design does not rely on the use of a Movable Instrument Platform (MIP) to change the instrument positions between observations. Instead, the mirror itself is tilted to illuminate the detector chosen for a given observation. This is achieved by mounting the optical system on a hexapod-system. This system consists of six telescope arms which attach the mirror to the service module. Each of these

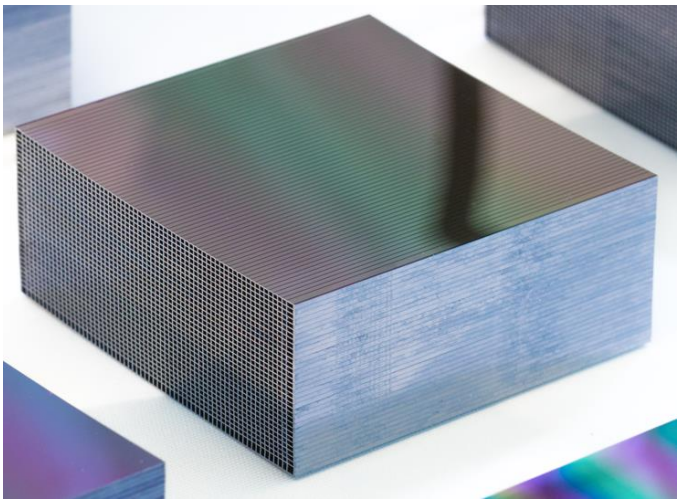

Figure 2.5: A stack of 35 layers of silicon plates. At the left side, the pores can be seen. Each layer is a thin plate of silicon, into which grooves are etched, forming the pores. While the individual layers are stacked, they are deformed such that the back face of each pore is an approximation of a small section of a Wolter-1 mirror. To gain the reflectivity necessary to image X-rays, the respective surfaces are coated with Iridium and B_4C. Such stacks form the mirror modules of *Athena*'s optics, as shown in Fig. 2.4. Image from Collon et al. (2016).

arms can be actuated separately, which results in a movement of the mirror. With a suitable set of actuations, the mirror can be moved in six degrees of freedom. This mechanism allows not only to switch between the detectors but also provides the possibility to focus the whole instrument in orbit, and also to use dithering patterns by moving the mirror only, making an additional movement of the spacecraft superfluous for this purpose. The use of this system has more advantages - the abandonment of the MIP saves mass, which is important for the development of the mission. It also improves the mass distribution over the spacecraft and relaxes the structural requirements for the connection to the launch vehicle as well as for the spacecraft itself. The now static Focal Plane Module can be better controlled thermally, as a larger radiator area can be housed and flexible heat pipes can be rejected. Disadvantages are a complication of the X-ray baffle system and an increased mass for the magnetic diverters required to deflect charged particles coming from the mirror (Ayre et al., 2016).

2.3 *Athena*'s Instruments

The X-ray photons collected by the mirror are focussed to the other end of the spacecraft, where the Focal Plane Module is located. This part of the vehicle accommodates the scientific payload of the satellite, the two X-ray instruments. In the next sections, both the WFI and the X-IFU are explained with their principal features. A closer look into the specific physics of the detectors will be given in Chapter 3.

2.3.1 The WFI

The WFI planned for the *Athena* mission as described by Meidinger et al. (2016), Rau et al. (2016), and illustrated in Fig. 2.6 consists of two separate detectors. The first detector is designed to have a large field of view. It is made from four individual DEPFET-sensors (details of this detector type will be given in Sect. 3.2.2) which are combined to one large

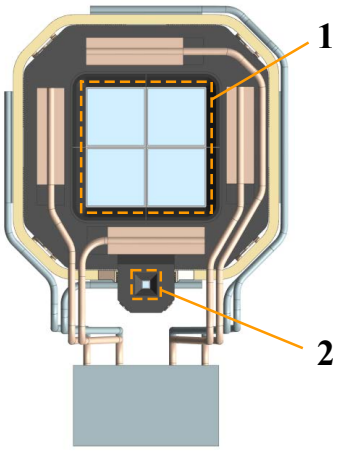

Figure 2.6: A view onto the current focal plane design of the WFI from the illuminated side. The large detector (**1**) consists of four DEPFET-sensors combined to a 2×2-array. The pixelated area of the sensors is smaller than the individual chips. This leads to a gap between the pixels of the four quadrants, forming a cross-like insensitive area in the detector. The small, high-count rate capable detector (**2**) is located a few centimetres to the side and is mounted slightly out-of-focus to decrease the pile-up for observations of bright point sources. Both sensors are held by a structural frame which is connected to heat pipes to cool the sensors and front end electronics. Image from Meidinger et al. (2016).

square array, covering a field of $40' \times 40'$ in the focal plane of *Athena*'s optics. Each of the four independent sensors has 512×512 pixels with a size of 130 μm×130 μm and is controlled by eight Switcher-A Application-Specific Integrated Circuit (ASIC)s. The read-out is performed by eight VERITAS 2 (Porro et al., 2014) ASICs per sensor (Meidinger et al., 2016). The sensors are operated in the rolling shutter-mode, which means that at the end of a frame, only one row is active for read-out at a time. Once the pixels of this row have been read out, the row is deactivated and a neighbouring row is read out. Because the edges of the individual sensors forming the quadrants are not pixelated, the integration of the four sensors to the large detector leads to a cross-like, insensitive area in the field of view. For observations, the attitude of the satellite can be used to compensate for this insensitive area. If the pointing of the telescope follows a suitable path on the sky over time, for example in the shape of a Lissajous curve, the insensitive area is effectively washed out over a large part of the observed region. This dithering could also be achieved by constantly moving the mirror with respect to the detector using the hexapod as explained in Sect. 2.2, instead of manipulating the attitude of the whole spacecraft (Ayre et al., 2016).

The second detector is smaller with only 64×64 pixels of the same size as the above. Its purpose is to provide additional high-count rate capability for bright point sources. To achieve this, the DEPFET-sensor is divided into two halves which are read out in parallel. This approach reduces the frame time length by a factor of two and enables the required time resolution of 80 μs. The count rate capability is further improved with the small detector being mounted slightly out-of-focus. The defocussing implies that the PSF as seen by the detector is wider than in the focal plane, but the photons collected by the mirror modules are spread over a larger area, reducing the effective count rate per pixel and thus pile-up. The optimisation of the WFI's small detector position is explained in detail in Sect. 5.3.

The two detectors, together with their front-end electronics, are mounted in a common camera head, which is surrounded by a graded Z-shield (Fan et al., 1996) for radiation protection. This shield is composed by layers made from different chemical elements, with decreasing atomic number Z towards the sensors. This design was shown to protect

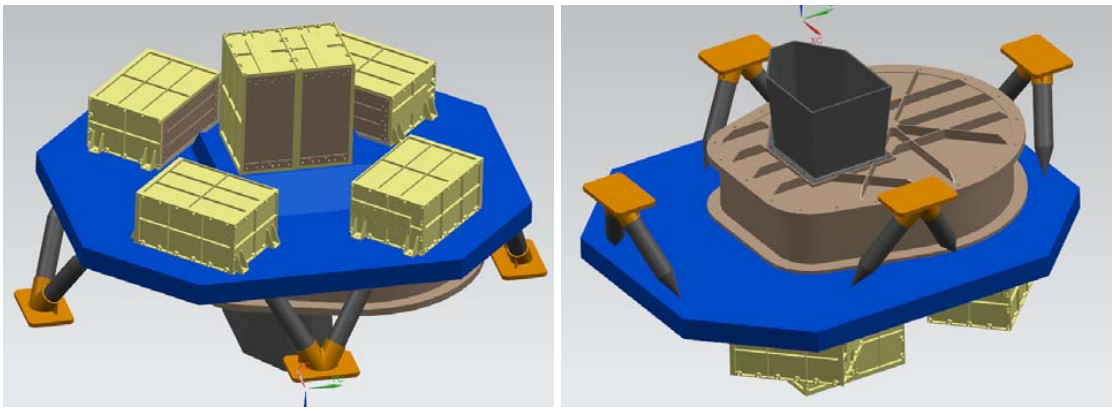

Figure 2.7: CAD-renderings of the WFI on its primary structure (blue). **Right**: The backside holds the six detector electronics boxes (yellow). **Left**: The detector and the graded Z-shield are encapsulated in the housing of the filter wheel (brown). The baffle (black) is mounted on top of the filter wheel. The structure is connected to the instrument platform with a framework (black struts and orange connectors). Images from Fürmetz et al. (2016).

effectively against different types of radiation (Fan et al., 1996). The shield has two holes, one for each detector, which open towards *Athena*'s mirror module. A filter wheel (Rataj et al., 2016) is placed above the holes, with four slots for different purposes. One slot holds a filter to block UV- and visible light. This filter is necessary as the sensors are not only sensitive to X-ray photons but also to low-energy radiation. As the amount of photons in the visible- and UV- range can be significantly higher than the number of X-ray photons, even the small signals produced by these low-energetic photons would add up to high signals during a frame, degrading the spectral resolution of the detector. The current design aims for a two-part blocking filter, with 90 nm Al being deposited directly on the sensor, and the filter wheel holding a foil of 40 nm Al on a 200 nm Polyimide

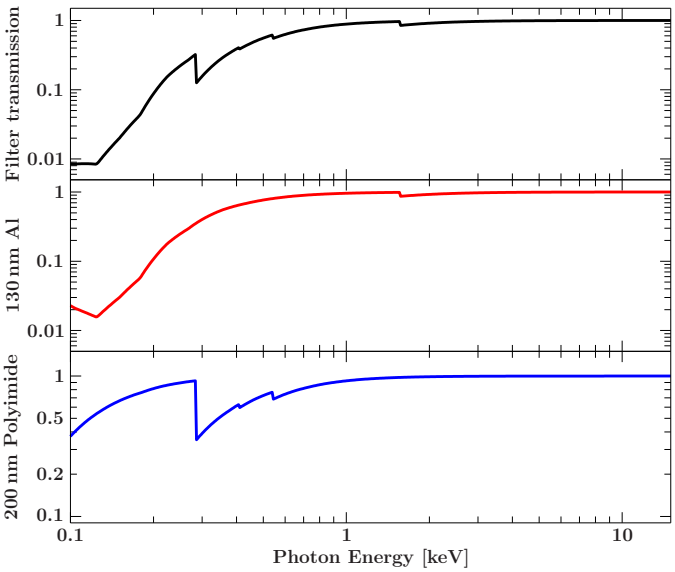

Figure 2.8: Transmissivity of the WFI's blocking filter. **Top**: The total transmissivity of the filter setup consisting of a total of 130 nm Al and 200 nm Polyimide. **Middle**: Transmissivity of a 130 nm Al filter. **Bottom**: Transmissivity of 200 nm Polyimide. Data from Henke et al. (1993, `http://henke.lbl.gov/optical_constants/`).

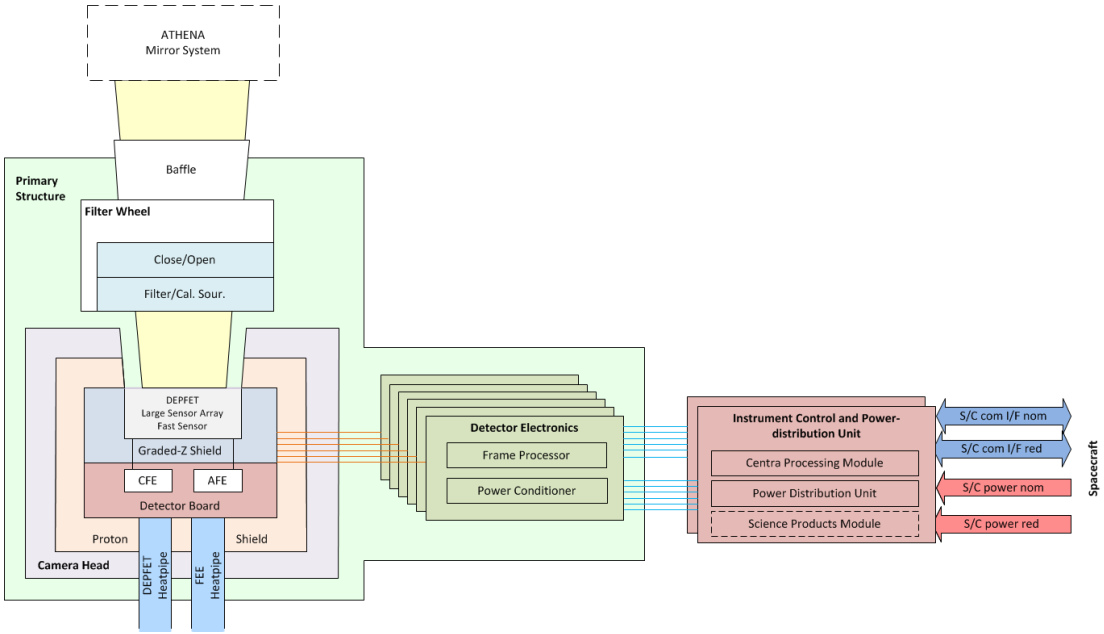

Figure 2.9: Block diagram representing the different parts of the WFI. The photons focussed by the mirror enter the instrument through the baffle and the filter wheel, before they hit one of the two detectors. These are encapsulated in the graded Z-shield inside the camera head. The signals are processed by the detector electronics and the ICPU, which forms also the link to the spacecraft. Illustration from Meidinger et al. (2016).

substrate (Meidinger et al., 2016). Together, the filter will block around seven orders of magnitude in the visual regime. The X-ray transmissivity of this setup is shown in Fig. 2.8. A second slot holds calibration sources for in-orbit calibration. A third slot is empty to allow evacuation of the filter wheel and camera head. Additionally, this slot can be used to observe astronomical sources with a smaller amount of total optical blocking filter thickness, helping to improve the effective area at low energies. The fourth slot is closed for protection of the sensors and to take measurements of the instrumental background.

The camera head and filter wheel are mounted on a support structure, which connects the camera to the satellite. It also holds the six detector electronics boxes. These boxes hold the electronics to supply the operating voltages and timing signals. The electronics accommodated in the boxes also digitize the analogue signals measured by the detectors. Further processing of the data is done inside the Instrument Control and Power Distribution Unit (ICPU), which also handles the thermal and filter wheel control (Plattner et al., 2016). A rendering of the current CAD model of the complete instrument assembly is shown in Fig. 2.7, and Fig. 2.9 gives an overview over the subsystems of the instrument.

The DEPFET sensors of the WFI are operated at a temperature of around 190 K to limit the damage caused by radiation. However, they are thermally coupled to the front end electronics which are operated at temperatures between 250 K to 290 K. This means that constant cooling of the system is required. The cooling is planned to be passive, meaning that no parts are moving and no consumables are used, such that the cooling system does

not limit the instrument's lifetime. Instead, radiator panels are used, which emit blackbody radiation into space by dissipating thermal energy. These radiators are mounted to the spacecraft and are connected to the instrument using constant conductance heat pipes (Fürmetz et al., 2016).

2.3.2 The X-IFU

The second instrument on board *Athena*, the X-IFU as described by Barret et al. (2016), is optimised to have an exceptionally high energy resolution of 2.5 eV at energies below 7 keV, covering an energy range from 0.2 keV to 12 keV. Nevertheless, it will be an imaging detector capable of making use of *Athena*'s spatial resolution to resolve the spectral variations of cosmic X-ray sources over their extent on the sky. To achieve these goals, the detector of the X-IFU is an array of individual Transition Edge Sensor (TES) pixels (Smith et al., 2016; Jackson et al., 2016). The current baseline for the detector, the Large Pixel Array (LPA) 2 (Barret, 2016), assumes the use of 3540 pixels, composed in a large hexagonal array. The pitch between the pixels is 260 μm, which is equivalent to an angular resolution of 4.5″ behind the 12 m focal length and slightly better than the required 5″. The full detector covers a field of view of 5′ (Smith et al., 2016). In addition to the requirements of energy and angular resolution, the X-IFU shall be able to handle bright sources with limited spectral degradation: For a flux of 1 mCrab, it shall be able to handle more than 80% of the counts as high-resolution events with a resolution of 2.5 eV. For sources with a brightness of 1 Crab, this fraction is allowed to decrease to 30%. The goal is still to provide more than 80% high-resolution events for sources with a flux of 10 mCrab. This requirement drives the development of alternative geometries with smaller pixels to distribute the counts over more sensors, as described by Smith et al. (2016).

The basic components of the instrument are shown in Fig. 2.10. The core of the X-IFU is the TES array. The basic principle of this sensor class will be explained in Sect. 3.3. The important aspect of its function for the system as a whole is the requirement of a very low operation temperature of only 50 mK (Charles et al., 2016). This has a huge impact on the design of the instrument. As Fig. 2.10 shows, several cooling stages are needed to reach and maintain the low temperature. The sensor is housed inside the cryostat on the Focal Plane Assembly as shown in the rendering of the CAD-model in Fig. 2.12. This also holds the Cryogenic Anti-Coincidence (CryoAC) (Macculi et al., 2016) and Cold Front End Electronics (CFEE) for the sensor and the CryoAC. These four components are all operated at the coldest region inside the cryostat at 50 mK. The CFEE is the first amplification stage for the signal measured in the TES pixels and requires the same low temperature as the sensor itself. The output of the CFEE is amplified again by a second stage at a higher temperature of 2 K, before it is guided out of the dewar to the Warm Front End Electronics (WFEE; Barret et al., 2016).

The low operating temperatures are generated by a complex cryochain, consisting of several coolers as described by Charles et al. (2016). Two-stage Stirling coolers and pulse tube coolers are used as precoolers. Their cooling powers reach from a few Watts to around 200 W, depending on the operating temperature. The Stirling coolers are used

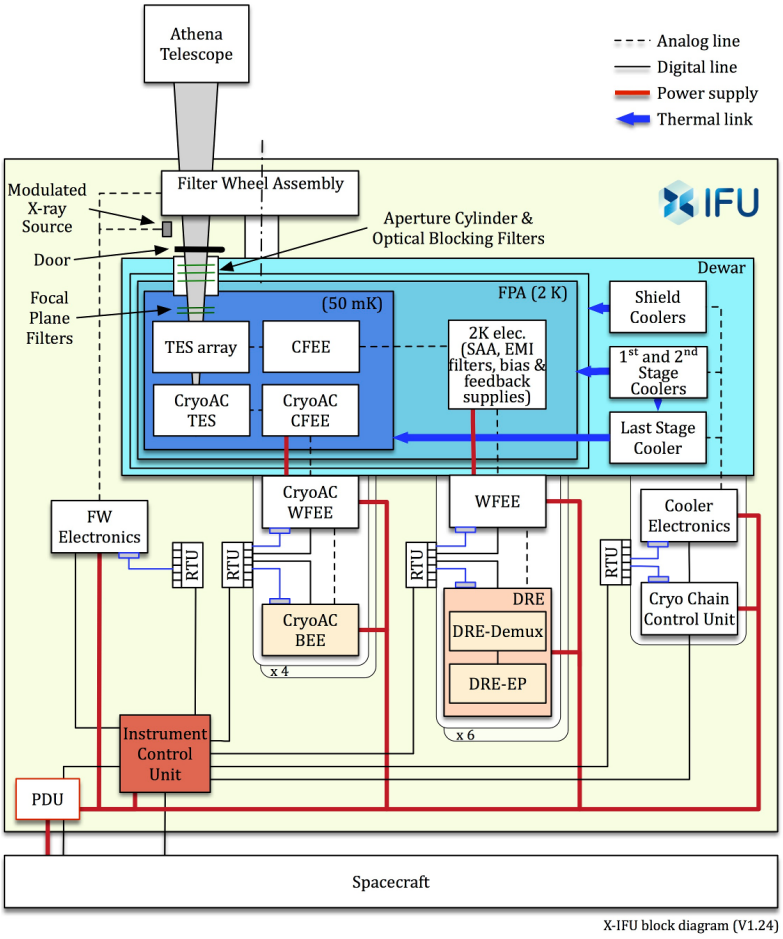

Figure 2.10: Block diagram of the X-IFU. The photons focussed onto the detector by the telescope (top) pass the filters inside the Aperture Cylinder and hit the TES array. This is operated at a temperature of 50 mK. Several cooling stages are required to reach this temperature, as illustrated by the blue shaded boxes. The cooling takes place inside the dewar, which is shown in Fig. 2.12. The instrument is linked to the spacecraft via the Instrument Control Unit and the Power Distribution Unit (PDU). The Modulated X-ray Source provides a calibration source for use in-orbit. Illustration from Barret et al. (2016).

in connection with 4 K Joule-Thomson (JT) coolers, each of which provides a cooling power of 40 mW at 4.5 K. The pulse tube coolers are used with 2 K JT coolers, which have a cooling power of 10–20 mW each. With these coolers, temperatures down to 2 K are reached. The operation of the sensor, the CryoAC and the cold front-end electronics at a temperature of 50 mK is achieved by the use of a ^{3}He sorption cooler coupled to an Adiabatic Demagnetization Refrigerator (ADR). This last stage can not be operated continuously but needs to be recycled after around 100 ks of operation (Charles et al., 2016; Nandra et al., 2014). Although the 50 mK cooling system is still in development, a model has shown to deliver a cooling power of 0.4 μW at 50 mK and 14 μW at 300 mK. All of the coolers except for the last stage are planned to be redundant (Charles et al., 2016). They are arranged at the outside of the dewar around its circumference, as shown in Fig. 2.12. The different temperature regimes inside the cryostat are separated from each other by several shields (Lam Trong, 2016).

To provide access for the X-rays to reach the sensor, the cryostat has to have an entrance window. In this hole, the Aperture Cylinder is mounted which holds several filters. These filters do not only shield the detector from radiation at low energies in the radio, infrared, visible and UV regime but they also need to follow the strong thermal gradient down to 50 mK. The current baseline filter setup for the X-IFU assumes a series of five filters. They

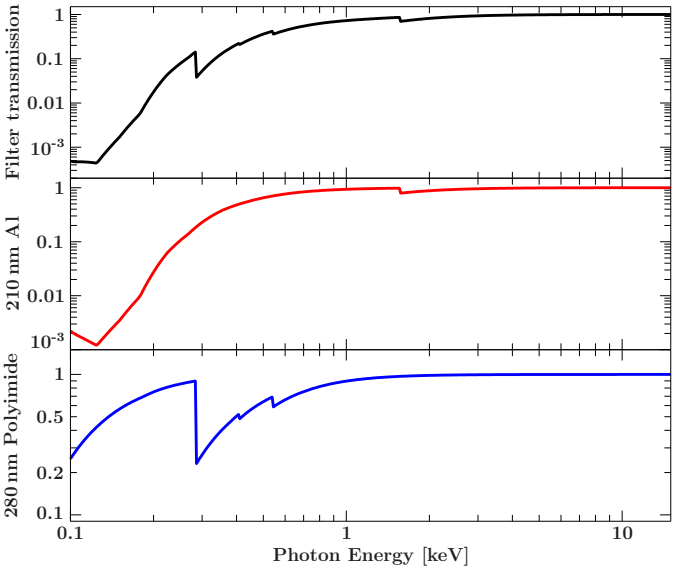

Figure 2.11: Transmissivity of the X-IFU's fixed filters. **Top**: The total transmissivity of the five filters consisting of a total of 210 nm Al and 280 nm Polyimide. Additionally, two of the filters are strengthened by a support mesh of 10 μm thick Polyimide with an open fraction of 93%. **Middle**: Transmissivity of 210 nm of Al. **Bottom**: Transmissivity of 280 nm of Polyimide. Data from Henke et al. (1993, `http://henke.lbl.gov/optical_constants/`).

have a total thickness of 280 nm Polyimide and 210 nm aluminium. To stabilise the two largest filters, support structures are needed. These structures are assumed to add a total thickness of 10 μm of Polyimide at 7% of their surface, while 93% of the filter area are not affected by this additional absorption (Barret et al., 2016). The transmissivity of this filter setup is shown in Fig. 2.11.

In addition to the fixed filters in the Aperture Cylinder, a filter wheel is mounted in front of the entrance window. This filter wheel offers space for up to eight filter positions. For launch, a Molybdenum filter opaque to X-rays closes the entrance window and protects the detector. This can also be used for in-flight background calibration measurements. A second filter place is left open for the observation with the fixed filters only. For the observation of very soft and bright X-ray sources, two Beryllium filters with different thickness are provided. These shield the detector from a part of the radiation below 3 keV which could lead to its degradation. For observations of bright sources, a neutral density blocking filter is added to the filter wheel. The desired blocking factor is still under investigation, with values up to 100 under consideration. Observations of sources with bright counterparts in the visual- and Ultraviolet (UV)-regime require the option for additional optical blocking filters. Two of them will be provided in the filter wheel.

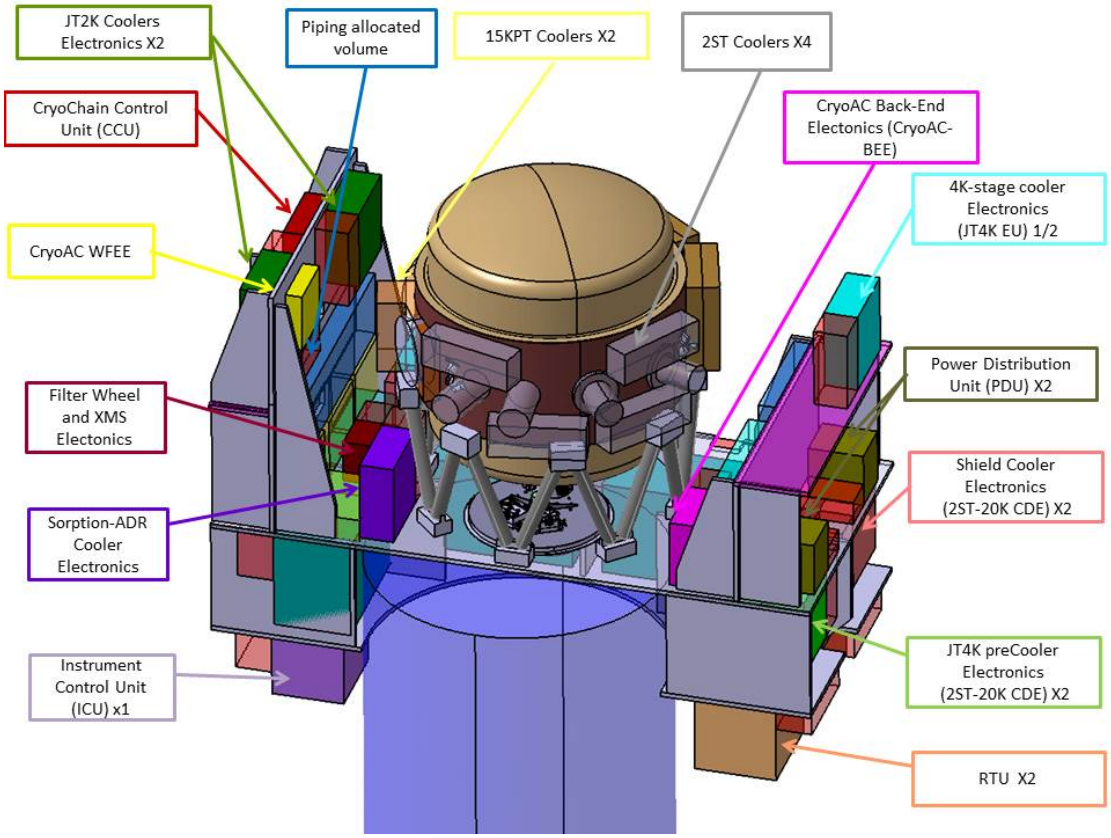

Figure 2.12: The CAD model of the X-IFU as presented to the Mission Consolidation Review in May 2016. The sensor is accommodated in the dewar (light brown). The low temperature necessary to operate the TES requires a complex cooling system. The coolers are mounted to the circumference of the cryostat, with the electronics and control units placed in racks around the dewar. Photons come from the bottom. Picture taken from Barret et al. (2016).

3 Simulations for *Athena*

During the last century, our understanding of physics has grown enormously. In 1901, Planck's article on the radiation of black bodies was published (Planck, 1901), opening the field of quantum mechanics, and in 1905, Einstein introduced special relativity (Einstein, 1905). A lot of progress was made in engineering, too: the development of aircraft, space travel, nuclear power plants and computers revolutionised our daily life. Both of these developments have one thing in common: They make further progress more and more complicated and expensive. This trend changes the way scientific work is performed to achieve even more insight into highly complicated research matters. Due to the huge investment of man power, work, and money which are necessary to make progress in fields like particle- or astrophysics, large institutions and consortia are formed for being able to handle and share the rising costs. Examples for this development are the European Organization for Nuclear Research (CERN)[1], a multi-national research institute for particle physics, or the consortia designing modern astronomical spacecraft such as *Athena*[2] and its instruments.

In order to lead to a successful accomplishment of the goals set for such a consortium, not only careful planning and a good design process is necessary, but also the continuous validation of the feasibility is required. Computer simulations are an enormous help in these situations: Firstly, they can be used to optimise a setup during the design process. Secondly, they allow to model the current design of a given device and test it in the computer, before any component has been produced. Furthermore, with a good knowledge of an astronomical instrument such as eROSITA on *Spectrum-Roentgen-Gamma (SRG)* or the X-IFU on board of *Athena*, the limits of the detector's capability can be studied and observational biases can be described, even before any real data is taken (see, for example, the study conducted by Borm et al., 2014 on galaxy cluster properties as measured with eROSITA). This also means that data processing algorithms can be tested, and analysis pipelines can be optimised for simulated data with known properties instead of real data,

[1] `http://home.cern/`
[2] `http://www.the-athena-x-ray-observatory.eu/`

which may otherwise lead to subjective results more resembling the scientist's wishes than the real physics.

In the chapters 4 and 5, such detector simulations are presented in detail. In chapter 4, the feasibility of the search for missing baryons with the X-IFU is tested, one of the main science goals of the mission. This example shows what can be learned from detector simulations about observations more than ten years in the future. Chapter 5 on the other hand is one of the cases where the detector hardware design and simulations go hand-in-hand. The first study described in chapter 5 validates the performance of the WFI as planned, while the second study picks up these results to further optimise a design parameter, which is then adopted in the development process. But before these simulations are presented and discussed, the software used for the calculations is presented and the models for the detector are described in the following sections.

3.1 SIXTE: Simulating an X-ray Observatory

The matter of detector simulations covers a broad field. They can be as simple as XSPEC's (Arnaud, 1996) `fakeit`-command, which generates a statistical realisation of a given X-ray spectrum with an additional background[3], but they can also reach to a very elaborate model of a scientific detector in a three-dimensional software such as Geant4 (Agostinelli et al., 2003; Allison et al., 2006).

All of these approaches have their justification. For the case of simulations of large observation campaigns, small detector effects can often be simplified and expressed through calibration files such as the Auxiliary Response File (ARF) and Redistribution Matrix File (RMF) together with other effects. On the other hand, a very in-depth description of the physical composition of a detector and its environment may be needed for other kinds of simulations, such as the prediction of instrumental background events. The different approaches lead to a high specialisation of the simulation software, and make a strong separation between hardware simulation and observation simulation. SImulation of X-ray TElescopes (SIXTE) as developed by Schmid (2012) aims to close the gap between these two directions. It offers a number of tools which can be used to perform observation simulations for long periods in the simulated time, as for example the complete eROSITA four year all-sky survey, but with a good description of the detector properties. Furthermore, it allows to use the SIMulation inPUT (SIMPUT) file (Schmid et al., 2013) to define the astronomical sources in a very flexible way. This format is also compatible with other X-ray simulation programs such as SIMX (Smith, 2013) and MARX (Davis et al., 2012).

SIXTE is used to study the performance of the *Athena* mission with its two instruments (Wilms et al., 2014). Its basic processing layout is shown in Fig. 3.1. As can be seen, SIXTE tries to mimic the process which is happening in the real world. It starts with a catalogue of X-ray sources to simulate individual photons. A description of the instrument's imaging system is used to propagate the photons onto the detector, where a model of

[3] `https://heasarc.gsfc.nasa.gov/xanadu/xspec/manual/XSfakeit.html`

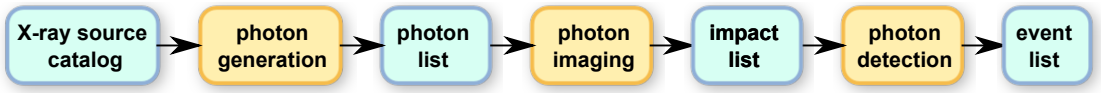

Figure 3.1: The basic layout of the standard SIXTE processing pipeline. In blue boxes, data products, either for in- and output or for optional intermediate files are shown. Yellow boxes depict the three main processing steps. Modified after Schmid (2012).

the sensor is used to create an event list, which can be analysed like real data. In the next sections, a more detailed explanation on the function of the steps is given. More information about the algorithms used by the software can be found in Schmid (2012).

3.1.1 The Source Catalogue

Apart from the instrument description, the SIMPUT source catalogue (Schmid et al., 2013) is the astrophysical input to SIXTE. It consists of a list of sources, each of which is defined by its position on the sky in Right Ascension (RA) and Declination (Dec), its flux in a given reference energy band and a spectrum. In addition, optional information about its extend on the sky can be given in terms of a FITS-image, and the temporal variability of the flux can be described by, for example, a light curve.

A strength of the format is the reusability of information. Instead of saving a spectrum for each source on its own, only links are given in the catalogue. This means that, in a simple catalogue, all sources can use the same spectrum, but it has to be saved only once. This makes it possible to create very large catalogues with several thousands of sources, as for example in Brand (2011). The same method is used for images and timing information. In the case of images, additional fields in the catalogue can be used to specify individual values for scaling and rotation of the pictures to gain more variability by using the same image again and again. Furthermore, a SIMPUT-catalog can be used for simulations of every instrument within SIXTE, provided the spectra contained in the catalogue cover the instrument's energy band. This makes the format very useful to compare observations between different telescopes. An in-depth discussion about the details of the file format can be found in the format definition document (Schmid et al., 2013).

3.1.2 The Photon Generation

After the launch of a simulation run with SIXTE, three main steps are successively executed, as shown in Fig. 3.1. The first task is to use the SIMPUT source catalogue to generate a sample of photons. Each photon within the software is described by three properties:

- arrival time (t_{photon})
- direction of origin (RA, Dec)
- energy (E_{photon})

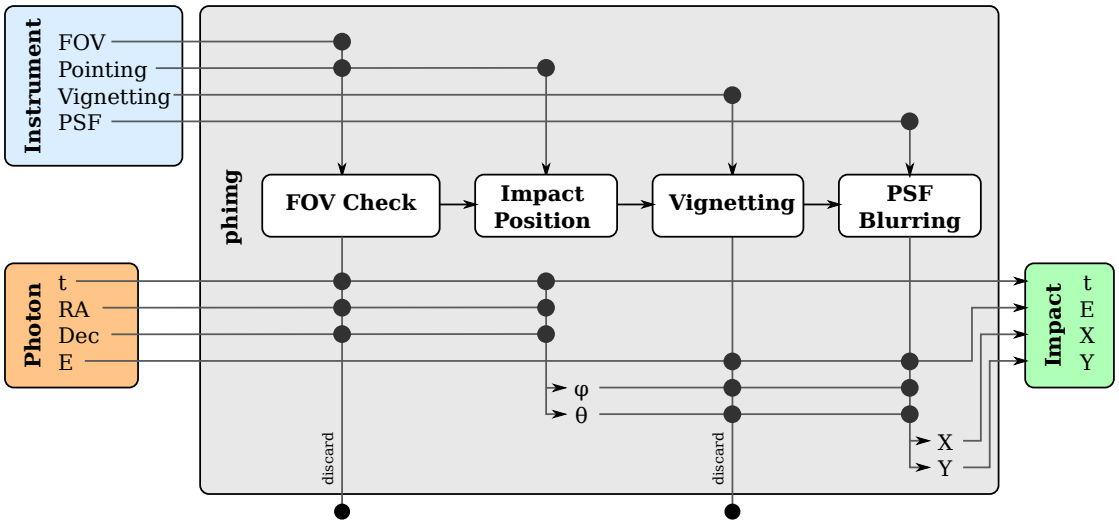

Figure 3.2: Block diagram of the photon imaging step in SIXTE. The blue box shows the information on the instrument necessary as input for this simulation step. The orange box symbolises a single photon as generated in the first simulation step. Its properties are translated into the observables on the detector plane, as depicted by the green box. If the photon lies outside the field of view or is rejected due to high vignetting, it is discarded. Graphic from the SIXTE manual (Brand et al., 2016a).

In the case of sources with constant brightness and spectral properties, the arrival times are randomly drawn to follow a Poisson distribution (Schmid, 2012). The energy of the photon is chosen randomly, too, with the energy spectrum of the source taken as the Probability Density Function (PDF). If the source has an image assigned for its flux distribution on the sky, the same is true for the photon's direction. Instead of the energy spectrum, the image is interpreted as a two-dimensional PDF.

To save calculation time and memory, not all sources in the catalogue emit photons all the time. Instead, the attitude information is used together with the field of view of the telescope to select all sources visible at a given time. Especially for all-sky observations, this significantly improves the performance of the simulation. Furthermore, the effective area or ARF of the instrument is already combined with the energy spectrum of each source to simulate only those photons which will later be detected. This means that the list of photons produced by this simulation step is already instrument specific and can not be used for other detectors, for example as a photon list in a SIMPUT catalogue. The exact algorithms used to draw the photon properties and descriptions of the algorithms used for sources with variable brightness can be found in Schmid (2012).

3.1.3 The Imaging Process

After the photons are generated, they need to be imaged onto the detector plane. This is the second step of the simulation and is illustrated in Fig. 3.2. It uses four properties of the instrument:

- field of view

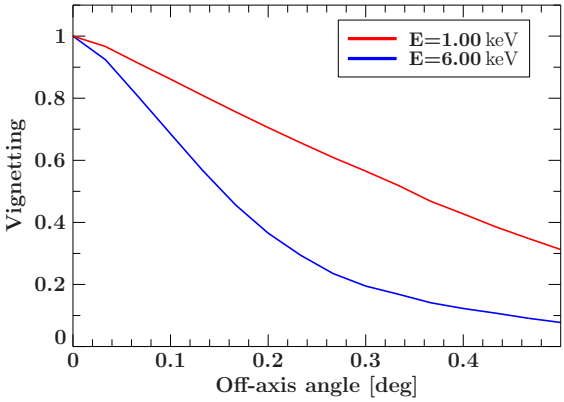

Figure 3.3: Vignetting function for *Athena*'s proposed mirror. Due to the nearly rotationally symmetrical construction of the mirror system, the vignetting only depends on the energy of the photon and the off-axis angle. The vignetting is normalised to unity on the optical axis, where the full effective area is reached. As the off-axis angle increases, the mirror reflectivity drops and the vignetting function decreases. For high photon energies, the vignetting drops faster than for low energies, which can be seen by the two curves, representing the vignetting for 1 keV and 6 keV photons.

- pointing direction
- vignetting function
- PSF

The field of view and the attitude are used to check again if a photon is visible for the detector. This is useful if a photon list is reused with slightly different parameters. The vignetting and the PSF however model the imaging qualities of the optical system. After the field of view-check, the ideal impact position of the photon on the detector plane is calculated using geometrical optics. This is done by converting the photon's RA and Dec, measured in the celestial coordinate system to an off-axis angle θ and an azimuthal angle φ, measured in the coordinate system of the instrument.

The vignetting function describes the effective area for an energy, E, and a combination of θ and φ, relative to the respective on-axis effective area described in the ARF. Usually, the energy dependent vignetting function is unity on the optical axis and drops with increasing off-axis angle. In the case of rotation symmetric optical systems which are a good model for a typical X-ray mirror such as for *Athena* (see Sect. 2.2), the dependence on the azimuth angle φ can be neglected. In SIXTE, the vignetting function can be described by a discrete, three dimensional array which is internally interpolated linearly. For each simulated photon, the vignetting function is evaluated, which results in a value between zero and one. A random value is drawn from a uniform distribution between the same limits. If the random value is higher than the vignetting, the photon is discarded. Otherwise, the photon can be detected and the simulation continues (Brand et al., 2016a; Schmid, 2012). The vignetting function of *Athena* is shown in Fig. 3.3.

The Point Spread Function (PSF) is the image of a point source on the sky as seen by the detector. It represents the discrepancy of a real mirror system from a perfect one, which would image a point source to an infinitely sharp point on the focal plane. Due to the energy dependent mirror reflectivity, the PSF is usually a function of the photon energy. In addition to this, the function depends on the direction of the source relative to the optical system, represented by the angles θ and φ as before. An X-ray mirror can be optimised for sharp on-axis images, but can have a broader PSF in the outer regions of the field of view. In SIXTE, the PSF is represented by a collection of images, one for each combination of the photon energy E_{photon} and the angles θ and φ. Example PSF

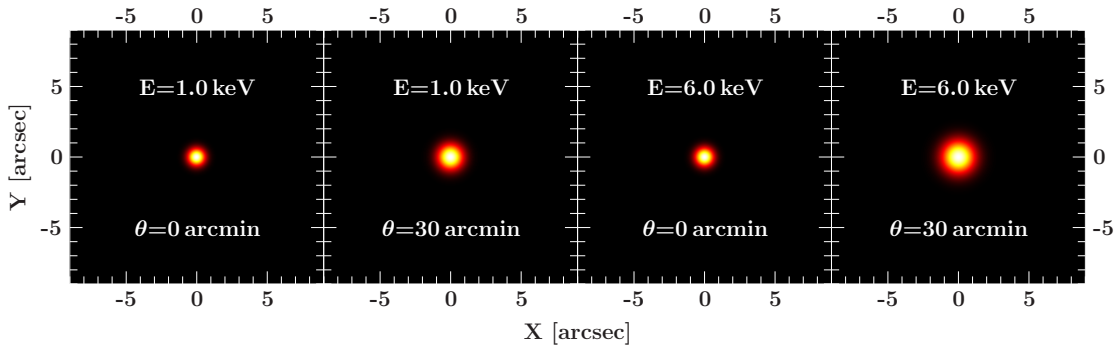

Figure 3.4: Four example PSF images for *Athena*'s proposed mirror as used for the simulations. The width of the PSF depends on the off-axis angle and the photon energy. The sharpest picture of a point source can be obtained at the optical axis. At higher off-axis angles, the width of the PSF increases, which leads to a lower resolution at the outer areas of the field of view.

images for *Athena* as used in this thesis are shown in Fig. 3.4. For each photon, the two best-matching PSF entries are selected and interpolated linearly. The resulting image is interpreted as a PDF for an offset to the impact position of the photon on the detector plane, represented by the coordinates X and Y (Schmid, 2012).

3.1.4 The Detection Step

The third step in a basic SIXTE simulation represents the detection of the photons and thus models the processes inside the sensor during its operation. The detector is defined in a SIXTE XML file together with the calibration files of the instrument. It offers options to describe its geometry as well as its read-out properties. For example, the operation of a CCD in which charge is moved from pixel to pixel until it reaches a frame buffer can be emulated by a specification of line shifts and waiting times in between (Schmid, 2012). The format has also be extended to describe the read-out timing properties of DEPFET sensors, as will be explained in the following sections. A modified format also allows to define more complex geometries and functions necessary for the simulation of TES detectors as used in the X-IFU.

The most obvious process in the detection step is the transformation from a photon's impact position, X and Y, to the coordinates of an affected pixel, $RAWX$ and $RAWY$. However, this is only a small part of the photon detection. In the case of CCD or DEPFET sensors, the primary photon creates a charge cloud, which may be distributed over several pixels. Thus, one photon can cause events in multiple pixels. This effect is taken into account by SIXTE (Schmid, 2012). It influences the quality of the spectra and can be partially neutralised by a so-called pattern analysis of the resulting event list, which searches for multi-pixel events and recombines them to reconstruct the original photon's impact position and energy. The effect of this charge splitting and the pattern analysis on astronomical observations will be described in detail in Chapter 5. The charge distribution in the detector caused by a one-photon event is described via an analytical function,

such as a two-dimensional Gaussian function. It is integrated over the areas of the four nearest neighbouring pixels, with the resulting integrals representing the charge fractions captured inside the respective pixels. This calculation assumes that the size of the charge cloud is much smaller than a pixel, otherwise parts of the charge could could reach into even more pixels.

In a basic SIXTE simulation, the initial photon energy is spread over the four nearest pixels, according to the relations of the integrated charge cloud. However, the sum of these energies is still the exact photon energy. To account for imperfections of the measurement process, the energy detected in a pixel is randomised according to the RMF of the detector (Schmid, 2012). The RMF is a two dimensional matrix which gives the Probability Density Function (PDF) to measure a true energy of E_{true} in an energy channel representing a value of E_{measured} (George et al., 2007). For an ideal detector, E_{true} would always be exactly E_{measured} and the RMF would be a pure diagonal matrix. A widening of the diagonal due to, for example, Fano and electronic noise, or the additional appearance of off-diagonal elements as seen from an escape peak, represent physical processes inside the detector, which lead to a degradation of the measured signal (Eggert et al., 2006). The use of the RMF provides a fast and efficient way to model such effects in SIXTE. However, some detector types require a more sophisticated solution. The modular approach of SIXTE allows to switch to more detailed and complex detector simulations if necessary, such as for the TES–detectors used by the X-IFU as will be described in Sect. 3.3.

3.2 The Detector Model of the WFI

The WFI consists of two independent detectors as discussed in Sect. 2.3.1. Both of them are implemented in SIXTE as downloadable instrument setups within the SIXTE-*Athena*-package[4]. In the current version, the package provides setups for the large and fast detectors for two mirror configurations and either with or without the external filter in the filter wheel. Each of these configurations comes with two descriptions for the large detector, differing only in the alignment with respect to the optical axis, as well as a representation of one of the large detector's sensors in a 16-row window mode for bright sources. The small detector is represented by one configuration, which assumes one read-out row per detector half as described in Sect. 2.3.1 and a defocussed mounting of 35 mm. As will be shown in Sect. 5.3, this is the optimum position to observe bright sources. In the following sections, the chip geometry, the principles of the DEPFET-technology and the implementation of the read-out cycle in SIXTE is explained in detail.

3.2.1 The Sensor Geometry and Timing Parameters

The geometry of the two WFI-detectors closely follows the parameters of the real instrument, as described in Sect. 2.3.1. The four sensors of the large detector are implemented separately and can be used either one at a time or all together by the appropriate SIXTE-

[4] `http://www.sternwarte.uni-erlangen.de/research/sixte/simulation.php#Setup`

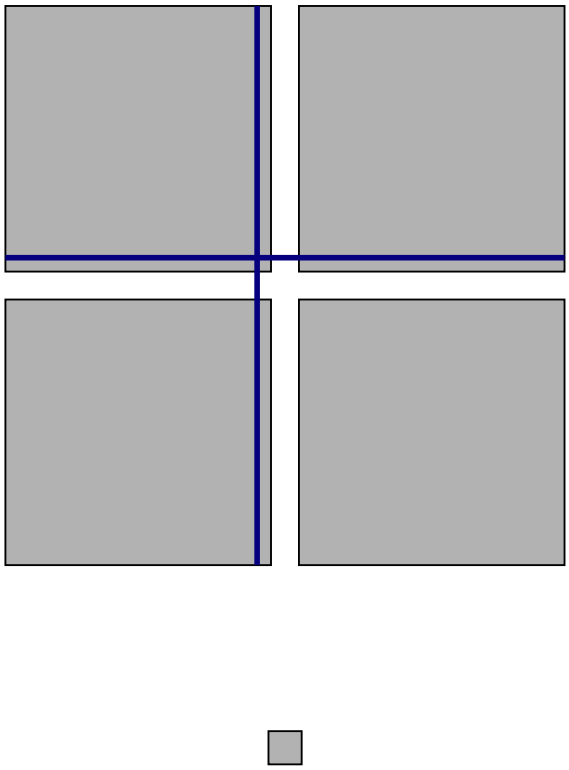

Figure 3.5: The geometrical configuration of the current implementation of the WFI in SIXTE. The large main detector is composed from four individual sensors, measuring 512×512 pixels each. Each pixel has a size of 130 μm×130 μm, so the total width or height of the quadratic sensors is 66.56 mm. Due to the finite edge size of the sensors, a gap of 7 mm is required between them. This number is a preliminary estimate and may change for the final detector. Not to lose the area with the lowest vignetting and the sharpest PSF, the whole array is shifted with respect to the optical axis. The blue cross marks the simulated point of intersection of the optical axis with the sensor surface. The offset is assumed to be around 10 mm diagonal from the array's centre. With a focal length of 12 m for *Athena*, the large WFI-detector covers a field of approximately 40'×40' on the sky. For bright sources, it has an additional 64×64-pixel sensor, which is depicted in scale to the main detector below. Due to the lower number of pixels, it can be read out faster, which reduces spectral degradation due to pile-up. This can be further improved with the small sensor being mounted outside the focal plane, such that the PSF is wider and the light from point sources is distributed over a larger number of pixels.

tools. Each quadrant is represented by an array of 512×512 pixels, with a pixel size of 130 μm×130 μm. The resulting sensor size is a square with an edge length of 66.56 mm for each quadrant. The standard setup for this detector assumes a gap of 7 mm between the pixelated area of two adjacent sensors due to the pixel edges and the small physical gap between them. This estimate is preliminary and may be different in the final stages of the detector design. Overall, the pixelated area of the WFI in SIXTE is a square with a size of 140.12 mm×140.12 mm, which is equivalent to a field of approximately 40'×40' on the sky with a focal length of 12 m. If the centre of the large detector was aligned exactly with the optical axis, the area with the lowest influence from vignetting effects and with the best PSF would be lost in the insensitive area formed by the gap between the quadrants. This is counteracted by a slight shift of the whole array, 10 mm diagonal with respect to the square detector layout. This is illustrated in Fig. 3.5. Additionally, the SIXTE instrument package also comes with a version in which the square array is perfectly aligned to the optical axis, which should only be used in special cases. The read-out cycle for the large detector in SIXTE assumes a total frame time of 1.28 ms, which is the result of a continuous operation in the rolling shutter mode and a read-out time per row of 2.5 μs. The total frame time can be reduced to 40 μs with the 16 row window mode.

Figure 3.5 also shows the fast detector in scale to the large detector. It is implemented as a 64×64-array of the same 130 μm×130 μm-pixels. This results in a total size of 8.32 mm×8.32 mm, corresponding to a field-of-view of $2'\,23'' \times 2'\,23''$ on the sky. However,

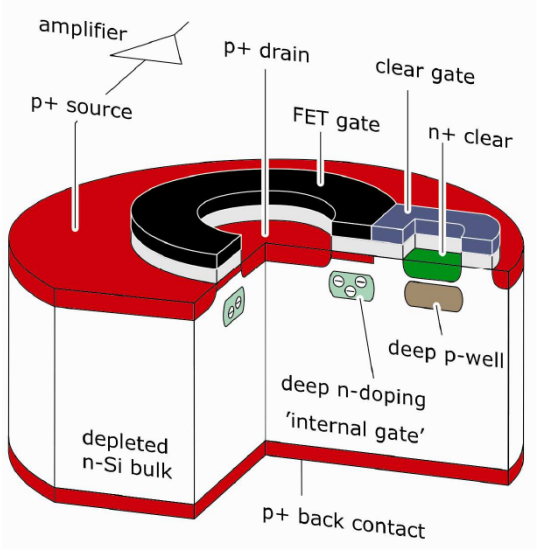

Figure 3.6: The principal composition of a DEPFET-pixel. Alternating p-, n- and p-doping of the silicon and suitable back and front voltages deplete the bulk completely and shift the maximum of the electric potential inside the bulk towards the front side. The hole- and electron pairs created by an X-ray photon are separated in this field, and the electrons drift to the maximum of the potential below the front side. An additional deep n-doping forms the internal gate, in which the electrons are trapped during the exposure time. On top, a p-channel MOSFET is formed by the source-, gate- and drain contacts, with which the charge is amplified for the read-out. The additional n-channel clear-MOSFET, consisting of the clear gate and clear contacts, allows to remove the charge after the measurement. Image from Lechner et al. (2006).

the fast detector will not be used for imaging observations but only for studies of bright sources with a too-high count rate for the large detector. To achieve the best results possible for very high photon numbers per time, the fast detector is mounted defocussed, as will be explained in Sect. 5.3. This is modelled by an appropriate set of out-of-focus PSFs in SIXTE. With a read-out time per row of again 2.5 μs and two read-out rows per detector half, the frame time of the fast detector is 80 μs.

3.2.2 Principles of DEPFET-sensors

In the previous sections, the WFI has often been identified as a DEPFET-detector. In the following, the principles of this detector type will be explained, with a focus on the effects which influence astronomical observations and which are necessary to be included in the simulations. The principle idea of the Depleted p-channel Field Effect Transistor (DEPFET) has first been described by Kemmer & Lutz (1987). The scheme of a modern implementation is shown in Fig. 3.6. The core of the concept is to bring the first amplification stage for the charge produced by a photon closer to the place of its creation. In the case of a DEPFET, this is achieved by placing a p-channel MOSFET in each pixel.

A standard Metal-Oxide-Semiconductor Field-Effect Transistor (MOSFET) uses the field effect to generate a conducting layer below the gate, which allows a current to flow from the source to the drain. This makes it possible to control the source-drain current by the voltage applied to the gate. The DEPFET extends this model by an additional, internal gate, which collects the electrons produced by the photon to manipulate the transistor's conductivity and thus the current.

As Fig. 3.6 shows, the largest part of a DEPFET consists of silicon in differently doped layers. The main part is formed by the n-doped bulk in the middle. It is surrounded by thin, p-doped layers at the front and back. Contacts at these three layers are connected to potentials which completely deplete the bulk. This process is known as sideward deple-

tion and was first proposed by Gatti & Rehak (1984). When a photon interacts with the silicon, it creates electron- hole-pairs, which are separated in the electric potential. The holes drift towards the negative back- and front contacts, but the electrons are trapped in the bulk at the maximum of the potential. To shift this maximum towards the region below the front side, the back contact is connected to a more negative potential than the front contacts. An additional deep n-doping forms the internal gate, which increases the strength of the potential maximum and helps to bring it to a well-defined region near the surface. Above the internal gate, a FET gate is added above the p-layer, separated from the silicon by a thin insulating layer. The gate is designed in such a way that it divides the surface of the silicon geometrically into two regions, the drain and the source. A suitable set of voltages applied between the source, gate, and drain contacts enables a current flow from the drain through the conducting layer below the gate to the source. The amount of additional electrons caught in the internal gate further influences the conductivity of the FET, which enables the measurement of the number of electron- hole-pairs produced by the photon and thus its energy. This is achieved by two measurements, during which the current through the MOSFET is integrated individually. At the end of the exposure time, the electrons produced by a photon are collected in the internal gate, but the transistor is not yet conducting. Only when a negative gate-source voltage is applied, a current flows through the FET, which is proportional to the sum of the field induced by the gate and the internal gate. An integration of this current over a certain time results in a charge proportional to the sum of these fields. To determine the amount of charge caused by the gate's field, the current is integrated over the same time again, but after the electrons from the photon have been removed from the internal gate. The difference between both integrals is now only proportional to the amount of charge which has been removed from the internal gate between both measurements and a gain factor. The removal of the electrons in the internal gate is accomplished by the clear gate and the clear, which form a unit similar to a n-channel MOSFET together with the internal gate. Between both integrations, high voltages are applied to the clear gate and the clear. The first one creates a conducting channel between the internal gate and the clear by using the field effect, just as the gate does during the integration times. The second voltage makes sure that the electrons arriving at the clear are removed from the detector.

This concept unifies the photon–matter interaction region and the first amplification necessary to measure small amounts of charge as created by single photons. To use this technology in imaging instruments, a large number of these units need to be placed side-by-side in an array structure, where they form individual pixels of a larger detector, as shown in Fig. 3.7. To avoid charge carriers travelling over pixel borders, additional channel separators are placed on the surface. These are connected to a low electric potential which repulses electrons from the area between the pixels to define the borders. To simplify the wiring for large sensors, the gate, drain, clear gate and clear contacts of all pixels in a row can be connected, as can the source contacts of the pixels in a column. These connections of the clocked potentials synchronises the read-out of all pixels in a row, while the signals of the individual pixels are measured in different channels connected to the respective sources. The WFI will use this technique in both detectors.

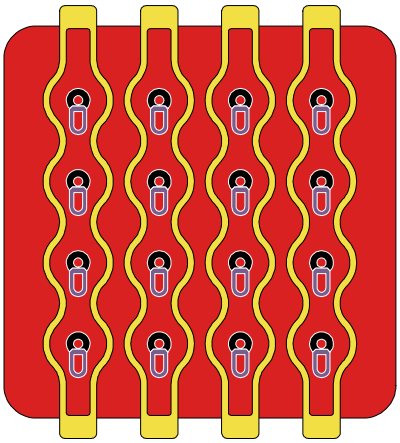

Figure 3.7: A sketch of a 4×4-pixel DEPFET-matrix. The individual pixels consist of DEPFET-units as shown in Fig. 3.6. The gates are ring-like structures (**black**), the clear gates are connected to them (**purple**). The individual pixels are composed in a square grid. The separation of the pixels is achieved by adding the channel separators (**yellow**), which build up a potential sink between the pixels to define the borders. The sensor design shown here is similar to the matrices used in Chapter 6. For these sensors, the gate, drain, clear gate and clear contacts are connected row wise, perpendicular to the channel separator's main axis (wiring is not shown). Only the sources are connected column wise, such that the signals of the individual pixels can be fed into different channels of the read-out electronics. This synchronises the read-out of all pixels in a row and simplifies the wiring for large matrices.

3.2.3 The Implementation of Misfits in SIXTE

As discussed in Sect. 3.2.2, a DEPFET measures the charge produced by a photon with two integrations. Between both integrations, a high voltage is applied to the clear contact of the pixel, which removes the charge from the internal gate of the pixel. This means that the first integration integrates the charge from the photon q_{photon} as well as the baseline signal q_{baseline} over a time $t_1 - t_0 = t_{\text{int}}$. As q_{photon} has been removed, the second integration only measures q_{baseline} during the time $t_4 - t_3 = t_{\text{int}}$. The subtraction of the two integration results yields a measurement that is proportional to the charge produced by the photon and a gain factor.

This is true as long as the photon hits the detector during the normal exposure time, and not during the active read-out of the affected pixel. If the charge is produced during the read-out process, so-called misfits can be produced. These are incompletely measured events which degrade the spectra. Figure 3.8 illustrates the processes taking place during the read-out. In the case of a photon impact during the first integration, the integration already started before, and the measurement will be incomplete. Thus, the baseline subtracted measurement is smaller than expected for the respective photon energy. A photon arriving after the first integration is completed may create even stranger signals: The first integration was not affected by this impact at all. However, if the charge is not removed completely by the clear, the signal present during the second integration is not only q_{baseline}, but features also a charge from the photon. Thus, the second integration measures a higher value than the first, and after the baseline subtraction, an event with negative sign is detected. As the charge can not be removed after the clear period, it is carried over into the next frame, where it is measured again, but with a positive sign. If the impact happens at the beginning of the clear shortly after t_1, the surviving charge is small as the attraction of the clear contact is high to allow a complete removal of the charge in a short time. However, the finite potential difference and extent of the charge cloud mean that this clear process is not instantaneous but takes a small amount of time. Thus, as the charge is produced more and more towards the end of the clear period $t_1 + t_{\text{clr}} = t_2$, more and more charge is left inside the pixel, and the measurement brings a value down to $-q_{\text{photon}}$. After the clear period and until the beginning of the second

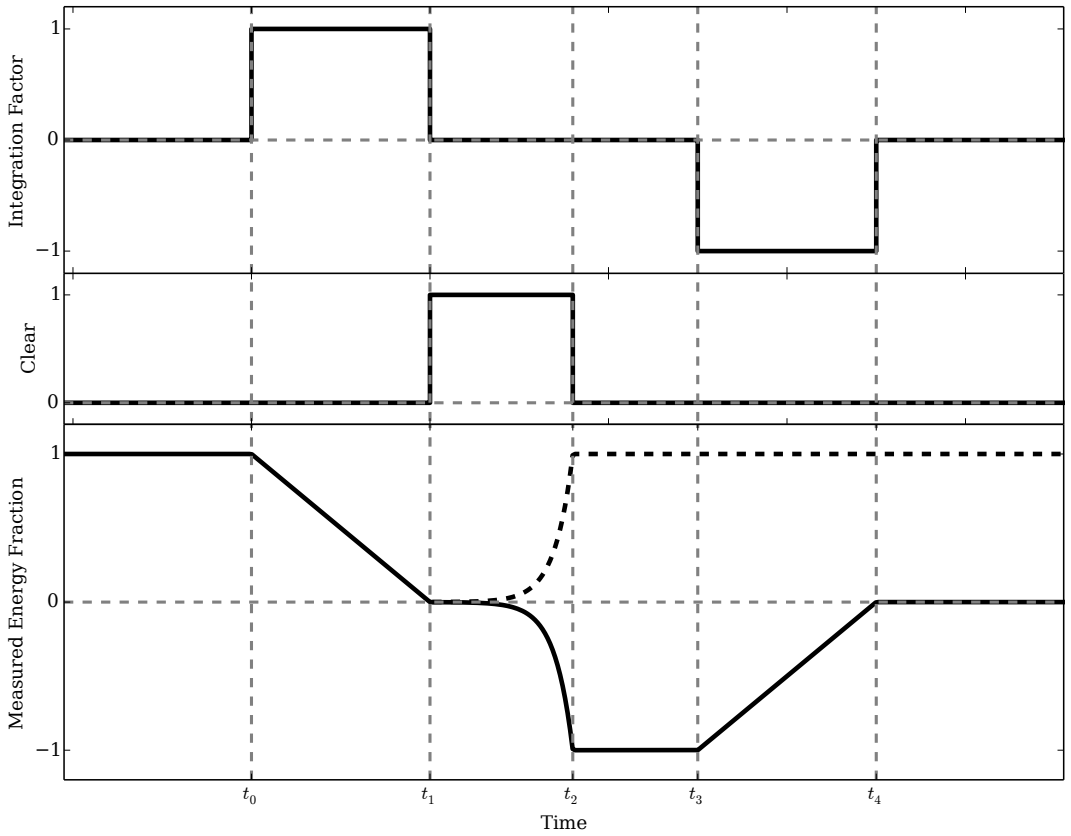

Figure 3.8: Simulated temporal behaviour of a DEPFET during the read-out. In this scheme, the influence of the readout on the measured signal starts at t_0. **Top**: During the time interval $[t_0, t_1]$, the charge present in the pixel is integrated for the first time. Between times t_3 and t_4, a second integration of the same length takes place, but with negative sign. As the panel in the **centre** indicates, the clear is active between these two intervals to remove the charge inside the pixel. If the charge is induced outside the active part of the readout, represented here by the interval $[t_0, t_4]$, these two processes lead to a measurement proportional to the charge. The purpose of the second integration is to measure the baseline signal which is present even if no event happened during the last frame. However, if charge is produced during the read-out process, the measurement may fail. The **bottom** panel describes the fraction of the measured photon energy to the true energy, depending on the arrival time of the photon. If the photon hits the pixel during the first integration period, the integrated charge is smaller than if the charge was present from the beginning, and the measurement result is lower than expected. If charge is produced after the first integration and is not removed completely during the clear process, the baseline measurement will also measure this additional charge, and produces a negative result (solid line). However, it will still be present in the first integration of the next frame, where it produces a standard, positive measurement (dashed line). As the arrival time gets closer towards the end of the clear, the time available is not long enough to remove the charge completely. If the photon arrives during the second integration period, the negative measurement starts to shrink towards zero, for the same reasons as for the first integration.

integration, a settling time is placed. The energy of photons hitting the pixel during this time are measured twice with the correct value, but with alternating signs. This changes during the second integration, when the same effect as during the first integration hap-

Table 3.1: The time dependence of the measured energy E_{m} on the photon impact time t_{photon} as implemented in SIXTE. Only the linear model for the clear is shown in the table. Alternatively, an exponential transition as described by Eq. 3.1 has been implemented.

Arrival Time	Interval	$E_{\mathrm{m,\ current\ frame}}$	$E_{\mathrm{m,\ next\ frame}}$
$t_0 < t_{\mathrm{photon}} \leq t_1$	1st Integration	$+E_{\mathrm{photon}} \cdot (t_1 - t_{\mathrm{photon}})/t_{\mathrm{int}}$	0
$t_1 < t_{\mathrm{photon}} \leq t_2$	Clear	$-E_{\mathrm{photon}} \cdot (t_{\mathrm{photon}} - t_1)/t_{\mathrm{clr}}$	$+E_{\mathrm{photon}} \cdot (t_{\mathrm{photon}} - t_1)/t_{\mathrm{clr}}$
$t_2 < t_{\mathrm{photon}} \leq t_3$	Settling	$-E_{\mathrm{photon}}$	$+E_{\mathrm{photon}}$
$t_3 < t_{\mathrm{photon}} \leq t_4$	2nd Integration	$-E_{\mathrm{photon}} \cdot (t_4 - t_{\mathrm{photon}})/t_{\mathrm{int}}$	$+E_{\mathrm{photon}}$

pens: The integration result drops, as the charge is integrated only partially over t_{int}. Thus, the negative measurement approaches zero as the impact time shifts towards t_4.

As the presence of misfits distorts the spectrum, these effects were implemented into SIXTE in the course of this work. As no measurements of these effects were available yet, simple, linear models were used to describe the dependence of the measured photon energy E_{m} on the arrival time t_{photon}. These models assume a linear drop of the measured signal from the full energy of the photon, E_{photon}, to zero during the first integration and from $-E_{\mathrm{photon}}$ to zero during the second integration. Even the time dependence during the clear was modelled linearly, rising from zero to $\pm E_{\mathrm{photon}}$ between t_1 and t_2. Later, an exponential rise was also implemented:

$$E_{\mathrm{m}} = \pm E_{\mathrm{photon}} \cdot e^{(t_{\mathrm{photon}} - t_2)/\tau}, \quad t_1 < t_{\mathrm{photon}} \leq t_2\,. \tag{3.1}$$

Table 3.1 summarizes the implemented temporal behaviour of DEPFET-sensors. For the current WFI-setup for SIXTE, the following parameters are used: The integration time is set to $t_{\mathrm{int}} = 1\,\mu$s, the clear takes $t_{\mathrm{clr}} = 300\,$ns. The settling time has a length of 100 ns. Tests with the exponential clear model and a time constant of $\tau = 150\,$ns have been performed.

3.3 The Detector Model of the X-IFU

Similar to the WFI, the final layout of the X-IFU is still under development. However, it is clear that the detector will rely on a TES array, probably with hexagonal shape. Studies during the last years have also taken a hybrid array into account, consisting of pixels with different sizes and properties. In the following section, the geometry used for the simulations presented in this work is described. Afterwards, a short introduction to the sensor function is provided to give an understanding about the implementation of the X-IFU in SIXTE is given.

3.3.1 The Sensor Geometry

The X-IFU is represented with different models in SIXTE. The software was extended to cope with complex geometries such as the hexagonal arrays planned for this detector. The

current baseline design was already described in Chapter 2. This so-called LPA2 design consists of 3540 square pixels with a size of 256 μm×256 μm. The pixel pitch in the array is 260 μm, resulting in 4 μm wide gaps between the individual TES which are blind for radiation in the simulations. The detector covers a field of view of approximately 5' on the sky with a focal length of 12 m. The LPA2 as implemented in SIXTE is illustrated in the left panel of Fig. 3.9.

A non-baseline design for the detector is the hybrid array. Such a design makes use of pixels with different sizes to optimise individual regions of the detector area for specific observation purposes. The right panel in Fig. 3.9 shows the same LPA2 as on the left, but with a Small Pixel Array (SPA) placed in the centre, substituting some of the LPA's pixels. The SPA itself consists of smaller pixels with a size of 106 μm×106 μm and a pitch of 110 μm. 19×19 of these pixels form a square array which may improve the high-count rate capability of the detector. In Chapter 4, only this small array is used. For this special case, the results of the study are dominated by the total count rate on the detector and the energy resolution, which is the same for both detector versions. So the selection of the SPA for the WHIM study does not affect the outcome of the simulations.

3.3.2 Principles of TES detectors

Sensors such as the WFI's DEPFET rely on the linear dependence between the photon's initial energy and the number of electron-hole pairs created when the photon interacts

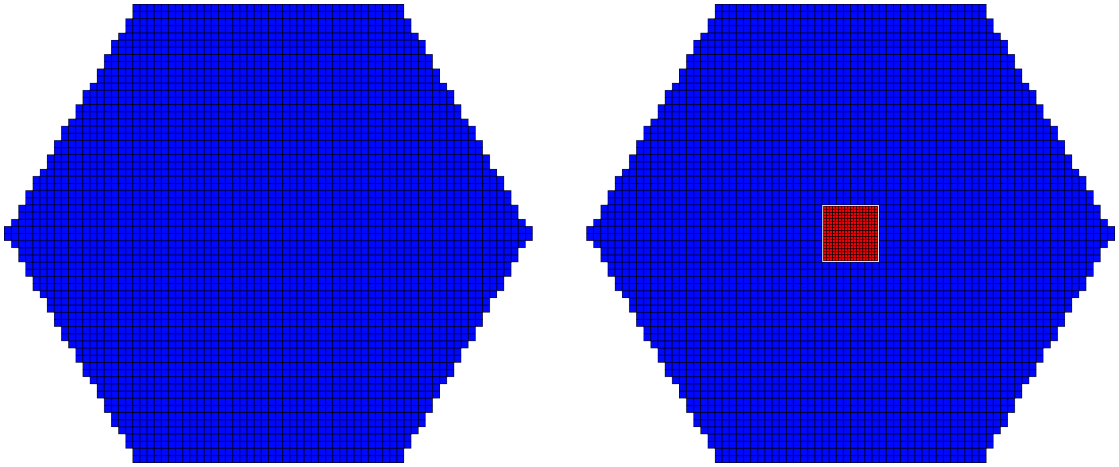

Figure 3.9: Two configurations of the X-IFU implemented in SIXTE. **Left**: The LPA2 design features 3540 pixels combined to a large hexagonal array. Each of the pixels has a quadratic shape with a side length of 256 μm. Between the individual pixels are 4 μm wide gaps, such that the pixel pitch is 260 μm, which equals to a angular resolution of 4.5″. The whole array covers a field of view of approximately 5′. This design is the baseline detector configuration for the X-IFU since 2016 November 22 (Barret, 2016). **Right**: The same design as on the left, but with a SPA embedded in the centre of the hexagon, forming a hybrid array. The SPA consists of 19×19 pixels in a square array, each of which has a size of 106 μm×106 μm and a pitch of 110 μm. This replaces the innermost pixels of the LPA2 array, leading to a total number of 3800 pixels. The SPA provides a higher angular resolution of 1.9″.

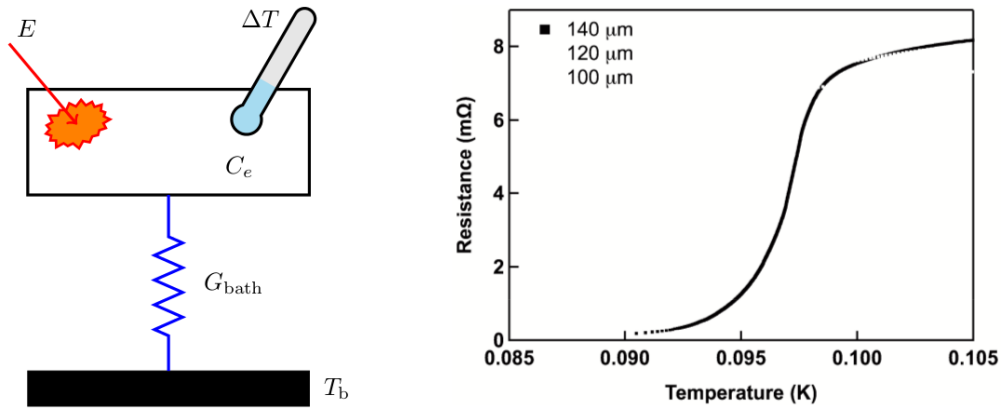

Figure 3.10: The function of a Transition Edge Sensor. On the **left**, the scheme of a TES shows its basic components (image from Wilms et al., 2016). The sensor material with a heat capacity C_e is coupled to a cool bath with a temperature T_b via a thermal link with a conductance G_{bath}, such that its temperature rests in the regime between the superconducting and normal states. If a photon hits the sensor, it is absorbed and its energy E is converted into an increase of temperature ΔT. As can be seen on the **right**, such a temperature increase leads to a very strong change of the TES's resistance. The graph shows an example measurement of a sensor at $T_b = 55$ mK (plot from Smith et al., 2016).

with the material. However, the Fano noise as a result of this stochastic process limits the measurement accuracy (Fano, 1947; Janesick et al., 1988). For example, the WFI will have a resolution of around 150 eV at a photon energy of 6 keV. The existence of Fano noise means that better resolutions, such as the required 2.5 eV for the X-IFU, can only be obtained by using different methods to determine the photon's energy. One other possibility is used in a Transition Edge Sensor: Instead of the number of charge carriers produced by the interaction, the rise of the temperature of the absorber is measured. The change due to a single X-ray photon is small, so a very elaborate measurement chain is required.

The TES solves this problem by cooling the sensor material down to a temperature which lies just at the transition between the superconducting state and the normal state, which causes a strong increase of the material's resistance for small changes in temperature. As is illustrated in Fig. 3.10, a photon interacting with the sensor material causes a slight increase in the absorber's temperature. Due to the steep rise of the material's resistance at the transition edge, the temperature increase can be measured as a strong change in the sensor's conductance. With an appropriate read-out, the X-IFU's sensors will reach an energy resolution of 2.5 eV and below (Barret et al., 2016).

However, because of the strong non-linearity between the observable resistance and the photon's energy, the processing of the measured resistance curves over time is also more complicated than for a DEPFET. Due to the thermal link of the absorber material and the cooling bath, an increase of the sensor's temperature due to a photon is neutralised over time; the stronger the thermal link, the faster the baseline temperature will be reached again. This leads to a peak-like shape of the measured resistance over time, as seen in Fig. 3.11. The Event Processor of the instrument needs to extract the photon energy from

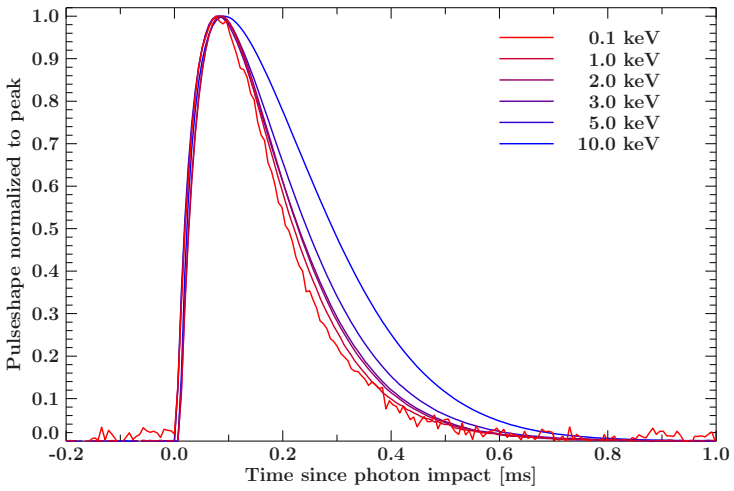

Figure 3.11: Example TES pulses simulated with `tessim`. The measured sensor response normalised to the area of the pulse, is plotted over the time since the photon impact for different energies. A strong increase in temperature due to the energy injected by the photon is followed by a slower decrease caused by the thermal link of the absorber to the cooling bath. The pulse shape is dependent on the photon's energy. Figure from Wilms et al. (2016).

such a data stream. Different pulse reconstruction algorithms are investigated for their qualities, as presented by Peille et al. (2016).

One outcome of this study is the dependence of the real energy resolution on the time between two individual pulses. The final energy resolution of the instrument is not only limited by the theoretical limits of the measurement of the temperature but also degrades due to uncertainties in the energy reconstruction step. Peille et al. (2016) found that two effects play a role for this additional degradation: When two pulses are very close together such that they overlap, the first pulse adds an energy bias to the measurement of the second pulse. Additionally, the number of data points available for the reconstruction of the pulses is more and more limited, the shorter the time between them is. Both of these effects lead to a degradation of the instrument's effective energy resolution at high count rates.

3.3.3 The implementation of TES detectors in SIXTE

The previous section indicated that TES detectors are fundamentally different in their function and behaviour than CCD or DEPFET sensors, for which SIXTE has been developed primarily. However, the modular design of the software made it possible to perform realistic simulations for TES detectors by only switching to another photon detection algorithm. Such a module has been developed by Wilms et al. (2016) under the name `tessim`. This software solves the time-dependent differential equations for the TES's temperature and current to numerically simulate the individual pulses caused by incoming photons. The output of `tessim` can be analysed like real measurements, for example with SIRENA, the software which will later be used for the on board processing (Ceballos et al., 2015).

However, this approach is unsuited for the simulation of observations with long exposures due to the high amount of calculation time needed. For such simulations, an alternative detection step has been implemented for TES detectors in SIXTE under the lead of Philippe Peille. This algorithm tries to extend the simplicity and high performance of

Table 3.2: TES grade definitions for the LPA2 and the SPA for a sampling frequency of 156.25 kHz.

	N_{samples}(prev.)	N_{samples}(next)	Energy Resolution (<7 keV)
LPA2			
High	800	16384	2.5 eV
Mid	800	512	3.0 eV
Low	800	1	15.0 eV
SPA			
High	128	512	2.5 eV
Mid	128	128	3.0 eV
Low	128	0	15.0 eV

the use of an RMF to randomise a photon's energy according to the detector's resolution and the knowledge gained from highly accurate simulations with `tessim` and energy reconstruction algorithms. Instead of using one RMF for all events, a set of three response matrices is used. As the observed energy resolution depends on the time between two photon impacts, the events are classified in three grades; high-, mid- and low-resolution events. The grade of an event depends on the time differences to previous event and to the next impact. The grade definitions for the current implementation of the SPA and LPA2 are listed in Table 3.2. With this setup, the count rate dependent degradation of the X-IFU's energy resolution can be taken into account realistically without sacrificing computing performance.

Another effect expected for the X-IFU is crosstalk. Crosstalk means the influence of the measurements of different pixels on each other. In the case of the X-IFU, this effect will be caused by different mechanisms such as thermal and carrier leakage, non linearities in the amplification and the common impedance (den Hartog et al., 2016). Crosstalk will lead to a slight degradation of the energy resolution. Descriptions of the relevant mechanisms are currently under development in SIXTE but have not been used for the simulations as presented in this work. Instead, the energy resolution of 2.5 eV for high-resolution events already includes the effect of crosstalk.

4 Detection of WHIM filaments with the X-IFU

As discussed in Chapt. 3, one purpose of detector simulations is testing the capability of an instrument to fulfill its goals during the design process. This allows the scientists to check whether the mission as planned is sufficient to collect the data needed to answer certain questions. One example of such simulations which have been undertaken for the *Athena* X-IFU instrument is about the search for missing baryons in the WHIM by observing faint absorption lines in the spectra of GRBs, one of the science goals of the mission (Nandra et al., 2013) as described in Sect. 1.2. The WHIM-study was performed using SIXTE (Wilms et al., 2014). The results presented in the following pages are based on the technical report describing the simulations by Brand et al. (2016b) and the publication by Brand et al. (2016). First, the simulation setup is described, followed by an explanation of the analysis of the simulated event data. Finally, the results give an impression on the capability of the instrument. Note that in part, the text of this chapter is taken in verbatim from these publications.

4.1 Simulation of WHIM filaments in SIXTE

The part of the science goal to be examined with the simulations described in this section requires to find WHIM-filaments in the spectra of GRB afterglows (Nandra et al., 2014). This means that all of the light detected by *Athena* has its origin in the GRB and only featuring variations in the absorption caused by the intergalactic matter. To be able to simulate a representative set of afterglows, existing data from similar events can be studied.

One of the properties of a GRB afterglow is its declining brightness over time. To investigate this, all 948 Swift XRT-light curves in the 0.3-10 keV energy band[1] (Evans et al.,

[1] `http://www.swift.ac.uk/xrt_curves/`

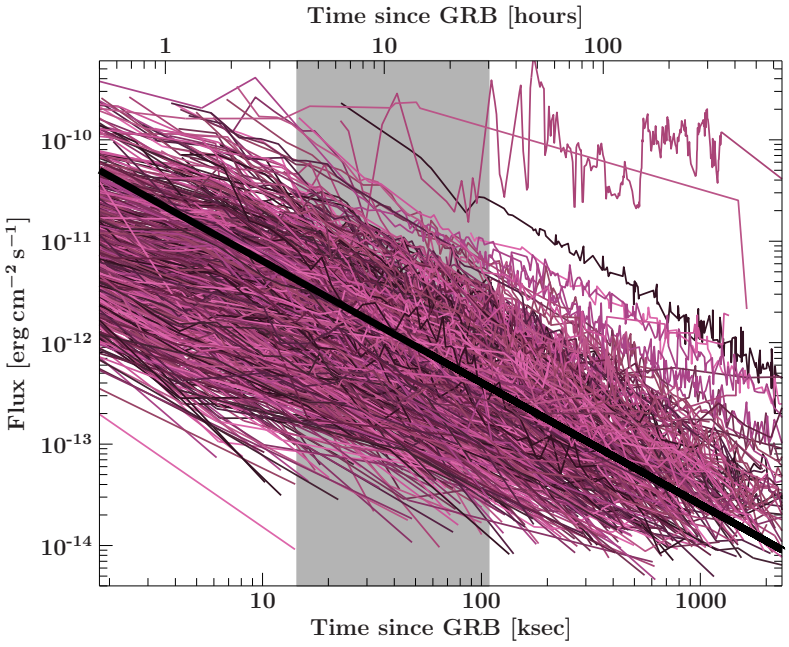

Figure 4.1: All 948 Swift GRB afterglow light curves (purple lines) analysed for the simulations presented in this work. The data has been measured between 2004 December 18 and 2015 September 31. The time behaviour of the GRBs in the relevant regime between four to 30 hours after the initial outburst (shaded in gray) can be approximated by the relation $F \propto t^{-1.2}$ (black line). This dependency is assumed for the input to the simulations. Figure modified after Brand et al. (2016).

2007, 2009) measured between 2004 December 18 and 2015 September 31 are investigated. The light curves are shown in Fig. 4.1. Following Margutti et al. (2013), a powerlaw relation of

$$F \propto t^{\alpha} \tag{4.1}$$

between the flux F and the time t with a powerlaw index α is fitted to the individual afterglows. In agreement with Margutti et al. (2013), a dependency of $t^{-1.2}$ is found to well represent the light curves in the relevant time range between four hours to 30 hours after the initial outburst.

The Swift data are also used to define the flux regime for the simulations. Figure 4.2 depicts the cumulated number of outbursts for a given flux or the respective number of counts, translated using the nominal effective area for a mirror radius of 1469 mm. The three curves reflect the flux measured at different times after the initial outbursts. They show that the highest fluxes to be expected are on the order of 10^{-10} erg cm^{-2} s^{-1}. Afterglows with this brightness are found around once per two years in the XRT-data. The Burst Alert Telescope (BAT) on Swift, which is used to trigger the XRT-observations, covers a field of view of 1.4 sr or around 1/9 of the full sky (Barthelmy et al., 2005), which means that the rate of these bright outbursts is on the order of five per year on the full sky. At brightnesses 100 times fainter, around 50 afterglows are observed per year with the XRT. This flux of 10^{-12} erg cm^{-2} s^{-1} is used as the lower limit which is accounted for in the simulations.

The spectrum of the GRB afterglow is modelled as an absorbed powerlaw with a photon index of $\Gamma = 2$ (Branchini et al., 2009) and a hydrogen equivalent absorption column of 1×10^{22} cm^{-2}. This value is simulated slightly higher than the median of 6×10^{21} cm^{-2}

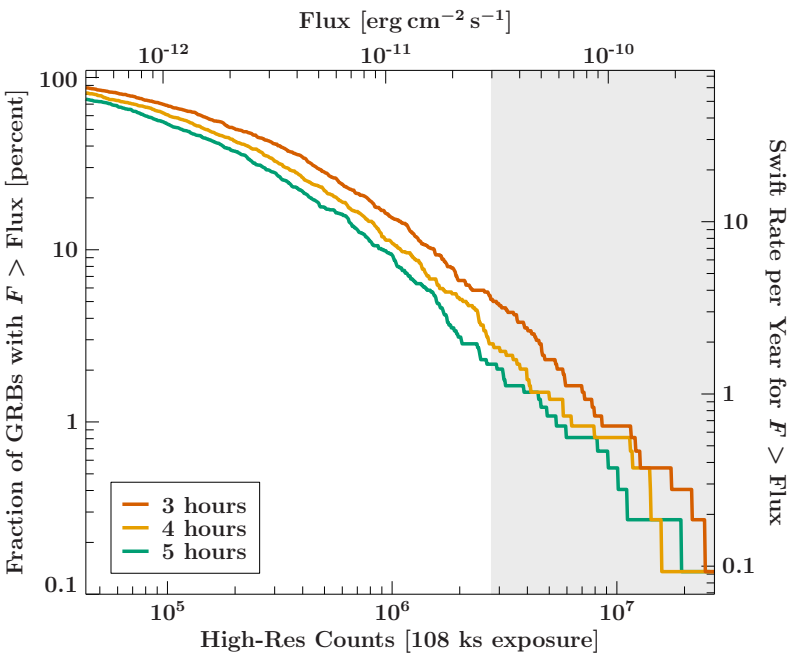

Figure 4.2: The cumulative number of GRB afterglows detected by Swift per year, brighter than the flux given on the upper x-axis. The three curves depict the cumulative distributions for the brightness after 3, 4 and 5 hours of the initial outburst. The equivalent count number after a 108 ks exposure with the X-IFU is presented on the lower x-axis. The shaded region marks the flux regime in which single lines can be reconstructed with a false alarm probability of less than 20% for EWs larger than 0.07 eV. Figure modified after Brand et al. (2016).

Table 4.1: The Spectral parameters for the GRB afterglow and WHIM model as used in the simulations presented in this chapter.

Parameter	Value	Reference
GRB Afterglow		
Photon Index	2.0	Branchini et al. (2009)
Redshift	2.0	Margutti et al. (2013)
Intrinsic Absorption	1×10^{22} cm^{-2}	
WHIM O VII Line at 574 eV		
Redshift	0.0–0.1	
Equivalent Width	0.07–0.28 eV	Branchini et al. (2009); E. Ursino, priv. comm.
σ	0.1 eV	
WHIM O VIII Line at 654 eV	optional	
Equivalent width	2/3 of O VII	
σ	0.1 eV	
Galactic Absorption	2×10^{20} cm^{-2}	

found by Margutti et al. (2013) to conservatively account for the broad range of the parameter. The afterglow is placed at a distance of $z = 2.0$, which shifts the prominent oxygen absorption edge from approximately 530 eV to effectively 180 eV, which is outside of the line search interval as discussed below. This means that the slightly higher intrinsic absorption should not have much effect.

The WHIM is modelled by either one or two faint absorption lines with Gaussian shape. In all cases, the O VII is present in the spectrum. It is located at an energy of 574 eV in the frame of rest of the filaments. The Equivalent Width (EW) of the line is varied from 0.07 eV up to 0.28 eV, following Branchini et al. (2009) and E. Ursino, priv. comm.. An

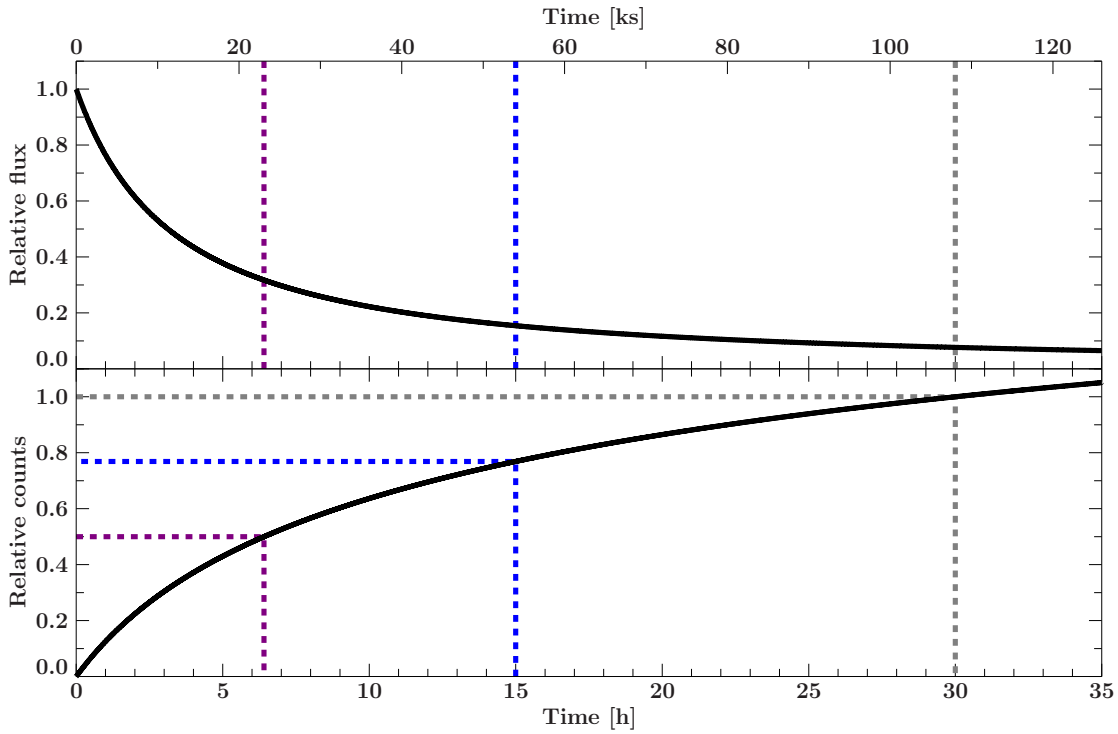

Figure 4.3: A light curve modelled with the dependency of $F \propto t^{-1.2}$ as shown in Fig. 4.1. The **top** panel shows the relative flux as a function of the time, normalised to the start of the observation. The **bottom** panel depicts the cumulated flux up to a certain exposure time, normalised to the X-IFU's maximum exposure time of 108 ks. It can be seen that half of the maximum possible counts for this instrument are collected in the first 22 ks (purple dashed line). After the first half of the 108 ks, around 76% of the photons are detected. Figure after Brand et al. (2016b).

optional second absorption feature, representing the O VIII line at a frame of rest–energy of 654 eV, is modelled with the EW tied to two thirds of the strength of the first line. As both lines have their origin in the same gas filaments, they share the same redshift. The redshift was chosen randomly between $z = 0.0$ and 0.1 in order to simulate the detection of local baryons. The width of the lines is assumed to be considerably lower than the 2.5 eV–energy resolution of the instrument, and is set to $\sigma = 0.1$ eV.

The last component of the spectral model is the Galactic absorption. This represents the absorption due to the interstellar medium of our Galaxy. It is modelled with an absorption column of $N_{\mathrm{H}} = 2 \times 10^{20}\,\mathrm{cm}^{-2}$. The complete list of spectral parameters is summarised in Table 4.1.

The instrument setup of the X-IFU in SIXTE is described in Sect. 3.3. As a large number of long-exposed observations will be simulated, only the RMF-based simulation approach is used, with the event grading described in Table 3.2. For the WHIM-simulations, only the SPA together with the nominal mirror radius of 1469 mm is used. For each of the combinations of spectral parameters and starting flux as described above, 51 simulated observations are performed, with the redshift of the WHIM-filament varying in the given region. Each simulation starts at four hours after the initial outburst, following the ToO

reaction time requirement of the instrument (Barret et al., 2016; Nandra et al., 2014). The exposure time is chosen to be 30 hours (108 ks), which is the maximum possible continuous exposure time with the X-IFU. This means that the resulting detection probabilities show the maximum which can be expected from real observations (Barret et al., 2016; Nandra et al., 2014). However, as Fig. 4.3 shows, most of the counts collected from a GRB-afterglow as simulated here arrive at the start of the observation. During the second half of the exposure time only around 20% of the total events are collected. This result implies that the exact duration of the observation does not have a huge impact on the detection probability.

4.2 Detection of faint absorption lines

The goal of the analysis presented in this chapter is to find out at which probability a WHIM-filament can be detected, assuming a certain line strength and GRB-brightness. To answer this question, the analysis of the simulated event data tries to reproduce the work of an astronomer who does not know the properties of the intergalactic gas, at which distance it is located, and if it is even visible in the line of sight. Furthermore, several thousands of spectra need to be handled to account for all cases and get a reasonable statistical number, so a manual analysis can not be performed. Instead, an automated blind line search as proposed by Protassov et al. (2002) is performed on each spectrum. The basic idea behind this method is to find the redshift value for which the line model and the simulated spectrum match the best, and to estimate the significance of the detection afterwards. In the following, the details about this algorithm are explained. The analysis is performed using ISIS (Houck & Denicola, 2000) and the ISIS functions (`ISISscripts`) provided by ECAP/Remeis observatory and MIT[2].

At first, the simulated observation data are binned to a spectrum with a bin width of 0.8 eV, using only the high-resolution events and a low-energy threshold of 0.25 keV. This approach oversamples the spectral resolution of the X-IFU roughly by a factor of three. The high number of several hundreds of counts per bin allows us to use χ^2-statistics for the subsequent fit. As we aim to handle the simulated data just as real observation events, not only the WHIM-lines need to be found, but the continuum needs to be described as well. The model used for fitting is similar to the one used to generate the event data. It consists of an intrinsically absorbed powerlaw for the GRB and a second absorption component for the Galactic absorption. To make the automated analysis more stable, the GRB's redshift as well as the Galactic absorption column are assumed to be known from other observations. These parameters are fixed during the spectral fitting process, all others are free.

After the first estimation of the continuum, an energy- or redshift range is defined in which the blind line search looks for the absorption features. Initially, the redshift range of the search interval is set to $0.0 \leq z \leq 0.1$, with a later extension to 0.5 to account for the influence of the size of the search interval. For the O VII line, a redshift of 0.1 results

[2] `http://www.sternwarte.uni-erlangen.de/isis/`

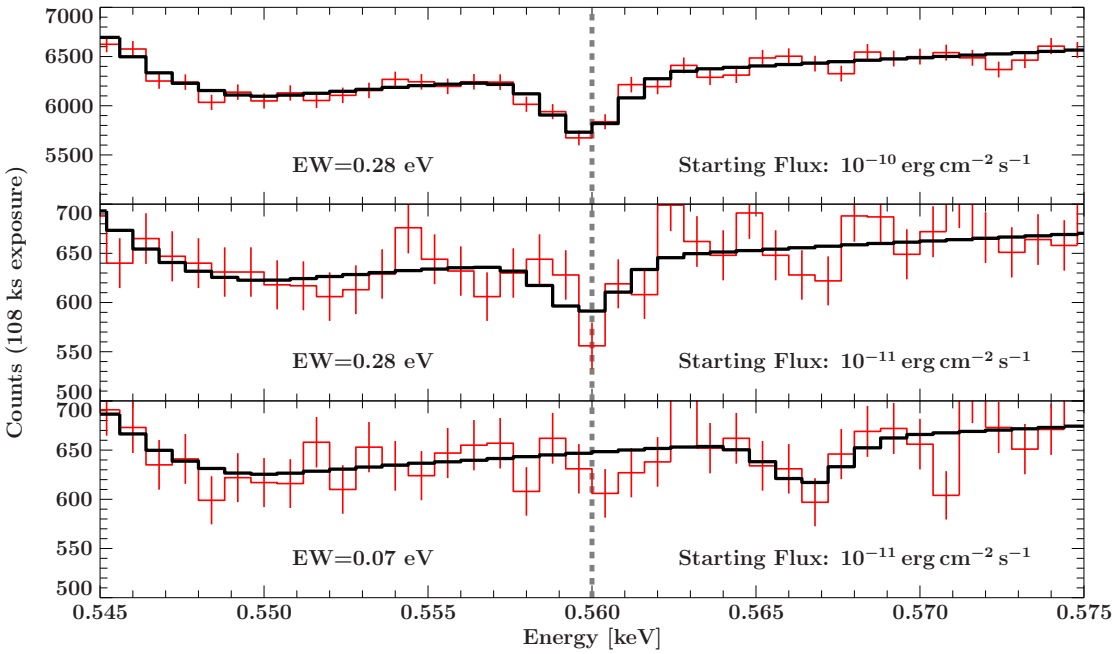

Figure 4.4: Three different simulated GRB afterglow spectra with a WHIM absorption line at 0.56 keV (red curves). The model produced by the automated analysis is represented in black. The **top** panel shows the spectrum for a bright afterglow and a strong line with an EW of 0.28 eV. The line can be identified easily. The panel in the **middle** shows a line of the same strength, but the afterglow is dimmer by one order of magnitude. The noise is higher than before, but the line is still found. The **bottom** panel shows the spectrum of an afterglow with the same brightness, but the line is much weaker with an EW of only 0.07 eV. The blind line search algorithm fails and confuses the true line with a random noise feature. Figure modified from Brand et al. (2016b).

in a measured line position of 0.522 keV. This energy- or redshift range is divided into small segments of $\Delta z = 1.4 \times 10^{-3}$ for the two line model, or an approximately similar $\Delta E = 0.5$ eV for the single line model. In the case of the two-line model, the frame of rest–energies of the lines are fixed to the respective values of the O VII and O VIII lines, such that the positions in the measured spectrum are influenced only by a shared value for the redshift. The redshift of the filament is subsequently fixed to each of these bins, while at each step, a fit of the spectral model to the simulated data is performed. The result is a list of χ^2-values, one for each line shift, which quantify the match between the model and the data. This is used to determine the redshift for which the model matches the best by searching the minimum χ^2-value. Three example best-fit spectra of such blind line searches are shown in Fig. 4.4.

However, this only gives the most likely position of a possible absorption feature. To calculate the significance of this detection, the best-fit model is used to generate 100 realisations of the continuum. Each of these spectra is analysed in two ways: First, it is fitted with the continuum components only. Then it is fed into the same blind line search algorithm as used before. Both fits return their best-fit χ^2-values, which are compared by taking the difference as $\Delta\chi^2 = \chi^2_{\text{continuum only}} - \chi^2_{\text{blind line search}}$. This difference gives

the improvement of the fit statistics caused by the addition of the line components. The original line detection is found to be significant if its own $\Delta\chi^2$-improvement is higher than 90% of the continuum–only values. In contrast, if any random fluctuations caused by noise in the spectra provide a better match to the WHIM-model than the fit in the original spectrum in more than 10% of the cases, the detection is insignificant.

4.3 What *Athena* can see

An intermediate result by the observation simulations of Sect. 4.2 is the number of counts which can be expected from an X-IFU observation with the maximum exposure time of 108 ks, taking into account the source model as described above. Figure 4.5 shows the dependence between the starting flux of the GRB afterglow four hours after the initial outburst and the total number of counts in the 0.3-10 keV energy band. It is separated into the three different event categories, high-, mid- and low-resolution events. In the relevant flux regime, the number of high-resolution events is almost two orders of magnitude higher than the number of mid-resolution counts. This means that no significant amount of data is lost by using only the high-resolution events.

The analysis results of the automated blind line search and significance calculation gives an idea about the outcome of a single WHIM observation - a positive or negative detection of the filament. However, in this study, the aim is to estimate the detection probability of a given line strength, depending on the flux of the GRB, and to quantify the reliability of announced detections. These quantities are described in the following sections.

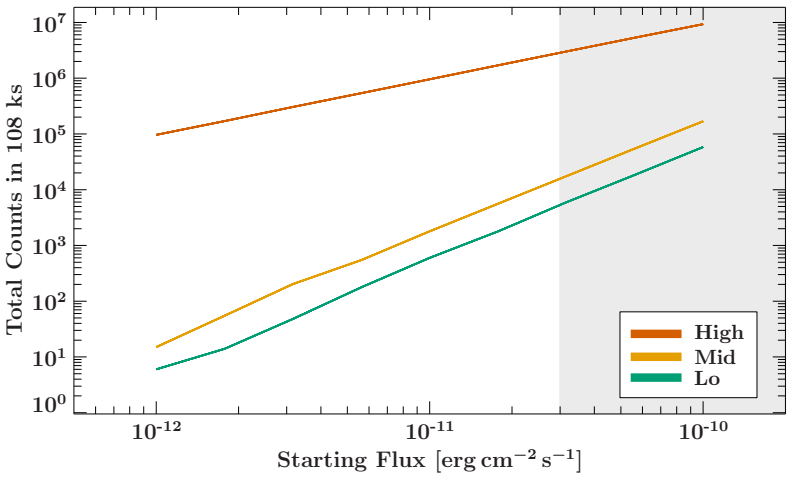

Figure 4.5: The number of counts detected by the X-IFU after an exposure of 108 ks as a function of the starting flux. The three curves depict the number of high-, mid- and low-resoultion counts. In the flux regime described in this work, the curves show no sign of high pile-up, which would cause a larger number of mid- or low-resolution events than high-resolution events. In the analysis, only the high-resolution events are used. Figure modified from Brand et al. (2016b).

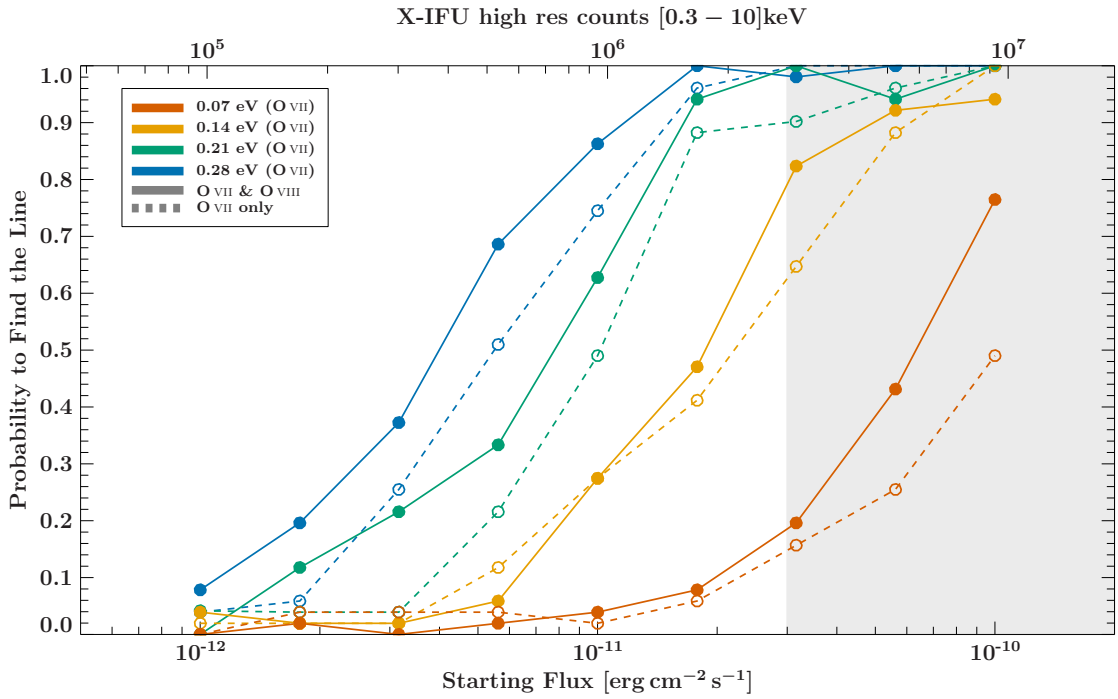

Figure 4.6: Detection probability for weak absorption lines as expected from WHIM-filaments as a function of the starting flux of the GRB afterglow. The different colors depict the probabilities for four EW-values, ranging from 0.07 eV to 0.28 eV. The **solid** lines give the probabilities calculated by using two absorption features, representing the O VII and O VIII lines for the blind line search. The **dashed** lines are the result of the same analysis but using only the strong O VII line. The upper x-axis gives the total number of counts in the 0.3-10 keV energy band for the starting flux at the lower x-axis. The detection probability increases with higher count numbers. As expected, the analysis shows that strong lines are found easier than weak features. The use of two absorption features with known energies in their frame of rest helps to make the analysis more reliable. The search interval for the lines is $0.0 \leq z \leq 0.1$. Figure modified from Brand et al. (2016b).

4.3.1 The dependence of the detection quality on the number of lines

To calculate the detection probability, all simulated observations with the same source flux and line EW, but different redshift values are combined to calculate the line detection probability:

$$P(\text{line found}, F, \text{EW}) = \frac{N(\text{significant detection, position correct}, F, \text{EW})}{N(F, \text{EW})} \,. \tag{4.2}$$

Here, $N(F, \text{EW})$ is the total number of simulated observations with a given Flux and EW, while $N(\text{significant detection, position correct}, F, \text{EW})$ is the number of significant detections which also find the lines at the correct redshift amongst these observations. To define if the redshift is found correctly, both the 90% confidence interval of the respective fit parameter and an additional margin are taken into account. The fixed margin is set to either $\Delta z = 1.0 \times 10^{-3}$ for the two-line case or $\Delta E = 1.25\,\text{eV}$ in the case of a single absorption feature. Figure 4.6 shows the resulting detection probabilities for four

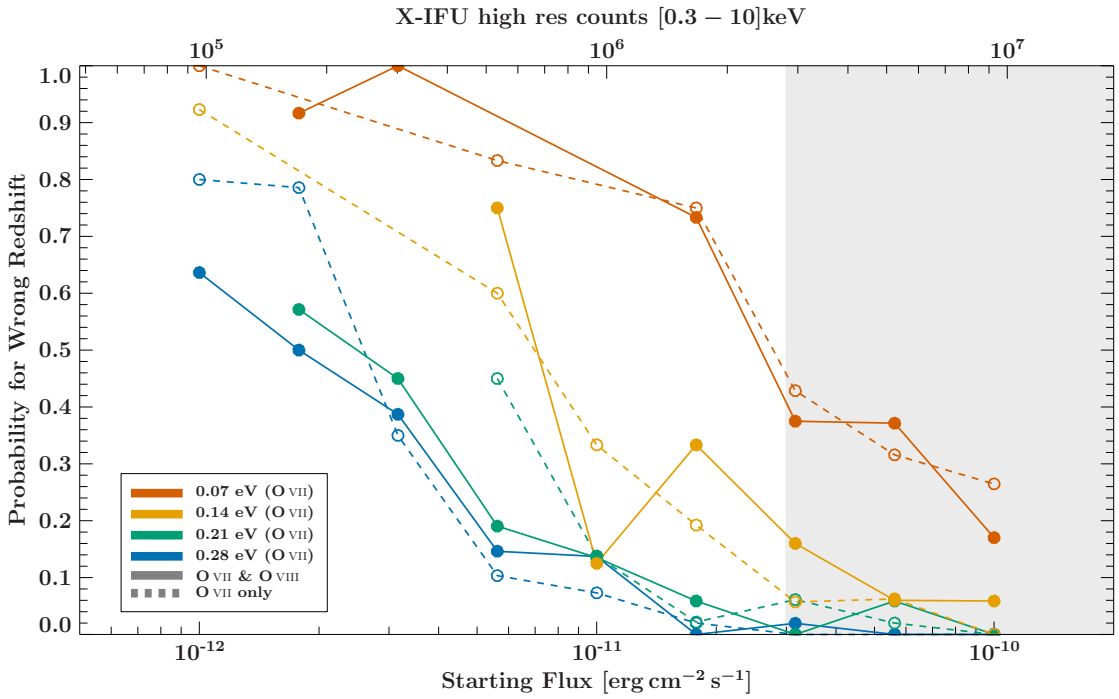

Figure 4.7: False alarm probability for the same simulation setup as shown in Fig. 4.6. The **solid** lines give the probabilities calculated by using two absorption features, representing the O VII and O VIII lines for the blind line search. The **dashed** lines are the result of the same analysis but using only the strong O VII line. The upper x-axis gives the total number of counts in the 0.3–10 keV energy band for the starting flux at the lower x-axis. Again, the search interval for the lines is $0.0 \leq z \leq 0.1$. Figure modified from Brand et al. (2016b)

simulated line strengths over the whole range of the starting flux. Additionally, both the results for the single line and the two line case are given. Overall, the curves demonstrate that with increasing flux, the detection probability increases as expected. The observed flux range covers almost the whole transition between no detections at the lowest starting fluxes of 10^{-12} erg cm^{-2} s^{-1} to a detection rate of almost 100% for the highest starting fluxes of 10^{-10} erg cm^{-2} s^{-1}. It also shows that for low line strengths, it is harder to detect the line, and thus more counts are required to find it. While the detection probability already reaches 100% for the strong lines with a width of 0.28 eV at around 2×10^{-11} erg cm^{-2} s^{-1}, it reaches only around 50% at the brightest GRBs simulated, with a starting flux of 10^{-10} erg cm^{-2} s^{-1}. It is noteworthy that the influence of the use of either one or two absorption lines in the blind line searches improves the detection probability, but only by around 10%-20% at a maximum. The variation of the EW by 0.07 eV has a higher impact on the result in most cases.

Another important quantity which can be extracted from the blind line search results is the false alarm probability,

$$P(\text{false alarm}, F, \text{EW}) = \frac{N(\text{significant detection, position wrong}, F, \text{EW})}{N(\text{significant detection}, F, \text{EW})} \,. \tag{4.3}$$

This number gives the probability that if the analysis finds a significantly detected absorption feature (composed by either one or two lines), it lies outside of the tolerated range around the true value and can be regarded as a wrong result. Such a false detection may cause misinterpretation of the abundance of WHIM in the universe or its spatial distribution and should therefore be avoided.

Figure 4.7 shows the false alarm probability for the same simulation- and analysis data as Fig. 4.6. Overall, the behaviour does not surprise: While at the high starting flux values the number of misdetections is low, it rises for low fluxes. The difference between the individual cases is the contrary behaviour of what has been seen for the detection probability: The higher the EW of the lines, the less false alarms are displayed. For the strongest lines with an EW of 0.28 eV or 0.21 eV, the false alarm probability is almost zero at starting flux values above 10^{-11} erg cm^{-2} s^{-1}. At the same number of counts, the analysed data for the weakest lines of 0.07 eV has a false alarm probability of around 80%. At the lowest simulated starting flux value of 10^{-12} erg cm^{-2} s^{-1}, even the strongest lines have a false alarm probability of around 75%. Due to the small sample size, the difference between the use of one or two lines is not obvious. The small sample is caused by the pre-selection of the cases for which a significant detection is announced by the automated analysis. In the regime where a line can barely be detected, the probability of a significant detection should also drop, regardless if it is right or wrong. In Fig. 4.7, only points with a minimum number of ten samples are shown.

4.3.2 The dependence of the detection quality on the search range

The results discussed until now are gained by a blind line search constrained to a very small interval in redshift of only $0.0 \leq z \leq 0.1$. In reality, this artificially small search region may not be sufficient as, in principle, filaments can imprint absorption lines up to the redshift of the GRB in the background. Cen & Ostriker (2006) show that they expect the WHIM to have a share of around 20% of the total baryonic mass at a redshift of $z = 2$, where the GRB is located in the simulations presented in this work. However, due to the decrease of the effective area of the instrument towards low energies and the intrinsic absorption of the GRB spectrum, the signal to noise ratio drops for highly redshifted lines. At the same time, the number of resolution elements in which the lines are searched increases, which leads to an increase in false detections. Additionally, the position of the O VII drops below the low-energy threshold as set in this analysis, reaching an observed energy of 0.19 keV at $z = 2$. As a compromise to estimate the influence of the extend of the search region, the redshift interval is enlarged up to $z = 0.5$. The measured line energy of the O VII and thus the smallest energy taken into account for the possible central energy of the feature is at 0.383. It has to be noted that this extended analysis is applied to the same data as the first run, so the simulated WHIM-filaments are still between $0.0 \leq z \leq 0.1$.

Figure 4.8 shows the detection probability for this extended search interval compared to the data gained from the initial, small search range. All other parameters are the same as before, and only the two-line search is performed. It can be seen that the increase of the energy range in which the line is looked for makes it harder to detect the features

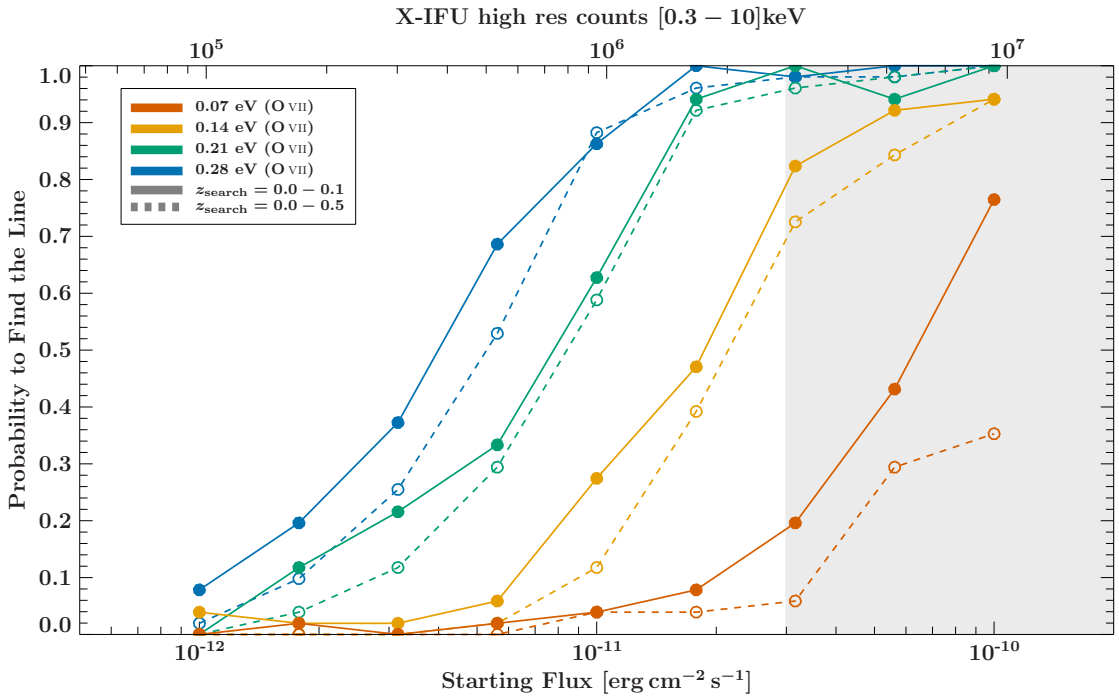

Figure 4.8: Detection probability as in Fig. 4.6, but with the nominal redshift interval for the blind line search of $0.0 \leq z \leq 0.1$ depicted by the **solid** lines, and the extended search range of $0.0 \leq z \leq 0.5$ depicted by the **dashed** lines. In all cases, both the O VII and O VIII lines are used for the analysis. The extended line search is applied to the same simulated event data as before. Figure modified from Brand et al. (2016b)

correctly. The difference in the detection probability between the small and large search interval is comparable to the influence of the use of a single line versus a line pair, as demonstrated in Fig. 4.6. The increased search range also affects the false alarm probability, as Fig. 4.9 shows. Especially for the faint absorption lines, the probability for a wrong detection increases. This can be explained by the higher number of bins, which are randomly affected by noise. The more bins are included in the search interval, the higher is the probability that at one point, the random pattern in the noise is similar to the shape of an absorption feature, which can be confused with a real line. An example of such a case is seen in the lowest panel of Fig. 4.4.

4.3.3 Discussion of the analysis results

In the previous sections, the complicated science case on the detection of absorption lines from WHIM-filaments in the spectra of GRBs has been analysed using a simple spectral model and hundreds of SIXTE-simulations. The general outcome of this study is that the X-IFU as simulated is able to detect WHIM-like absorption features in bright GRB afterglow observations.

The different cases presented in Sect. 4.3.1 and 4.3.2 show that both the exact line pattern

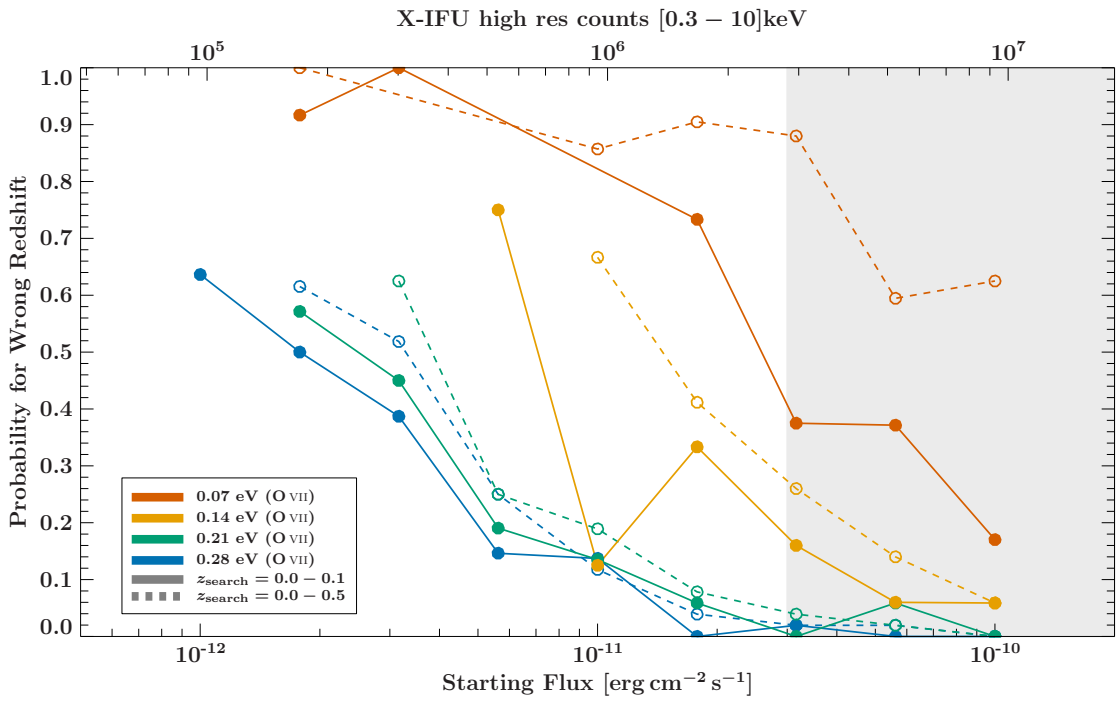

Figure 4.9: False alarm probability as in Fig. 4.7, but with the nominal redshift interval for the blind line search of $0.0 \leq z \leq 0.1$ depicted by the **solid** lines, and the extended search range of $0.0 \leq z \leq 0.5$ depicted by the **dashed** lines. In all cases, both the O VII and O VIII lines are used for the analysis. Figure modified from Brand et al. (2016b)

as well as the finer details of the analysis play a vital role in the true success and credibility of the search results. In Sect. 4.3.1, the difference between the use of one or two lines for the blind line search is described. It shows that by using more than one absorption line, the detection probability improves due to the larger total imprint of the intergalactic matter into the spectrum. The knowledge about the line energies in the frame of rest of the filaments allows us to look for a distinct line pattern in the spectrum, which can be found more reliably than a single line. While the simulations presented here use either only one or two absorption features depicting the O VII and O VIII lines, real filaments may produce even more lines. Branchini et al. (2009) simulates ten WHIM ions. However, the O VII and O VIII lines have been chosen here because they are predicted to be the strongest features in the relevant energy range. Assuming that this is the case, the addition of other lines in the spectrum are expected to be of less impact to the scientific outcome than the addition of the O VIII line as presented above.

In Sect. 4.3.2 the impact of the search range on the detection probability has been discussed. The search range as used in this work is an artificial constraint to the analysis. In general, absorbers can be located anywhere between the source and the observer, thus the natural limit for the redshift range is the redshift of the GRB, in our case. However, some other factors influence the range in which lines can be looked for efficiently. Such factors can be the energy dependent signal to noise, the spectral shape of the background

source, or the limits of the detector. In the case of the simulations as presented here, also the computing runtime has to be taken into account. For several hundreds of spectra, a factor of ten in the extent of the search range means that approximately the same factor needs to be reserved for the computations. The initial compromise of the search range has been chosen to be limited up to $z = 0.1$, with a later extension to 0.5. The results show that the increased search range makes it harder to detect the lines correctly, in both the detection probability and the false alarm probability.

To summarise all of these results, a limit of $3 \times 10^{-11}\,\mathrm{erg\,cm^{-2}\,s^{-1}}$ as the starting flux of the GRB outburst at the beginning of the observation is chosen. This assumes that the X-IFU is able to observe the afterglow for the full 108 ks. At this flux limit, all but the faintest absorbers with a strength of more than 0.07 eV can be detected successfully with a probability of at least 75%. At the same time, the false alarm probability for these parameter combinations is below 25%. At lower fluxes, the line strength necessary to keep the false alarm probability low and the detection probability high increases rapidly. Above, nearly all filaments can be found reliably without significant contamination from false detections. In all of the above plots, the region above this flux value is shaded in grey. As seen in Fig. 4.2, Swift found a rate of approximately two afterglows per year with a starting flux higher than $3 \times 10^{-11}\,\mathrm{erg\,cm^{-2}\,s^{-1}}$ after four hours of the initial outburst with a sky coverage of 1/9 (Barthelmy et al., 2005). Extrapolated onto the whole sky, we can expect around 18 afterglows per year which allow us to reliably detect WHIM absorption lines stronger than 0.07 eV.

5 Optimisation studies for the WFI

In the previous chapters, the *Athena* mission with its two instruments was described as it is planned today. However, the mission is still in the development phase and a lot of details may change until it is finally launched. One of the purposes of the simulations presented in this thesis are to describe the capabilities of the mission design as-is, and to compare it to new ideas and developments. The information gained from these simulations can be used to find the solution which is suited the best for a certain set of scientific requirements. The following sections are a summary of technical reports conducted for the WFI and present two cases which deal with such situations. One of the basic problems of each X-ray detector is pile-up, which limits the capability of the detector to observe bright sources. After a discussion of the meaning of this effect, the bright-source performance of different versions of the WFI are examined. The basic result of this study has been that the best performance can be gained by using a small, fast detector mounted in a position out of the focal plane. In the last section of this chapter, the dependence of the bright source performance of this small chip is described in terms of the out-of-focus position, which can be used for the final design of the detector.

5.1 Pile-up: Blinding the Detector

In X-ray astronomy most sources are so faint that only a few photons can be detected in a relatively long exposure time in the order of seconds to even hours with the current mirror areas. This allows us to use the spatial distribution of events on the sensor not only for a brightness map as of, for example, CCDs in the optical regime, but also to measure the energy of each photon individually. When a high-energy photon interacts with the silicon of the detector, it creates a cascade of electron-hole pairs. The cascade comes to an end when the energy of the individual particles is not sufficient to lift a further electron from the valence band to the conduction band. Even if a part of the primary photon's energy is also converted into phonons, the statistical process results in

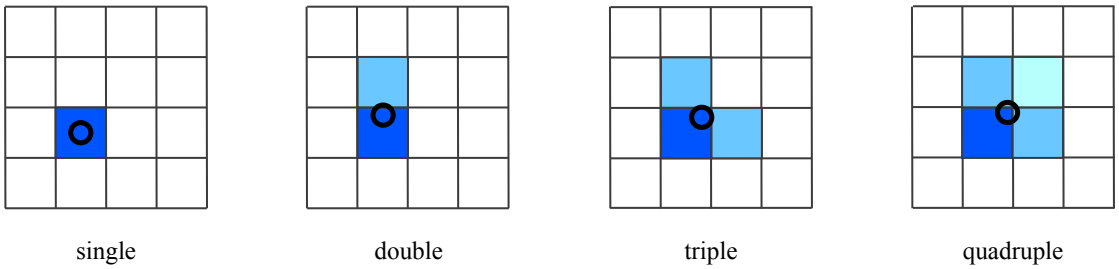

Figure 5.1: The four allowed pattern types in SIXTE. Depending on the impact point of the photon (**black circle**), the created charge cloud may overlap with one, two or three pixel borders, creating a signal in all of the affected pixels. This assumes that the charge cloud is considerably smaller than the pixel pitch. The pixel in which the photon impacts has the highest measured signal. In the case of a triple event, this must be the central pixel of the pattern. In the case of a quadruple event, the pixel with the strongest signal must be at the opposite side of the pixel with the weakest signal. Different patterns must origin from more than one photon events and have to be neglected.

a number of electron-hole pairs proportional to the photon energy. If it is possible to measure the number of electrons collected for example in the internal gate of a DEPFET, it is possible to derive the energy of the X-ray photon.

However, this is only true under two assumptions: Firstly, it requires that all of the charge carriers are measured and are located in a single pixel. Secondly, one has to assume that this pixel has only been hit by one photon during the exposure time. The first of these requirements can be relaxed partially by a more sophisticated analysis. If a photon hits the detector near the border between two pixels, the finite extent of the charge cloud can end up with the total amount of electrons being split over several pixels. Usual detector designs result in charge clouds smaller than the pixel pitch, such that it is impossible that a single charge cloud extends over more than two pixels in a straight line. This leaves us with three different possible pattern types, which are illustrated in Fig. 5.1.

The standard single event is produced if the whole charge is located in one pixel, carrying the full signal. If the photon hits the border between two pixels, both of them will measure a part of the charge, with the main portion in the pixel of the primary impact. This is called a double event. As the impact point gets closer to the corner of a pixel, either a triple or a quadruple event can be generated. This depends on the portion of the charge which is measured in the pixel diagonal to the pixel of the photon impact. If it is small, it may be cut off by the low energy threshold, which is required to suppress thermal noise. Then, a triple event is measured, with the main signal being found in the pixel in the middle. If a quadruple event is produced, the pixels with the maximum and minimum charge are located at the opposite sides. The software which analyses the raw data has to take these split events into account. It has to scan through the signal distribution of each frame, looking for these pattern types. The sum of the individual signals in each pattern is a good estimate for the primary photon's energy. The location of the events can then be estimated by placing them inside the area of the pixel with the highest signal of each found pattern. The use of the signal fractions found in each pixel can further improve the resolution down to sub-pixel estimates, as shown by Dennerl

et al. (2012).

However, bright sources are a problem for this detection concept. When the flux is high enough, such that several photons are spread only over a few pixels during one frame, they produce events in adjacent pixels which are not due to the split of the charge cloud as described above. They can create different kinds of patterns than the four allowed ones. In this case, it is impossible to disentangle the fractions of the total signals cased by each of the photons. As it is better to lose a bit of the sensitivity than to accept spectral degradation in these cases, patterns which are not similar to the four described above are rejected for further analysis. To describe the fraction of the accepted events which can be used for scientific analysis, the term throughput is introduced. It is defined by the fraction of the accepted, valid events, N_{valid}, to the total number of photons which hit the detector plane, N_{tot},

$$\text{Throughput} = \frac{N_{\text{valid}}}{N_{\text{tot}}} \,. \tag{5.1}$$

Because of pile-up, this number is expected to decrease at high source fluxes. There are two types of pile-up: energy pile-up denotes the impact of multiple photons in a single pixel during one frame. This leads to a measured event energy equivalent to the sum of the individual photons. Pattern pile-up means the generation of a valid pattern as shown in Fig. 5.1 by more than one photons. This effect also leads to measured event energies closely related to the original photons. The pattern analysis removes a large number of the corrupted events. However, it can not distinguish if a certain event suffers from energy or pattern pile-up or is indeed an uncorrupted measurement. This leaves a fraction of events which are still measured with the wrong energy. Pile-up can be expressed by the pile-up fraction

$$\text{Pile-up Fraction} = \frac{N_{\text{piled-up valids}}}{N_{\text{valid}}} \,, \tag{5.2}$$

with the number of valid events suffering from pile-up, $N_{\text{piled-up valids}}$. As noted for the throughput, this number increases as the photon density on the detector surface gets higher.

In SIXTE, pile-up is simulated very closely to the real-world process. Each photon generates a Gaussian charge cloud, which is split over several pixels, depending on its impact position. As the detection simulation uses a detailed description of the read-out process, two impacts, for example in neighbouring pixels, will result in a piled-up event just like it would be created in a real detector. However, SIXTE allows the user to track which photons caused which events, even in the case of pile-up. This enables us to study, for example, the pile-up fraction as defined by Eq. 5.2, or the throughput as described by Eq. 5.1. The knowledge gained from such simulations can give us an understanding about which detector designs work better in certain situations, and lets us examine the origins of misbehaviour.

In the special case of the WFI's DEPFET-detectors and the operation in the rolling-shutter mode (see Sect. 2.3.1), pile-up is even more complicated. Until now, it has been assumed

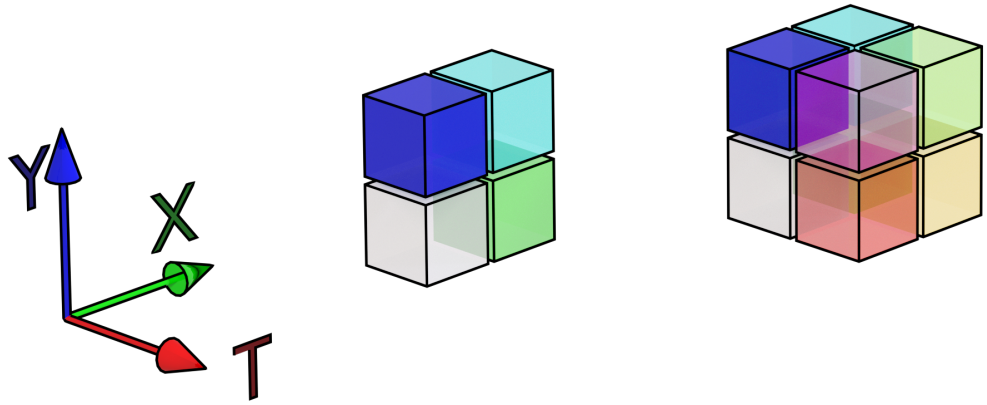

Figure 5.2: An illustration of the effect of the extension from a two-dimensional pattern recombination in only X- and Y-coordinates to a intra-frame pattern recombination algorithm. In the standard implementation, split events are only searched for in the pixel values in one frame. This also implies that a second event happening in the pixels around the primary event either distorts the split pattern to an invalid one, or causes a piled-up valid event which is measured to the sum of both photon's energies. If the split patterns are searched for also in consecutive frames, the geometrical area on the sensor which can be affected by these forms of pile-up is extended to a larger volume in several frames. This means that for such a pattern recombination algorithm, pile-up will cause a bigger problem than for the standard case.

that pile-up happens if two photons hit the detector at adjacent pixels during one frame. However, with the special read-out of the sensors, a split pattern, for example a double-event, can be distributed over two frames if it is created during the read-out of one of the affected rows. In this case, there are two options: The pattern recognition could be extended such that it looks for valid patterns not only in the individual frames, but also for consecutive frames. In principle, this extends the two-dimensional problem in the X, Y-plane to a three dimensional one, with the frame number or time being the new direction, as indicated in Fig. 5.2. This would mean that the so-called intra-frame split events could be recognised properly and treated like a normal split event. The second option is not to look for such events at all and to detect both parts of such an intra-frame split event as individual events.

Both options have advantages and disadvantages. Of course, not taking intra-splits into account means that the spectrum degrades by a certain amount, as the full signal of a single photon is distributed over two parts with lower signals. On the other hand, the search for patterns in consecutive frames complicates the matter of pile-up even more: While pile-up was able to affect an event only during one frame for the case of no intra-frame splits, it can cause problems during three frames if patterns are recombined over adjacent frames, namely the frame of the primary photon's impact, as well as the one before and after. Respectively, the amount of pile-up which is expected with such an algorithm is higher by a factor of around two to three, depending on the exact implementation.

As the goal of the studies presented in the next sections is to examine the best possible

Table 5.1: The simulated X-ray point sources have a Crab-like spectrum, consisting of an absorbed powerlaw with the listed parameters and the abundances of Wilms et al. (2000). With the norm given in this table, the source has a brightness of 1 Crab.

Parameter	Value	Units
Γ	2.1	
norm	9.5	photons $\mathrm{keV}^{-1}\,\mathrm{cm}^{-2}\,\mathrm{s}^{-1}$ at 1 keV
N_{H}	$0.4 \cdot 10^{22}$	cm^{-2}

behaviour of bright sources where pile-up is a large problem, intra-frame split events have not been recombined. It has to be noted that the effect of the not-recombined intra-frame split signals on the measured energy spectrum is only depending on the primary photon's energy as well as the size of the charge cloud. This size determines the fractions in which the full signal is distributed over several pixels. This information can be used to calibrate the data, effectively broadening the detector's response a bit. However, the effect is not dependent on the count rate of the observed source, so this calibration is stable for all sources.

5.2 The Bright Source Performance

In real observations, a variety of source-intrinsic properties such as its brightness or time variability can influence the data quality. During the development phase of the *Athena* mission, we attempt to break down these complex behaviours into simple models. They help us to gain an understanding how individual properties influence the outcome of an observation, and to see whether a particular design option improves the capability of the instrument to collect the data needed for scientific analysis.

The bright source performance studies are one of the cases in which a larger number of designs for the mirror system and the detectors are analysed to evaluate the scientific impact of design decisions. In this study, a test source with a given brightness and a simple spectrum is used to describe the throughput and pile-up fractions of the different instrument setups. Simulations with SIXTE are performed, observing the source with each combination of the optics and detectors. The resulting event lists are used to investigate the throughput and pile-up values for this source brightness. To get an overview how an increase in brightness affects the data quality, these simulations are repeated for different source brightness values. The results of this investigation are documented in technical reports, which can be used by the instrument consortia to make decisions on the development process. The data presented in this section gives an overview on the information as presented in the latest iteration of this report for the WFI.

5.2.1 The Bright Source Simulation Setup

The source chosen as a reference is a point-source with a Crab-like energy spectrum, consisting of an absorbed powerlaw with the parameters as given in Table 5.1. For the

absorption abundances, the values from Wilms et al. (2000) are used. The norm of this standardised spectrum is chosen to result in a brightness of 1 Crab. The flux of this source is varied between 10^{-4} Crab up to 3 Crab, such that the throughput and pileup behaviour can be investigated in a flux range of over four magnitudes, from intermediately bright up to very bright sources.

The optics of the *Athena* mission for these simulations depict the two options described in Sect. 2.2: The nominal mirror assembly has a radius of 1469 mm. The smaller CDF version, discarding some of the outer mirror modules, has also been examined. This mirror version has a radius of 1190 mm. The energy dependent mirror area information is provided by Richard Willingale. Together with the detector's quantum efficiency and the filter transmissivity, these data form the effective area of the instrument. The quantum efficiency and the filter transmissivity curves are provided by Arne Rau. It assumes the use of the external filter in the filter wheel, as discussed in Sect. 2.3.1. Additionally, the resulting effective area is multiplied with a factor of 0.9, which accounts for the influence of manufacturing errors. The mirror area curves and the respective effective areas are shown in Fig. 5.3.

The pointing of the satellite is assumed to be perfectly aligned with the position of the point source. This means that the image resulting from the observations is as sharp as it can be. The PSF describing the position dependent photon distribution is therefore the narrow on-axis function. In the simulations as presented here, it is modelled by a two-dimensional Gaussian model, also dependent on the photon's energy. It has a HEW of 4.9 arcsec at an energy of 1 keV and 5.2 arcsec at 6.0 keV. These numbers have been determined by ray-tracing simulations performed by Richard Willingale. He has also provided a PSF-profile as it would look at a plane parallel to the focal plane, but shifted 15 mm towards the mirror. The resulting out-of-focus PSF is broader and distributes the photons over a larger area on the detector. This model is also used in the following simulations. It is discussed in more detail in the next section.

The detectors themselves are simulated as described in Sect. 3.2. However, due to the narrow size of the source, the sensors can be read-out in window modes. With the on-axis PSF, a window of 16 rows is sufficient to read out all detected photons. This is used

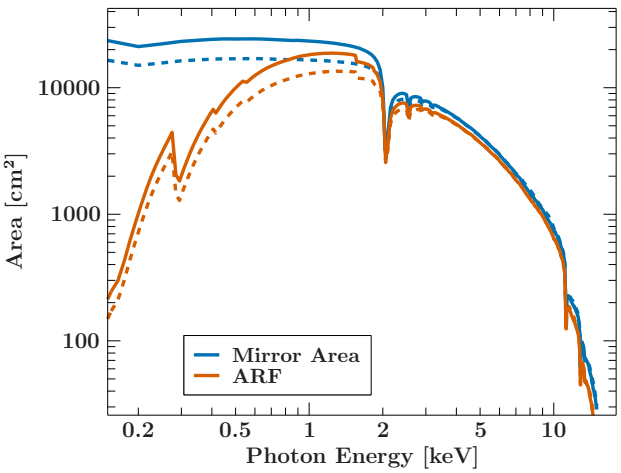

Figure 5.3: The mirror area (**blue**) and the effective area (**red**) as a function of the photon energy, as used by the simulations as presented in this section. The **solid** lines depict the curves for the nominal mirror assembly with a radius of 1469 mm, the **dashed** lines depict the curves for the alternative, smaller mirror design of the CDF study with a radius of only 1190 mm. The effective area takes into account the mirror area but also the quantum efficiency of the detector. Figure modified after Dauser et al. (2015).

Table 5.2: The detector modes as used in the bright source performance study. The window modes reduce only the number of rows, as these are the time-critical aspect for read-out. In these modes, all columns are read out as in the normal mode.

Name	Size (rows×columns)	PSF used	frame length
L	512×512	in-focus	1280 μs
L, W16	16×512	in-focus	40 μs
L, W64, df	64×512	out-of-focus	160 μs
S, W16	16×64	in-focus	20 μs
S, df	64×64	out-of-focus	80 μs

for both detectors, the large and the small one. Additionally, the out-of-focus PSF is used to see how much the distribution of photons over a larger area improves the high-count rate capability. With this larger source image, the window size of the large detector is increased to the same size as the small sensor, i.e., 64 rows. Additionally, the large detector is simulated in standard operation mode for comparison. The different modes are summarised in Table 5.2.

5.2.2 The Influence of the Source Flux

The simulations as described in the last sections are conducted for all of the above optics and detector setups. The simulation data are used to describe the flux dependence of the throughput– and pile–up–functions for each detector. Figure 5.4 shows these functions for all of the mentioned optics and detector versions and window modes. At low flux values of around 0.1 mCrab, all setups lead to a throughput of 100%, which means that all of the photons interacting with the detector are measured. The throughput is stable up to a certain flux limit, at which it starts to drop rapidly. This limit depends on the exact optics- and detector configuration as well as its read-out mode. The decrease is caused by the increasing probability of two or more events hitting the same or neighbouring pixels. Thus, the same source brightness, the pile-up starts to get important and approaches the mark of 1%, which has been shown to be a critical limit for the scientific analysis of the energy spectrum (Dauser et al., 2015). With even more pile-up, the distortion of the spectra increases significantly and the original parameters can not be measured to high precision anymore.

The increase in pile-up with the source flux continues, until a limit of between 10% to 20% is reached. At the same source brightness, the throughput drops below 30%, leaving only a third of all events detected properly. From this point on, the throughput approaches 0% asymptotically. At the same time, the pile-up starts to decrease again. This behaviour can be explained by the pile-up reaching saturation: In the central part of the source's image on the detector, almost all pixels are hit by photons during one frame. This causes invalid split patterns all over the central region of the PSF, which is recognised by the pattern analysis algorithm, rejecting all events in this region. Thus, the signal in the pixels which are affected the most by pile-up are blinded by the bright source. A ring around this region is left over, but as the photon density is lower here,

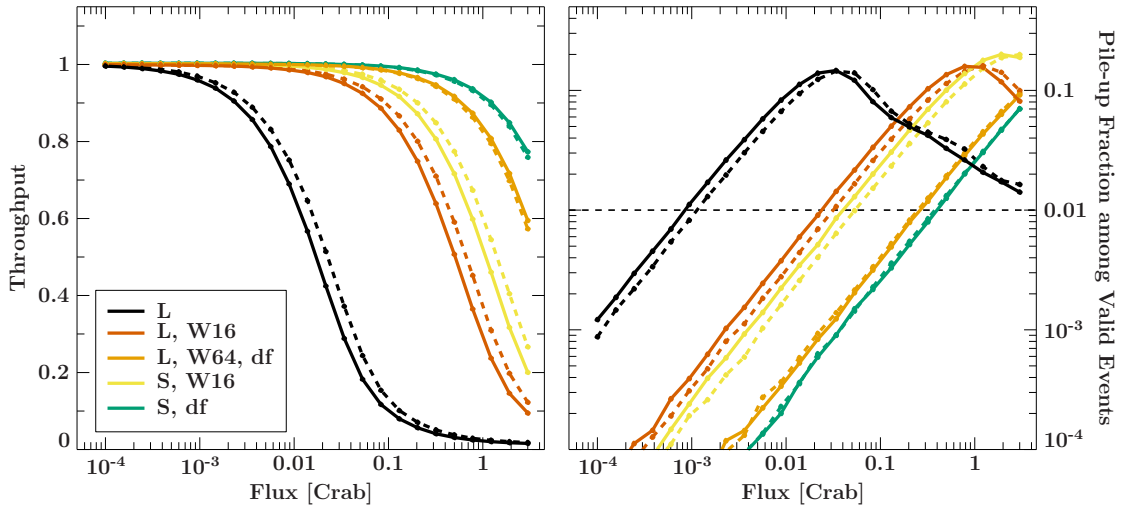

Figure 5.4: The throughput and pile-up performance of the large and small detector for different read-out modes and either in-focus or out-of-focus. The solid lines represent the nominal mirror with a radius of 1469 mm, the dashed lines depict the smaller mirror with a radius of 1190 mm. The **left** panel shows the throughput. As expected, the curves break in at a certain flux limit for each detector, caused by the rejection of piled-up event patterns. The **right** panel depicts the pile-up fraction among all valid events. The curves show a degradation of the spectral quality up to the flux limit for which the respective throughput falls below approximately 30%. For even brighter sources, the pile-up decreases again. The limit of 1% in pile-up is represented by the horizontal, dashed line. Figure modified after Dauser et al. (2015).

pile-up is less probable. With increasing source flux, the blind region grows, and the pile-up fraction among valid events decreases.

The curves shown in Fig. 5.4 show the results of all detector versions listed in Table 5.2 and for both mirror sizes. The large detector in its standard operation mode and a frame duration of 1280 μs is affected the most by pile-up as expected. The pile-up limit of 1% is reached already at around 0.8 mCrab for the nominal mirror. The smaller number of photons focussed on the detector by the smaller mirror delay the degradation a bit, the same limit is reached only at just over 1 mCrab. The benefit of the smaller mirror for bright sources is around the same for all detectors, from now on, only the nominal mirror is discussed. The result for the large detector means that this detector is able to be used in full-frame mode only for sources weaker than 1 mCrab, if spectral quality matters over the whole field of view and all events shall be used for the analysis. However, if the detector is operated in a 16-row window mode, the readout speed is increased by a factor of 32. In around the same amount the bright-source capability increases: The 1% pile-up limit is reached only at about 22 mCrab, and the throughput behaviour improves respectively. A further improvement can be made by using the detector in a defocussed mode, as is indicated in the figure. The out-of-focus position of 15 mm with respect to the focal plane and the detector being read out in a 64-row window shifts the point at which the 1% pile-up limit is reached by another order of magnitude in source flux. This lies now at 220 mCrab for the nominal mirror, with the throughput improving for the same

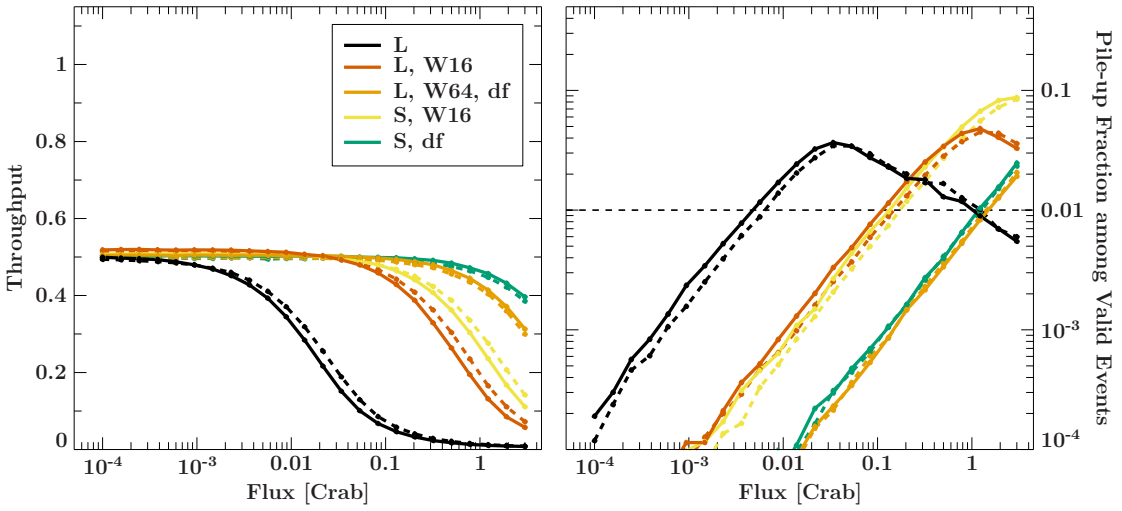

Figure 5.5: The throughput and pile-up performance as shown in Fig. 5.4 but only for single events. Again, the solid lines represent the nominal mirror with a radius of 1469 mm, the dashed lines depict the smaller mirror with a radius of 1190 mm. The throughput is smaller by around 50% for all cases, which is caused by the loss of double-, triple- and quadruple events. However, the rejection of these multi-pixel events improves the pile-behaviour by a factor of around 6 in flux, with respect to the data shown in Fig. 5.4. Figure modified after Dauser et al. (2015).

amount.

The benefit of the small detector is its intrinsic capability to read out two rows at the same time. This further increases the read-out speed, with a duration of 80 μs in full-frame mode. However, if it is used in-focus, the same as for the large detector holds, and a 16-row window is sufficient to detect all events. This mode is still faster by a factor of two with respect to the large detector because of the two-row read-out. This allows the detector to observe sources twice as bright as with the large chip in the same sized window mode, the 1% pile-up limit is reached only at around 44 mCrab. The same improvement can be observed for the out-of-focus simulations, the small detector shifts the maximally observable source flux to over 400 mCrab with the same 15 mm defocusing.

A part of the problem caused by pile-up can be solved by rejecting all split patterns consisting of more than one pixel, leaving only the single events. If a uniform distribution of photons over the pixels is assumed, the probability of a piled-up double event is already eight times higher than a piled-up single event, as the primary pixel has eight neighbours which could be hit. For higher patterns, even more pixels surrounding the primary event are possible, making pile-up in these orders even more probable. Of course, in the case of a focussed detector observing a point source, the photon distribution is not uniform over the pixels. Nevertheless, the PSF of *Athena* is still large enough to illuminate 16 pixels of the WFI with a relative brightness of at least 10% of the pixel lying in the centre of the PSF (Dauser et al., 2015). Thus it is no surprise that the pile-up behaviour improves considerably if only single events are analysed, as Fig. 5.5 shows. Of course, this approach requires to reject a large number of events. The throughput curves shown

in the plot predict that around one half of all events is lost. But the benefit is a gain in a factor of around 6 in terms of the maximally observable source flux, measured at the 1% pile-up limit. Using only single events and either the large or small detector in a defocussed position, sources brighter than 1 Crab can be observed with acceptable spectral quality. As using the small detector in a position out-of-focus seems to be a preferable solution for bright sources, the next section deals with the question of the best amount of out-of-focus mounting.

5.3 Optimisation of the WFI's Small Sensor

The purpose of the small detector of the WFI is to deliver a high–countrate capable option with otherwise identical parameters as the large field-of-view detector. As explained in the previous sections, this is achieved by the combination of a relatively low number of rows which need to be read out and the ability to read out two rows at the same time. However, as the analysis presented above shows, another huge gain in high–countrate capability can be achieved by using the detector in an out-of-focus position. In this first study, a fixed position of 15 mm above the focal plane has been used. This value for the offset is a preliminary estimate, only thought to be a guideline for the general prove of concept. In this section, the bright source performance is tested for its dependence of the exact value of the offset. The explanations as presented in this section follow the discussions by Brand et al. (2015).

Figure 5.6 shows seven radial surface brightness density functions calculated by Richard Willingale using ray-tracing simulations. The curves give sections of the profiles of PSFs for different detector offsets, ranging from 10 mm to 40 mm with respect to the focal plane. Especially above an offset of 15 mm, they show an approximately linear increase of the radius of a flat disk with increasing out-of-focus position. Only the inner millimetre

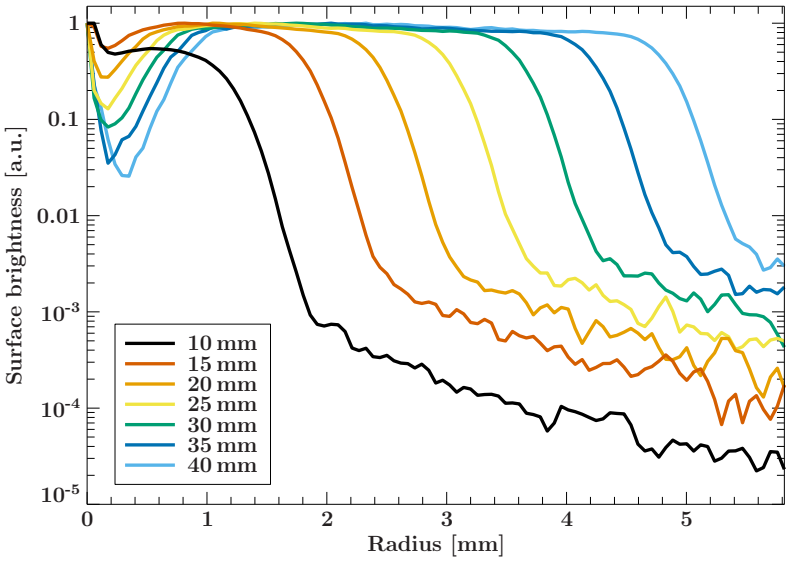

Figure 5.6: The surface brightness density functions for the *Athena*-mirror and the detector mounted out of focus as simulated with SIXTE. The position of the detector plane along the optical axis is given relative to the focal point. The fluctuations at low levels are due to noise in the original ray-tracing simulations performed by Richard Willingale For the simulations, these profiles have been used to create rotation-symmetric 2D PSF-profiles.

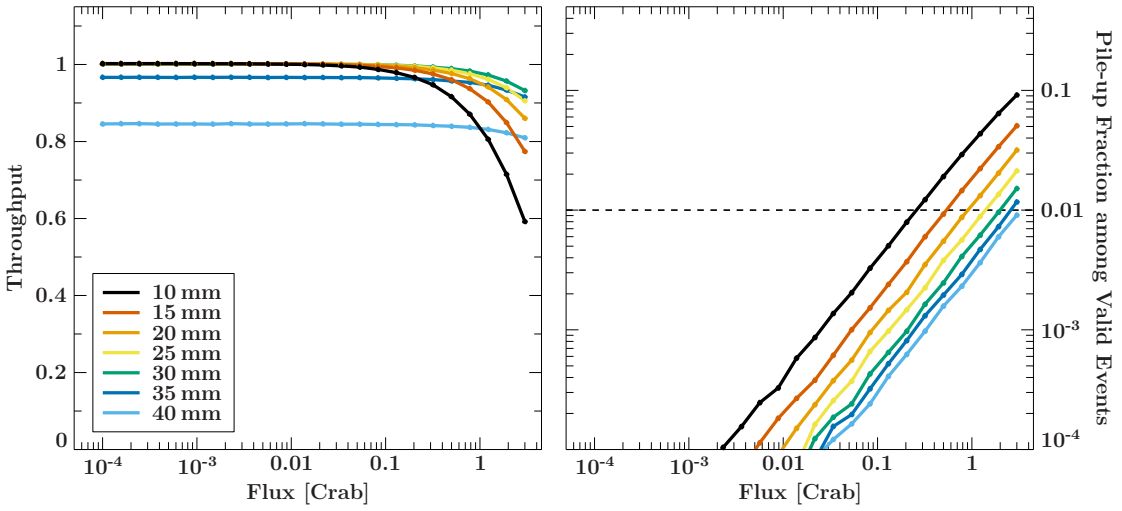

Figure 5.7: Left: The throughput as a function of the source flux for different out-of-focus positions, ranging from 10 mm to 40 mm. It can be seen that the break-in of the detected photon number shifts towards higher fluxes for stronger defocussing. Only for the highest values of the positional shift a general loss of detections sets in, due to the PSF growing over the detector borders. **Right**: The pile-up fraction for the different out-of-focus positions as a function of the source flux. The problem of pile-up increases with higher photon density, and improves with the light being distributed over a larger PSF area. The difference between the 10 mm and 40 mm positions leads to an improvement of the maximally observable flux (1% pile-up) from around 0.25 Crab to around 3 Crab. Figure modified after Brand et al. (2015).

forms a dip. For high defocusing, the PSF is transforming into an image of the reflective surface of the focussing mirror of *Athena*, which blocks the light at the centre. The functions depicted in this figure are used to create PSF-images which can be fed into SIXTE. With these files, simulations similar to the ones in the previous section are performed, using only the small detector of the WFI.

The results of these simulations are shown in Fig. 5.7. It describes the throughput and pile-up performance as a function of the source flux, as already discussed in Sect. 5.2.1. This time, the different curves depict the behaviour of the small chip for the seven different out-of-focus positions with the PSFs shown in Fig. 5.6. For these curves, all valid events, regardless of the pattern type, have been analysed. Not surprisingly, the curves for 15 mm defocussing are similar to the curves presented in the previous section for the defocussed version of the small detector. For higher offsets, especially the pile-up fraction improves because the photons are distributed over a larger area, decreasing the probability that neighbouring pixels are hit during the same frame. For the highest value of 40 mm, the 1% pile-up limit is reached only at slightly above 3 Crab.

However, for offsets above 30 mm, the throughput decreases even at low source fluxes, which are not affected by pile-up. This can be explained by the size of the PSF growing over the sensitive area of the detector, as Fig. 5.8 illustrates. It shows the image of the PSF on the detector, as measured directly from the event data simulated by SIXTE. For an out-of-focus position of 25 mm, the PSF fits well inside the 64×64-pixel array of the sensor, for 35 mm it is already slightly larger than the small field of view.

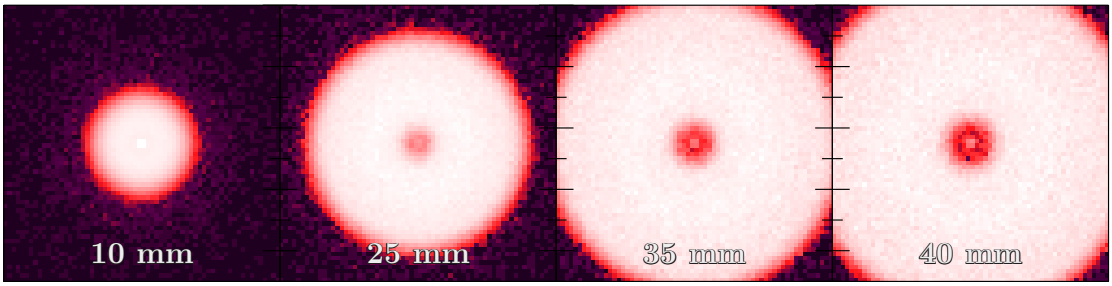

Figure 5.8: The picture of a point source as seen by the high-countrate capable detector of the WFI with different out-of-focus positions. It can be seen that the disk of the PSF grows over the small field of view of the detector for out-of-focus positions over 35 mm. For smaller shifts from the focal plane, the PSF is smaller and the photon density is higher. Figure from Brand et al. (2015).

As presented in Sect. 5.2.1, the amount of pile-up can be further reduced by using only single events in the analysis. For the brightest sources, the resulting loss of the number of counts available for the scientific analysis after the rejection of higher event patterns may be tolerated, as the count rate is very high for these sources. In this case, even with an offset of only 10 mm, sources brighter than one Crab can be observed below the 1% pile-up limit, as Fig. 5.9 shows. With an offset of 40 mm, the extrapolation of the curves presented in this figure indicates that sources with a brightness of around 10 Crab can be observed with the same pile-up limit. Bringing together the benefits of good spectral quality even at high count rates with the loss of throughput at the highest simulated detector position, the location of 35 mm above the focal plane seems to be the best trade-off for the small sensor of the WFI.

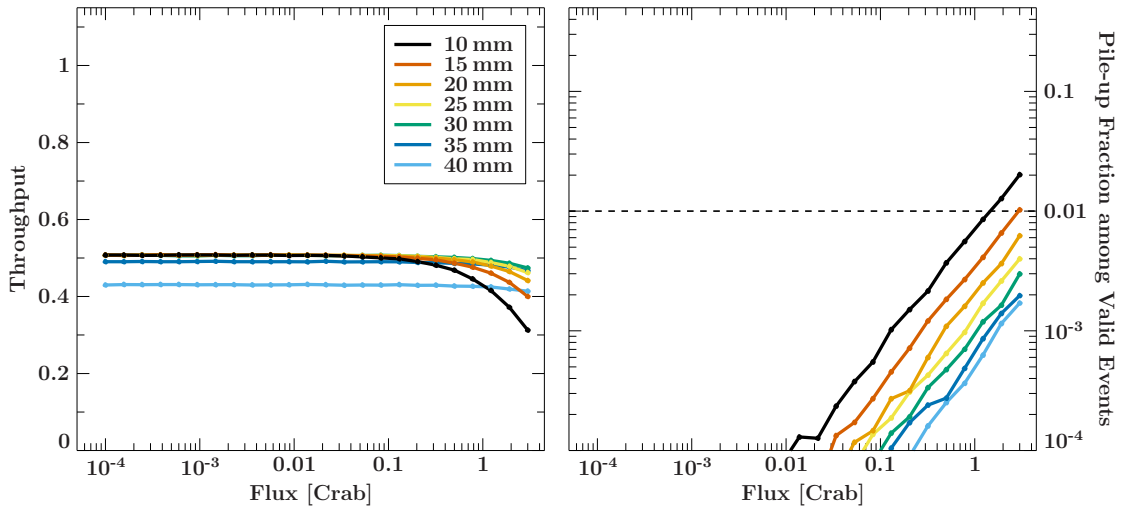

Figure 5.9: The throughput and pile-up performance of the small detector of the WFI as shown in Fig. 5.7, but only using single events. This helps to further improve the high-count rate capability, but decreases the number of events available for scientific analysis. Figure modified after Brand et al. (2015).

In summary, the simulations conducted in the last sections show that the WFI is able to handle bright sources with a flux of up to 3 Crab without a significant distortion of the spectrum caused by pile-up. At the same time, almost all photons interacting with the sensor are available for scientific analysis. In this respect, the division of the instrument into two detectors helps to fulfill a broad variety of requirements, from a field-of-view as large as possible to the observation of bright sources. With this division, the two parts of the WFI can be optimised individually to the special needs. The simulations conducted in this section show that not only the design of the sensor itself is vital for its capability to observe bright sources. The precise position in which it is placed relative to the mirror decides about the image quality. For most imaging detectors, the light will be focussed as good as possible, resulting in a sharp image of the sky. However, as the imaging requirement is already fulfilled with the large field-of-view detector, the high-countrate-capable detector can be optimised even by sacrificing the ability to be used for imaging. It has been shown that by placing it at a height of 35 mm above the focal plane, the photon density is decreased such that it can take spectra from sources as bright as 3 Crab with less than 1% pile-up contamination and almost 100% in throughput. Neglecting higher event patterns than single events further increases the high-countrate capability to around 10 Crab. This result has firstly been considered for the actual detector design by Meidinger et al. (2015) and is now part of the baseline design (Meidinger et al., 2016).

6 Measurements at the SPIX II-Experiment at MPE

As discussed in the previous chapters, the two instruments of the *Athena*-mission are in a development phase where design details are still under evaluation. Because of this, we have to rely on theoretical predictions or measurements from prototype models to simulate effects specific to the new technology. This is the motivation for measurements performed at the Max-Planck-Institut für extraterrestrische Physik (MPE), where the so-called Single PIXel (SPIX) II setup has been used to measure the temporal behaviour of early prototypes for the DEPFET-sensors of the WFI during the read-out time interval. The setup is the second iteration of the SPIX as described by Wölfel (2007) and Bähr (2010). The SPIX II allows one to illuminate parts of the sensor with a laser. The laser does not radiate continuously, but is pulsed and can be synchronised to the read-out sequence. This allows one to inject signals only at precisely defined times, such that the predictions made for the sensor's response can be compared to actual measurements. In addition, measurements with ^{55}Fe-sources can be performed. The X-ray spectrum of this radioactive isotope features emission lines at known energies and is used to calibrate the gain of the pixels. A particular focus for the measurements has been set on the effects taking place at the end of the clear time. In the following sections, the SPIX II setup and the data sets will be explained, followed by a description of the analysis of the data and the results.

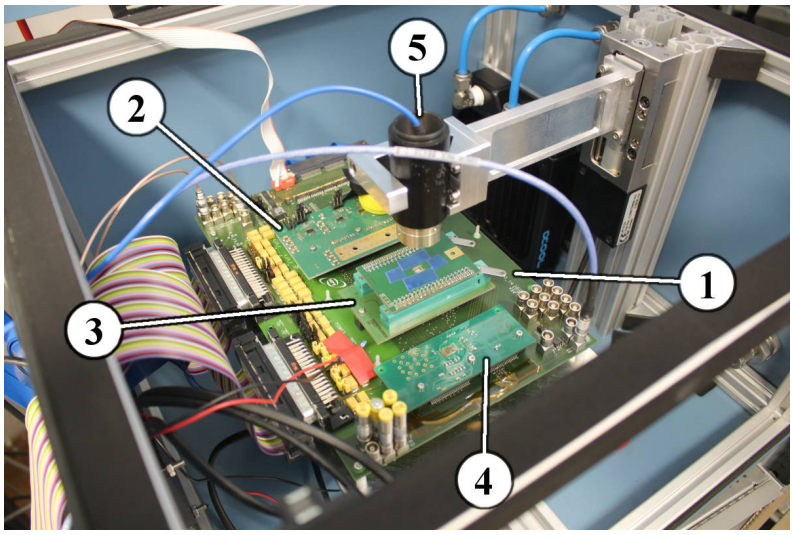

Figure 6.1: The SPIX II-setup inside the light-shielding box. On a X-Y-manipulator, the Base Board is mounted (**1**), which holds the Switcher Board (**2**), the DUT Board with the sensor (**3**) and the Readout Board (**4**). The laser fibre is fed into a lens (**5**) and can be manipulated by a Z-motor to focus the light. The setup is driven by the X-board from the outside, which synchronizes the operation of the sensor-, readout- and data aquisition components.

6.1 The setup of the SPIX II experiment

The measurements presented in the following sections are made with 4×4-pixel test structures from previous DEPFET-productions. MPE has developed a small and flexible setup called SPIX II (Fig. 6.1), which can handle single pixel structures as well as small arrays. The components of this setup control the device and read out the measured signals. Additionally, it features a laser diode which can be synchronised with the read-out sequence. The core setup consists of four boards. The Base Board, to which the Switcher Board, the Device Under Test (DUT) Board, and the Readout Board are connected (see Fig. 6.2 for a scheme of the components).

To allow for quick changes of the sensors, SPIX II is operated under normal atmosphere and room temperature. This circumstance means that the measured noise level is significantly higher than that of in-space detectors. The increased noise is not a problem for the purpose of this work, as the main interest lies on the temporal behaviour of the signal, and not on the total energy resolution. The sensor is mounted on the DUT Board, which consists of an Interlink Printed Circuit Board (PCB), connected to the ceramic board to which the sensor is glued and bonded. The ceramics with the sensors are connected via two 20-pin Zero Insertion Force (ZIF)-sockets.

The gate, clear, and clear-gate voltages of the DEPFET-sensor are controlled by the four SwitcherS-ASICs. They are mounted on the Switcher Board. In the configuration used in the following measurements, the switchers select one pixel row at a time. The charge collected in the pixels of this row is read out with a VERITAS 2.0 (Porro et al., 2014) ASIC mounted on the Readout Board. The resulting readout sequence is shown in Fig. 6.3. The Base Board's function is to provide a platform for the Switcher, DUT and Readout Board and to distribute the controlling signals to these components. It is fed with driving signals from the external X-Board, which is programmed with the sequencing code for the experiment. Using this setup assures that switching, readout, and data acquisition are synchronized.

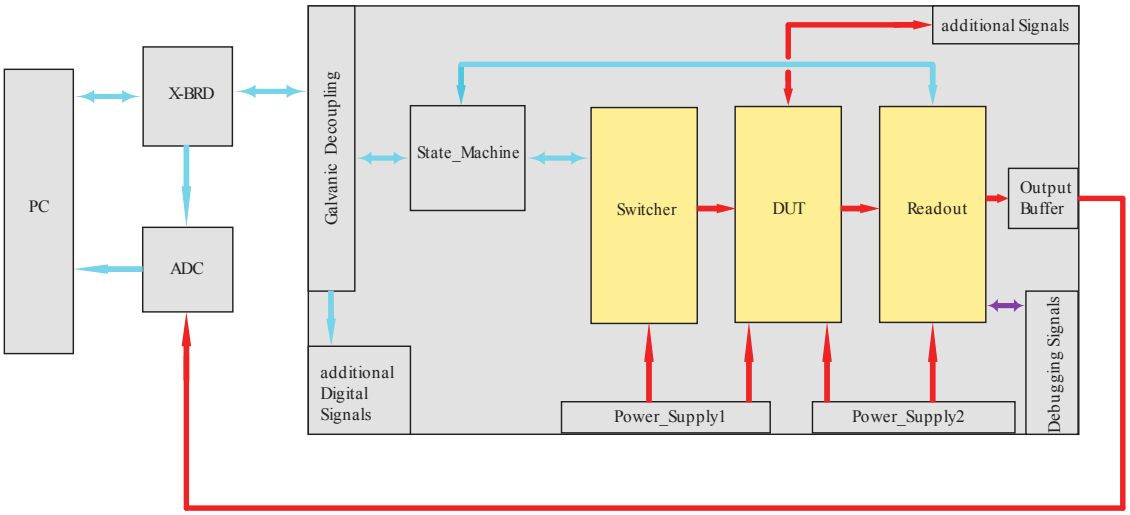

Figure 6.2: Block diagram of the electronic components of the SPIX II-setup. The Switcher Board, DUT Board and Readout Board (highlighted in yellow) are described in the text and can be seen in Fig. 6.1. The periphery components (highlighted in gray) are not further discussed. Figure modified after A. Bähr, priv. comm..

This unit is mounted on a manipulator which can move the boards in the X- and Y- position. The optical signal which is observed by the sensor for the measurements described in the following sections is produced by an ALPHALAS PICOPOWER LD–660–50–FC laser diode powered by an ALPHALAS PICOPOWER PLDD–50M driver. The diode emits pulses with a width of 60 ps to 80 ps, depending on the exact frequency in which it is triggered. This is described in the Individual Test Data Sheet for the PICOPOWER–LD–660–50–FC Laser (Serial # PPR1412–01) and Laser Diode Driver PLDD–50 (Serial # PPBR1412–01) combination. This pulse length is shorter by around two orders of magnitude to the time distance with which the read-out sequence has been sampled, so the temporal characteristics of the laser pulses are not relevant. The laser diode irradiates red light with a wavelength of 660 nm. This wavelength equals a photon energy of $E = h \cdot c/\lambda \approx 1.9\,\text{eV}$. In Silicon, with a band gap of approximately 1.1 eV (Knoll, 2010, p.368), one photon with this energy is able to lift a single electron into the conduction band, so the total number of electrons measured by the sensor after a laser pulse is proportional to the number of photons hitting the detector. The brightness of the laser pulses can be varied by changing the “pulse power”.

The laser driver is fed with a trigger signal from a AGILENT B1104A-pulse-/pattern generator. The pattern generator is synchronized to the DEPFET’s frame cycle and is configured such that it triggers the laser driver at every 5th read-out sequence to emit a pulse. Additionally, it allows to delay the trigger via a time offset commanded from a PC, which makes it possible to shift the injection time with respect to the beginning of the read-out. The delay is measured from the rising edge of the sequence which was used to trigger the laser. The absolute value of the delay is without a meaning for the course of this work, but it serves as a way to shift the injection time to a particular point during the read-out

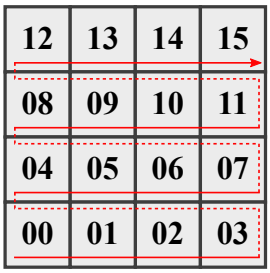

Figure 6.3: The pixel numbers as used in this work. During the read-out at the end of a frame, one row of the 4×4-matrix is selected at a time, starting with the lowest row. When a row is selected, the pixels of that row are read out in sequence, from left to right. As the end of the row is reached, the Switcher Board deselects it and selects the next one, until the whole array is read out. Afterwards, a new frame starts. Two kinds of measurements have been undertaken: Measurements with all light focussed onto one pixel, and measurements with the laser defocussed and the whole array illuminated. For all in-focus measurements, only pixel 05 was used to prevent border effects.

of a certain pixel row.

The commanding software also allows so-called sweep measurements. Here, the delay for the laser driver is stepped through a user-defined interval. At each step, the setup records the output of a pre-defined number of frames which can be converted to a spectrum. sweep measurements allow to probe the read-out interval of the sensor in a reliable and reproducible way and are used for all but the calibration measurements described in the following sections.

6.2 Measurements for two sensors

During April 2016, I performed a total of 27 measurements for the two DEPFET-sensors *P05_W81_Q10* and *P05_WS80_Q10*, 20 of which are sweep measurements over the read-out time of the second row of the 4×4-matrices. The two sensors are of identical layout. A scheme similar to the sensors is presented in Fig. 3.7. The 16 pixels of each device have a size of $75\,\mu\text{m} \times 75\,\mu\text{m}$ and are constructed on a bulk with a thickness of $450\,\mu\text{m}$. The difference between both sensors is the use of different silicon wafers for their fabrication. Even with similar production, the doping of the bulk may vary slightly, resulting in different depletion voltages. The complete lists of operating voltages applied to the sensors during these measurements are given in Appendix A.1. The main difference between the pixels as presented here to the pixels which will be used for the WFI is their size. As discussed before, the current instrument design aims for square pixels with a length of $130\,\mu\text{m}$. This means that the results gained from the measurements in this chapter can well be transferred to the WFI, but the exact values of the model parameters will be different.

The sweep measurements undertaken with these sensors sample the examined time interval in 10 ns-steps, starting at a time offset of 5000 ns and ending at 13000 ns, covering the whole read-out of the second row. At each of these time steps, a spectrum with 49995 frames was integrated. At every 5th frame, the laser injects a light pulse, followed by four dark frames. For an ideal detector, this would correspond to a proportion of 1:4 between the area of the signal and noise peaks. Between the different sweep measurements, the pulse power of the laser was varied, resulting in different amounts of energy deposed inside the sensor for each data set. As another parameter, the focusing of the laser was changed by moving the laser's optics in Z-direction. For both sensors, measurements with the laser focussed onto pixel 05 (see Fig. 6.3) as well as out-of-focus measurements have

Table 6.1: Laser measurements with the detector *P05_W81_Q10*. The equivalent energy given in the table is determined from the analysis results.

Name	Pulse Power	Equivalent Energy (Pixel 05)	Focus Position
P05_W81_Q10_160425_02	6.00	8.9 keV	in-focus
P05_W81_Q10_160425_03	5.00	2.2 keV	in-focus
P05_W81_Q10_160425_04	4.50	0.7 keV	in-focus
P05_W81_Q10_160425_05	5.50	4.7 keV	in-focus
P05_W81_Q10_160425_06	5.75	6.4 keV	in-focus
P05_W81_Q10_160425_08	5.25	3.3 keV	in-focus
P05_W81_Q10_160426_02	7.50	1.1 keV	out-of-focus
P05_W81_Q10_160426_03	8.00	2.2 keV	out-of-focus
P05_W81_Q10_160426_04	8.50	5.9 keV	out-of-focus
P05_W81_Q10_160426_05	8.75	9.3 keV	out-of-focus
P05_W81_Q10_160426_06	8.25	3.2 keV	out-of-focus
P05_W81_Q10_160426_07	7.75	1.5 keV	out-of-focus

Table 6.2: Laser measurements with the detector *P05_WS80_Q10*. The equivalent energy given in the table is determined from the analysis results.

Name	Pulse Power	Equivalent Energy (Pixel 05)	Focus Position
P05_WS80_Q10_160428_02	5.00	2.1 keV	in-focus
P05_WS80_Q10_160428_03	6.00	8.3 keV	in-focus
P05_WS80_Q10_160428_04	5.50	4.4 keV	in-focus
P05_WS80_Q10_160428_05	4.50	0.7 keV	in-focus
P05_WS80_Q10_160429_02	7.50	0.9 keV	out-of-focus
P05_WS80_Q10_160429_03	8.00	1.8 keV	out-of-focus
P05_WS80_Q10_160429_04	8.50	5.2 keV	out-of-focus
P05_WS80_Q10_160429_05	8.75	8.4 keV	out-of-focus

been taken. The data sets used in the following analysis are listed in Tables 6.1 and 6.2.

In addition to the sweep measurements, calibration measurements were taken with a ^{55}Fe-calibration source to determine the absolute gain of the pixels. For the analysis, the calibration measurements listed in Table 6.3 have been used. They were analysed using the MPE-software ROOT Offline Analysis (ROAn)(Lauf & Andritschke, 2014), which performs a pattern analysis and fits line profiles to the noise peak as well as the Mn Kα and Mn Kβ-peaks. The line positions are important for the following analysis because they can be used to determine the gain, which is the conversion factor between the ADC's channel number and the energy of the photon producing the signal. The gain is determined for each pixel individually and saved in a gain map for further use. The software also produces offset maps which give the position of the noise peak for each pixel. As the following measurements allow simultaneous observation of the noise peak and signal peak(s), the offset is directly determined from each spectrum to prevent long-term drifts influencing the calibration quality.

Table 6.3: Fe55-calibration data used to calculate the gain maps.

Name	Detector	Validity Date
P05_W81_Q10_160425_01	*P05_W81_Q10*	2016 April 25
P05_W81_Q10_160426_01	*P05_W81_Q10*	2016 April 26
P05_WS80_Q10_160428_01	*P05_WS80_Q10*	2016 April 28
P05_WS80_Q10_160429_01	*P05_WS80_Q10*	2016 April 29

6.3 Data extraction

The purpose of the measurements described in this work is to test our understanding of the effects which take place if a photon hits a DEPFET-pixel during its read-out. This means that the peak positions, which encode the measured energy of a photon, need to be extracted from the spectra. In the following, the process which is used for this task is described. An example raw data histogram and the extracted peak positions are shown in Fig. 6.4.

The data recorded with the SPIX-software are stored in a raw-data format. I have written a ROOT-program to convert the raw data into FITS-files, which contain the pixel's signals of one frame per row. The calibration maps from ROAn are also converted into FITS-tables. The analysis I programmed reads these FITS-files and is written in Python[1] 2.7, depending on the packages NumPy[2] (tested with version 1.11.1), Matplotlib[3] (version 1.3.1), lmfit[4] (version 0.9.3), SciPy[5] (version 0.18.0rc2), and the modules copy and os.

The core of the analysis consists of the peak-detection and -fitting step. With the setup used for this work it has been impossible to correlate the frame number with the trigger time of the laser. This means that the analysis algorithm needs to determine the position of an unknown number of peaks - noise peak and signal peaks - in a reliable way. As described before, a sweep measurement takes a spectrum at each injection time, which is stepped through by the control software. In the case of the laser experiments presented here, each spectrum consists of the noise peak, and either no, one, or two signal peaks. We expect one signal peak during the time in which the pixel is not read out, as well as during the time before the end of the first integration and after the second integration. If a photon produces a charge cloud during the clear time interval, an ideal sensor would not measure any of this signal as it is immediately removed through the clear. However, as the voltage applied to the clear is finite and the charge cloud has a finite speed and extent, we will measure at least parts of it if it is created at the end of the clear time interval, when the clear is deactivated before the whole charge is removed. Because of the subtractive measuring principle of the DEPFET as described in Sect. 3.2.3, the remaining charge is measured twice: once in the frame in which it is produced, but

[1] https://www.python.org/
[2] http://www.numpy.org/
[3] http://matplotlib.org/
[4] https://lmfit.github.io/lmfit-py/
[5] http://www.scipy.org/

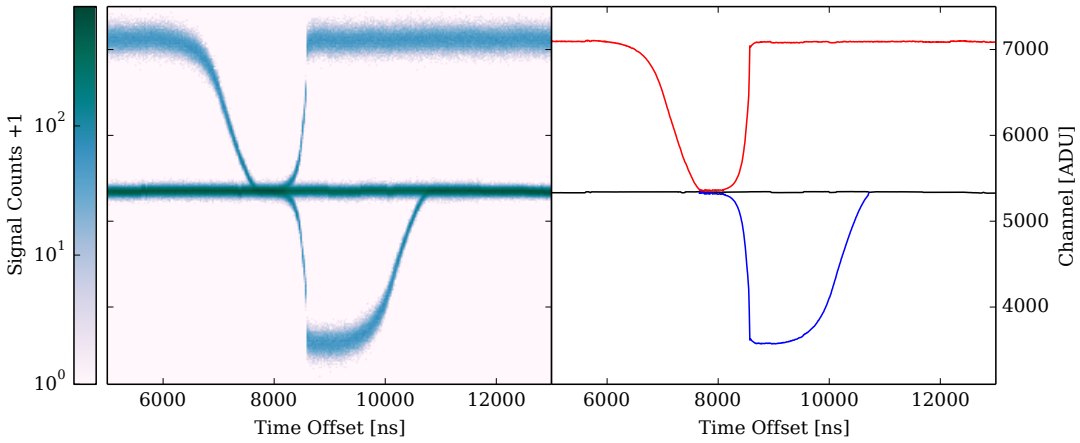

Figure 6.4: An example of the peak detection's in- and output. The figure shows the data of pixel 05 for the measurement `P05_W81_Q10_160425_03`. **Left**: The sweep measurement gives one spectrum for each selected injection time offset. The strong noise peak is relatively stable over time, while the signal peaks vary due to the effects taking place during the pixel is read out. **Right**: The peak detection algorithm finds the number and position of the peaks in the spectrum and fits a model composed of up to three Gaussian functions to the data. Shown are the centres of the noise peak (black line), the positive signal peak (red line) and the negative signal peak (blue line).

with a negative sign, and once in the next frame, with a positive sign like any other charge created in the next frame. As the existence of the third, negative peak is caused by the second integration measuring more charge inside the pixel than during the first integration, the peak disappears with the end of the second integration.

Together with the knowledge of the laser pulse injection frequency of one pulse per five frames, we can calculate the area ratios of the peaks: If there are two peaks, we have four empty frames per illuminated frame, resulting in a ratio of the peak areas of 1:4. If there are three peaks, we have one frame with negative energy, one with positive energy, followed by three empty frames. This results in a peak area ratio of 1:1:3.

As a typical sweep measurement contains several hundred spectra, the analysis needs to be automated and must be able to work equally well over a broad range of peak distances and peak numbers. Especially important are the spectra in which the peaks are very close to each other, as will be explained in later sections. Simple, general peak detection algorithms, such as SciPy's `find_peaks_cwt`-function, which are based on absolute heights of the bin values or a smoothed version of it, have proven to find only a single peak when two maxima are very close to each other.

For the purpose of the laser measurements as presented here, a new algorithm has been developed which is based on fitting Gaussian functions to the spectrum. This is done in three steps. At first, the number and approximate position of peaks are detected. In the second step, a fit with the derived number of lines is performed. These two steps are done sequentially for all spectra of a sweep measurement. In the third step, the resulting best-fit peak positions of all spectra of the measurement are read in and smoothed, to determine new starting parameters for a second fit to each spectrum. This step success-

fully corrects cases in which the peak detection missed a peak. The individual steps are described in more detail in the following.

6.3.1 Peak Detection

The peak detection algorithm as used for the analysis presented here is optimised for the data from DEPFET-laser measurements. It works with a high signal-to-noise ratio, where the background count number between the peaks is mostly zero. It divides the spectrum into blocks which have to be separated by at least `mindist` bins and in which there are at least `vmin` counts in each bin. In the following sections, `mindist` was set to 50 bins and `vmin` to 10. These blocks are sorted by their integrated number of counts. As the ratio between the noise peak area and the signal peak area is known as described before, the block with the highest number of counts must contain the noise peak, for which the bin with the highest count number is chosen as the first guess of the center. If there is a second block, it has to contain exactly one other peak, as would be the case if there is a third block. As the peaks might be very close together inside one block, the algorithm puts additional peaks into the block with the highest signal sum, until the maximum of 3 peaks is reached. The first guesses for the centres of these peaks are shifted to the noise peak: if the positive signal peak has already been placed in its own block, the 3rd peak is initialized at 10 bins below the noise peak. If both signal peaks are initialized inside the noise peak's block, they also are shifted by 10 bins from the noise peak. These parameters have proven to work well with the processed data.

The initialization is followed by a first fit of three Gaussians (Eq. 6.1) to the spectrum, using the first-guess positions x_c and a σ of 20 bins.

$$y(x) = a \cdot \mathrm{e}^{-\frac{(x-x_c)^2}{2\sigma^2}} \tag{6.1}$$

The amplitude a is set to 0.3 of the maximum height of the block for the noise peak. The amplitudes for the signal peaks are constrained to match the area ratio of 1:1:3 during the fit. This allows the peaks to grow upwards during the fit iterations. As during the fit peaks with first guess centres very close to each other can switch places, they are sorted afterwards, in the order of noise peak to positive signal peak to negative signal peak. The signal peaks are now tested for their distance, their absolute position, and their width. Signal peaks with centres outside the range of the spectrum are deleted, as are signal peaks closer than one bin together or broader than 1000 bins.

6.3.2 Peak Fitting

After the first guess for the number and parameters of the peaks, a final fit is performed. For the parameter initialization, the peak positions are directly adopted from the first guess. The σ-values are lowered by 10 channels to allow for a re-grow of the Gaussians from the inside. The amplitude of the noise peak is lowered by 10 counts to support this behaviour. The re-growth approach proved to improve the fit quality and stability in rare

cases. The amplitudes of the signal peaks are constrained to the area ratio of either 1:4 or 1:1:3 during the fit, depending on the number of peaks used.

6.3.3 Fit Refining

The first two steps of the peak fitting algorithm only work with the information from one spectrum at a time. This design allows it to be used also for stand-alone spectra, but neglects the fact that in most cases, two succeeding spectra in a sweep measurement are very similar. With this information, the occurrence of outliers can be suppressed. The third stage of the algorithm is designed to do exactly this. At first, the results of the second stage are read in for the whole sweep measurement. All best-fit parameters of slices in which the centre of either the noise- or signal peak is found to be infinite are neglected, followed by a filter which accounts for the difference of the peaks' position in adjacent spectra. The filter discards parameter sets in which either the noise- or the signal peak changed by more than the half of the full signal height and at least more than 20 bins, if the signal height is very low. The remaining best-fit peak centres, widths and amplitudes are interpolated linearly for the missing time steps as initialization of a final fit.

The occurrence of a third peak is decided by the asymmetry of the spectrum with respect to the noise peak centre. A good indicator is the cumulative sum of the spectrum. If there is only the noise peak or if there are two additional signal peaks, equal numbers of counts will be distributed above and below the noise peak, and the cumulative fraction of counts at the position of the noise peak will be 50%. If only the positive signal peak exists, there are more counts at bins above the noise peak, and the cumulative fraction of counts at its position decreases. In reality, the 50% criterion is not exact, as the measurement of the spectrum is a statistical process and the position of the noise peak is not found exactly by the previous stages. However, the more the cumulative fraction at the noise peak position deviates from 50%, the higher is the probability that there is only the positive signal peak in the spectrum. In the following analysis, a criterion of 45% works for all cases except one (`P05_W81_Q10_160426_05`, pixel 10), which has no negative signal peak at all. For this special case, the algorithm was manipulated manually to fit only two peaks.

A problem which occurs at very high signal heights is the signal peak moving past the dynamic range of the readout electronics. If this happens, the lowest or highest bin inside the dynamic range is filled with the total number of counts of the respective peak outside the dynamic range. In this case, the peak fitting stage proved to be unreliable. The resulting errors can be corrected at this stage. The dynamic range of the measurement is determined by scanning the complete set of spectral data, looking for the lowest and highest filled bin. The highest and lowest bins inside the dynamic range could be affected by the issue, altering the shape of the peaks which leads to a bad fit. For the fits of the third stage, they are neglected. The initial parameters for the centres of the signal peaks are also limited to the borders of the dynamic range.

After this analysis of the results of the second stage's fits, a final fit is performed for every spectrum. The statistical parameter uncertainties for the peak centres are calculated

for upper limits of the $1\,\sigma$-confidence interval with an accuracy of 0.25 bins, using the $\Delta\chi^2 = 1$ criterion (Lampton et al., 1976). A higher accuracy for the statistical uncertainty of the fits is not necessary because systematic effects due to vibration of the setup and long-term stability of different components dominate the total uncertainty. These are estimated during later steps of the analysis.

6.3.4 Systematic Uncertainties and Gain Calibration

The data extraction has been performed successfully as described in the previous sections. Before the analysis of the temporal behaviour of the two sensors is described in Sect. 6.4, a first look at the fit results is given. In the following sections, only the positive signal peak is shown. It is offset-calibrated by subtracting the noise peak's centre from its position. Additional systematic uncertainties are estimated using the first and last 100 data points of each sweep measurement, from which the standard deviation of the offset-calibrated signal peak position is calculated. This is added in quadrature to the statistical uncertainties for each data point,

$$\Delta C = \sqrt{\Delta C_{\text{sys}}^2 + \Delta C_{\text{stat}}^2}\,. \tag{6.2}$$

As the centre positions of the peaks are still in units of the ADC's channels, the gain maps described in Sect. 6.2 are now used to convert the signal height into eV.

The equivalent signal height is estimated from the mean value of the first and last 100 data points.

6.4 The Temporal Behaviour of *P05_W81_Q10*

The primary question which led to the measurements has been to characterise the transition from zero to the full signal, which happens when a X-ray photon produces a charge cloud around the time the clear is turned off. After the successful peak fitting, the time dependence of the measured signal can be examined by looking at the gain-calibrated signal height curves. Before comparing models to the measurements, the extracted data are described in the following.

The pulse powers chosen for the in-focus measurements with the sensor *P05_W81_Q10* result in a range from 0.7 keV to 8.9 keV. The complete normalized signal data of pixel 05 for these measurements is shown in the upper panel in Fig. 6.5.

It can be seen that all six data sets are very similar. The only energy dependence noted is located at the end of the clear time interval, when the signal curve rises again from zero to the full signal height. The inset in the figure shows this feature in more detail. Other than during the time between the start of the first integration and the end of the clear, the signal is very stable. This stability changes when the laser is out of focus, as the bottom panel in Fig. 6.5 shows. The figure again shows only the signal measured inside pixel 05. Now, the signal drops by a few percent of the total height during the whole

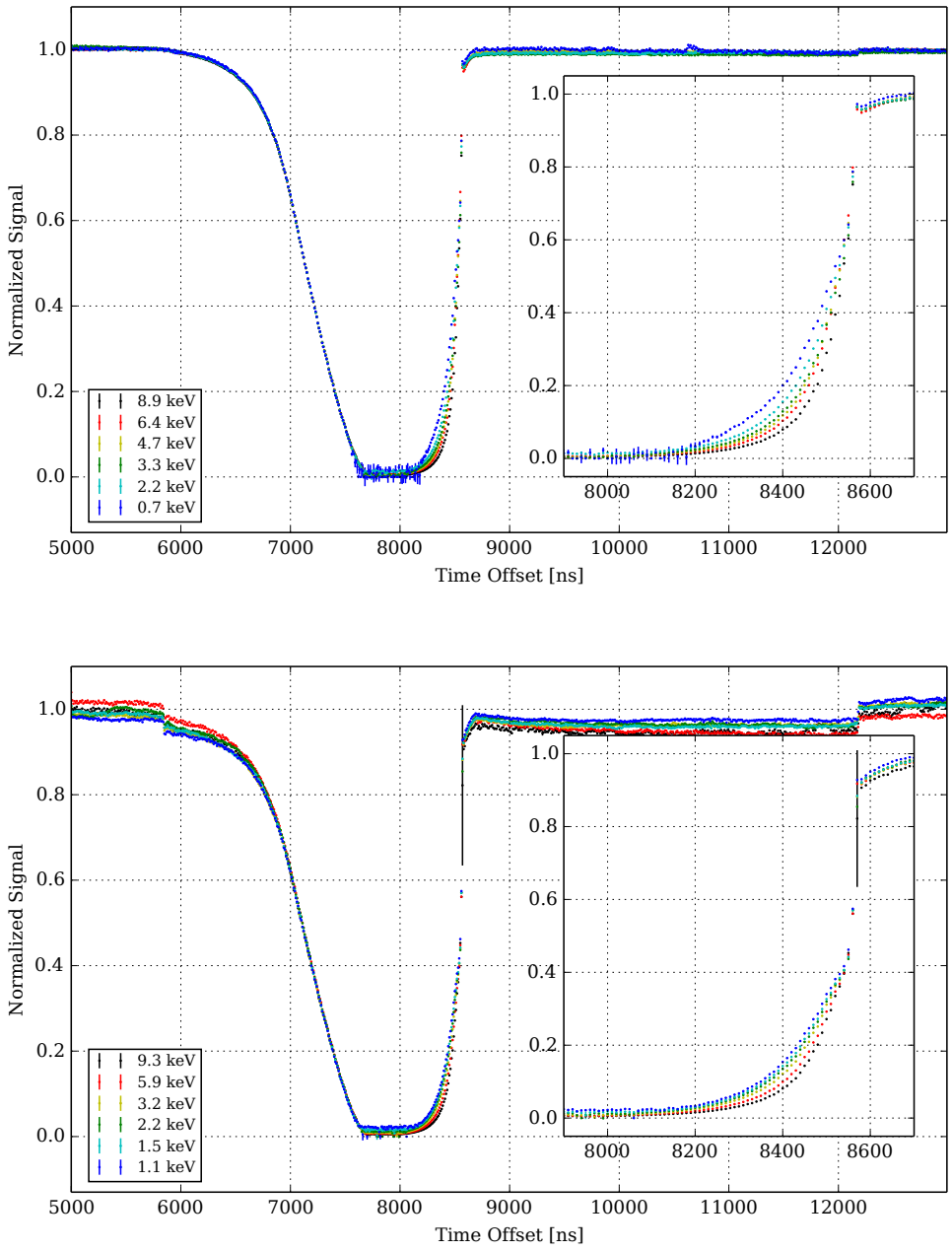

Figure 6.5: Top: The normalized reconstructed signal height inside pixel 05 of the sensor *P05_W81_Q10* as a function of the energy deposition time during the read-out of the pixel. Color-coded is the amplitude of the signal, which can be converted to an energy equivalent corresponding to a single X-ray photon. The inset shows a zoomed-in view of the gradual rise of the positive signal at the end of the clear time interval caused by the finite speed with which the charge is removed from the pixel. The data presented in this graph was taken with the laser maximally focussed to the center of the shown pixel. **Bottom**: The same as above, but with the laser being out-of-focus, illuminating the whole 4×4-pixel array of sensor *P05_W81_Q10*. This causes the charge inside pixel 05 to be distributed not only at the center but also over the outer areas, from which it has to drift a longer distance to the clear.

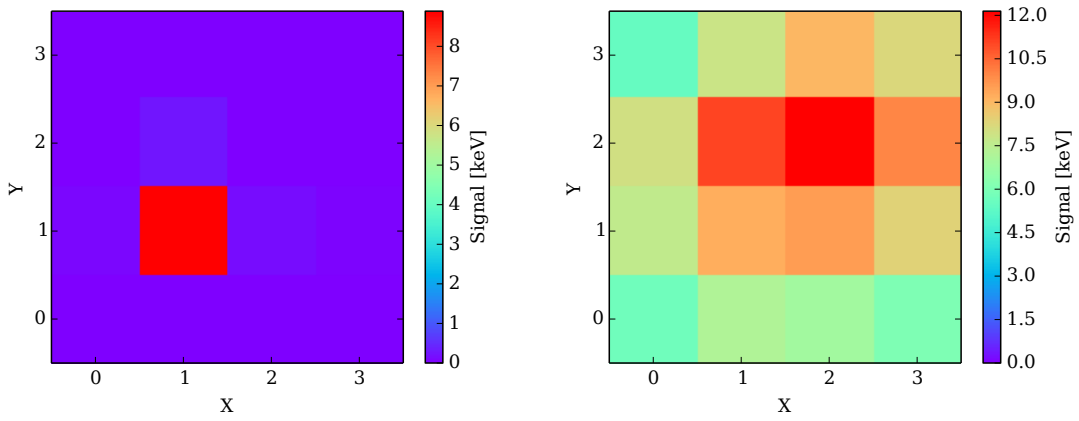

Figure 6.6: Left: Equivalent energy distribution over the 16 pixels during the measurement `P05_W81_Q10_160425_02`. In the case of this measurement, almost the whole radiation is concentrated inside pixel 05. **Right**: The equivalent energy distribution for the measurement `P05_W81_Q10_160426_05`. It can be seen that the whole sensor area is illuminated by the laser.

period in which the row is selected for read-out. Again, an energy dependence of the rise at the end of the clear time interval can be observed, which seems to be weaker than in the in-focus measurements. This time dependence will be analysed in detail in Sect. 6.4.

Figure 6.6 shows the equivalent energy deposition as a spatial distribution over the 4×4 pixels of the sensor for the measurements `P05_W81_Q10_160425_02` (in-focus, see Table 6.1) and `P05_W81_Q10_160426_05` (out-of-focus). The unit of eV is meaningless in this context, but it serves as a measure of the number of photons which have been detected in the individual pixels. Its purpose here is to correct for differences in gain between the pixels. As expected, nearly all photons have been detected in pixel 05 for the in-focus measurement. The out-of-focus measurement shows a more diverse picture, the equivalent energy deposition ranges from approximately 5 keV to 12 keV. For a more even distribution the distance from the optics to the sensor would have to be increased. This was not possible because the Z-motor has already been at its upper stop. During the measurements performed during the same day, the position of the laser optics has not been altered, and the analysis shows no significant changes in the illumination pattern.

The principal function of the DEPFET and its impact on the measured signal during the read-out have already been discussed. With the sweep measurements and the extracted peak positions the simple models can now be tested and refined. The analysis of the signal rise at the end of the clear time is described in the next section for sensor *P05_W81_Q10*. The analysis for sensor *P05_WS80_Q10* is described in Sect. 6.5.

6.4.1 Analysis of the Clear Time Constant

In the lack of theoretical models, two simple functions have been included in the DEPFET-specific code of SIXTE to describe the behaviour of the measured signal S. The first, a simple linear transition from 0% to 100% ranging over the whole clear time interval, is

Table 6.4: Best-fit parameters for simultaneous fits of exponential functions to the end of the clear time interval for the sensor *P05_W81_Q10*.

In-focus		Out-of-focus	
Parameter	Value	Parameter	Value
t_c	8577.6 ± 0.1 ns	t_c	8592.7 ± 0.3 ns
τ(8.9 keV)	65.4 ± 0.3 ns	τ(9.3 keV)	72.8 ± 0.5 ns
τ(6.4 keV)	78.0 ± 0.1 ns	τ(5.9 keV)	78.7 ± 1.0 ns
τ(4.7 keV)	80.7 ± 0.1 ns	τ(3.2 keV)	84.4 ± 0.9 ns
τ(3.3 keV)	81.2 ± 0.4 ns	τ(2.2 keV)	87.1 ± 0.8 ns
τ(2.2 keV)	91.4 ± 0.1 ns	τ(1.5 keV)	89.8 ± 0.7 ns
τ(0.7 keV)	104.4 ± 0.2 ns	τ(1.1 keV)	93.5 ± 1.5 ns

obviously unphysical, but has been used to get a first idea on the possible effects of the clear on the spectra of astrophysical sources. The second model is an exponential rise, as described by Eq. 6.3.

$$S(t) = \begin{cases} S \cdot e^{(t-t_c)/\tau} & , \; t < t_c \\ S & , \; t \geq t_c \end{cases} \tag{6.3}$$

Here, t_c is the time at which the clear is turned off, and τ is a time constant which depends on the individual sensor and its operating parameters.

As has been noted in Sect. 6.3.4, the data sets from both sensors show that the transition function is dependent on the equivalent energy of the laser pulses. This can be modelled by adding an energy dependence to the parameter $\tau = \tau(E)$. With this extension, the model can be fitted to the data. The fit is performed simultaneously to the data sets of the in-focus measurements, followed by a fit to the out-of-focus data.

Panel (b) in Fig. 6.7 shows the resulting residuals for sensor *P05_W81_Q10*. The reduced χ^2-value is relatively high with 57.22 for the in-focus data and 8.48 for the out-of-focus data, with 503 degrees of freedom each. Table 6.4 lists the best-fit parameters for the in-focus and out-of-focus measurements. The time constant increases with decreasing equivalent energy in both cases, from around 70 ns at an energy of approximately 9 keV to 100 ns at low energies of around 1 keV. This is illustrated in Fig. 6.8. However, the high χ^2_{red}-values and the residuals in the fits as shown in Fig. 6.7 indicate that the model describes the rapid increase not well enough. A second look on Fig. 6.5 shows that the energy dependence seems to be limited to a part of the rising edge. As the signal reaches about half of the full signal height, all curves in the measured regime behave similar and are almost perfectly overlapping. Only before this point the curves fan out with individual time constants. This leads to a further modification of the model. Instead of using one smooth exponential function for the whole rising edge, a break is introduced at the time $t_c - t_{break}$. Before this break, the rise is modelled by an exponential function with an energy dependence, $\tau_1(E)$. After the break, the increasing signal is described by another exponential function with a constant time constant τ_2. The amplitudes of the two exponentials are chosen such that the two parts are continuous at $t_c - t_{break}$ and reach the full signal S at the end of the clear interval, t_c.

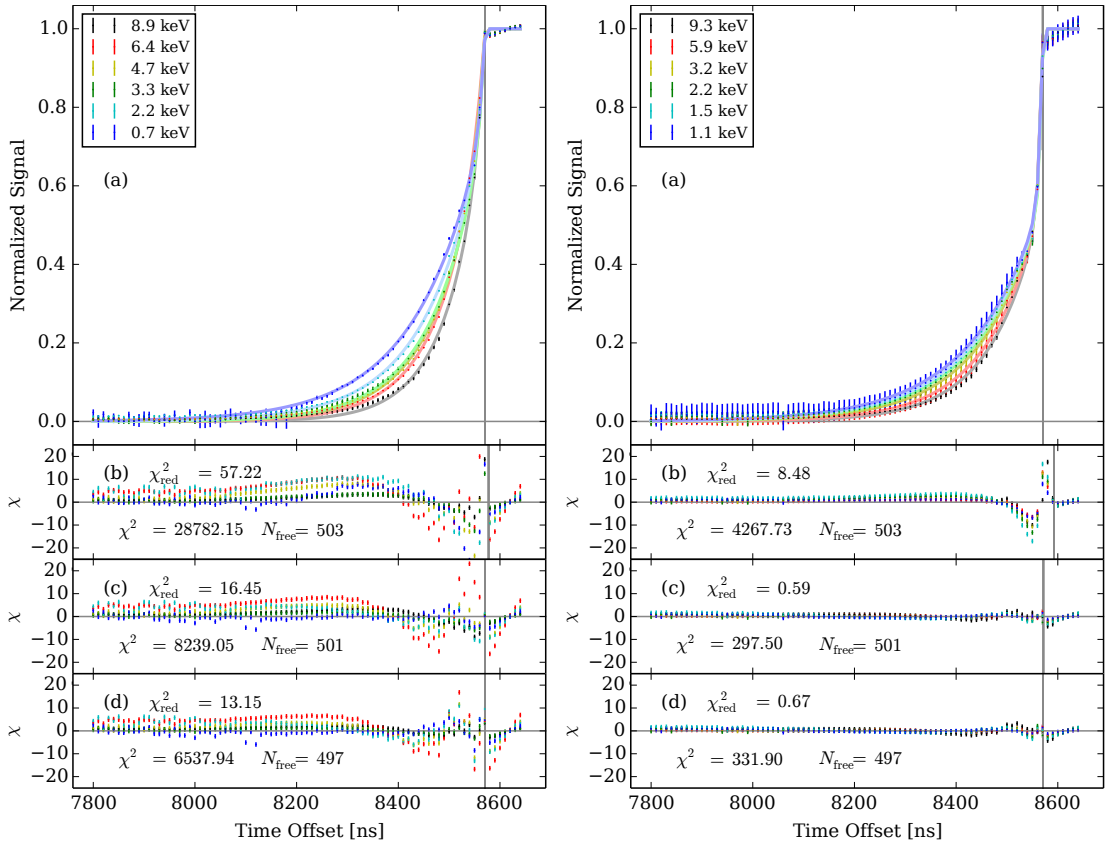

Figure 6.7: The results of fits of different functions to the rising edge of the signal curve of sensor *P05_W81_Q10* at the end of the clear time interval. In the panel on the **left**, the data of the in-focus measurements are shown as markers for six different signal heights. Panel (a) depicts the best-fit curves for the additive exponential model. The solid lines are the respective best-fit curves. Panel (b) shows the residuals of the best-fit for the simple exponential model. Panel (c) shows the same for the broken exponential model. The residuals of the additive model are shown in panel (d). The vertical gray, solid lines marks the best-fit value for the end of the clear time interval of each model. The panel on the **right** depicts the same for the out-of-focus measurements.

The resulting empirical model is described by Eq. 6.4.

$$S(t) = \begin{cases} S \cdot \mathrm{e}^{(t_{\mathrm{break}}/\tau_1(E)) - (t_{\mathrm{break}}/\tau_2)} \cdot \mathrm{e}^{(t-t_{\mathrm{c}})/\tau_1(E)} & , \; t < t_{\mathrm{c}} - t_{\mathrm{break}} \\ S \cdot \mathrm{e}^{(t-t_{\mathrm{c}})/\tau_2} & , \; t_{\mathrm{c}} - t_{\mathrm{break}} < t < t_{\mathrm{c}} \\ S & , \; t \geq t_{\mathrm{c}} \end{cases} \tag{6.4}$$

It has to be noted that the model still assumes a constant signal height right after the clear is switched off. As the data show, this is not fully true due to several effects. The highly attractive potential of the clear is not shut down instantaneously but falls with a certain time constant, caused by the finite slope of the controlling square wave. Even if the potential reacted very fast, the transition would not be a sharp edge, as it would require an instantaneous removal of the charge inside the pixel. However, the charge is generated in a three-dimensional cloud which also deforms rapidly due to the high

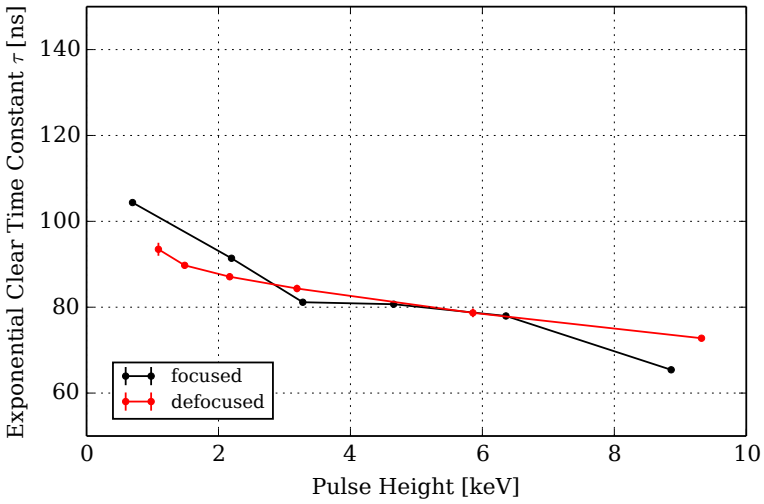

Figure 6.8: The time constant τ of the exponential functions for sensor *P05_W81_Q10* as a function of the equivalent energy. The black curve depicts the fit values obtained for the in-focus data, the red curve for the out-of-focus measurements.

Table 6.5: Best-fit parameters for simultaneous fits of broken exponential functions to the end of the clear time interval for the sensor *P05_W81_Q10*.

In-focus		Out-of-focus	
Parameter	Value	Parameter	Value
t_c	8570.63 ± 0.05 ns	t_c	8571.7 ± 0.2 ns
t_{break}	20.8 ± 0.2 ns	t_{break}	15.7 ± 0.4 ns
τ_1(8.9 keV)	65.1 ± 0.4 ns	τ_1(9.3 keV)	92.0 ± 1.0 ns
τ_1(6.4 keV)	82.0 ± 0.1 ns	τ_1(5.9 keV)	102.3 ± 2.2 ns
τ_1(4.7 keV)	87.7 ± 0.2 ns	τ_1(3.2 keV)	116.5 ± 1.9 ns
τ_1(3.3 keV)	90.8 ± 0.6 ns	τ_1(2.2 keV)	124.5 ± 1.8 ns
τ_1(2.2 keV)	105.6 ± 0.2 ns	τ_1(1.5 keV)	130.5 ± 1.5 ns
τ_1(0.7 keV)	126.6 ± 0.4 ns	τ_1(1.1 keV)	138.1 ± 3.5 ns
τ_2	51.3 ± 0.2 ns	τ_2	22.9 ± 0.5 ns

potential gradient. For the removal of the charge, this cloud needs to travel to the clear completely, and because it has a finite size, it smears out any sharp time dependencies. But due to the lack of model with theoretical foundations and the focus lying on the effective time constants of the clear itself, the transition is modelled as a sharp edge. To keep the resulting systematic error small, only seven data points after the fast rise are included in the fits, just enough to reliably find t_c.

Table 6.5 shows the best-fit parameters for the broken exponential functions fitted to the in-focus and out-of-focus data. Compared to the time constants for the simple exponential model, the values for τ_1 are larger, especially for low equivalent energies and the out-of-focus data sets, where a value of almost 140 ns is found. This is accompanied by a short second time constant of around 51 ns in the in-focus case and 23 ns in the out-of-focus case. The broken exponential model fits the data better, as the reduced χ^2-values of 16.45 (in-focus) and 0.59 (out-of-focus) show. This can also be seen directly in Fig. 6.7c.

Figure 6.9 shows the energy evolution of the first time constant for both focus settings.

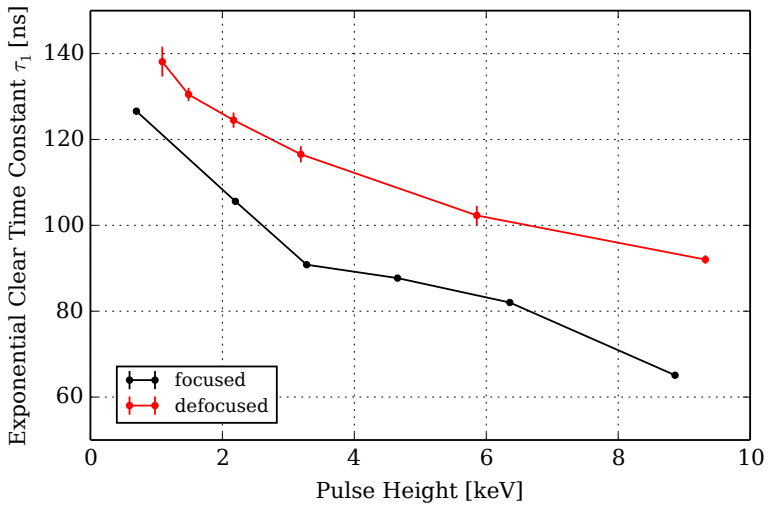

Figure 6.9: Time constant τ_1 of the broken exponential functions for sensor *P05_W81_Q10* as a function of the equivalent energy. As in Fig. 6.8, the black curve depicts the fit values obtained for the in-focus data, the red curve for the out-of-focus measurements.

As can be seen, there are two dependencies. As before, the time constant decreases with increasing equivalent energy. However, the introduction of the second time constant and the resulting improved fit shows that the first, long time constant depends on the focus setting. The in-focus values are systematically lower than the out-of-focus values. This behaviour can be explained qualitatively as a result of the charge being produced near the clear in the in-focus case, but being distributed over the whole area of the pixel in the out-of-focus case. This difference results in a longer mean distance which the charge has to move until it reaches the clear. This effect is countered by the shorter second time constant in the case of the out-of-focus data, which removes the remaining charge after the break more quickly.

The broken exponential model fits the data well. However, the forced break implies that physical processes change abruptly at a certain time during the end of the clear, with instant influence on the measured signal. This is unlikely because of the finite speed with which the electric fields change inside the volume of the pixel and the non-negligible size of the charge cloud. A more physically motivated model is the superposition of two processes with different time constants, described by the addition of two exponential functions:

$$S(t) = \begin{cases} S \cdot \left(m \cdot \mathrm{e}^{(t-t_\mathrm{c})/\tau_1} + (1-m) \cdot \mathrm{e}^{(t-t_\mathrm{c})/\tau_2} \right) & , \; t < t_\mathrm{c} \\ S & , \; t \geq t_\mathrm{c} \end{cases} \tag{6.5}$$

Here, m is the mixing factor which represents the weight of the first process relative to the full signal height. This model can be used to fit the data, but due to the interconnection between the two processes, the two time constants can not be treated separately any more. A longer first time constant also influences the time domain which was previously described only by the second time constant. This implies that both time constants need to be varied with the equivalent energy with this model.

Figure 6.7 shows the best-fit curves and the respective residuals of this additive model for the data of sensor *P05_W81_Q10*. The residuals are smaller compared to the ones for the broken exponential functions, especially for the in-focus data. Table 6.6 lists the best-fit

Table 6.6: Best-fit parameters for simultaneous fits of additive exponential functions to the end of the clear time interval for the sensor *P05_W81_Q10*.

In-focus			Out-of-focus		
E [keV]	τ_1 [ns]	τ_2 [ns]	E [keV]	τ_1 [ns]	τ_2 [ns]
8.9	74.3 ± 0.4	14.4 ± 0.6	9.3	95.3 ± 1.0	7.2 ± 0.4
6.4	87.0 ± 0.2	26.3 ± 0.3	5.9	104.2 ± 2.1	6.7 ± 0.7
4.7	93.8 ± 0.2	17.5 ± 0.3	3.2	116.9 ± 1.8	6.1 ± 0.5
3.3	97.1 ± 0.6	10.1 ± 0.6	2.2	123.9 ± 1.7	5.3 ± 0.5
2.2	110.2 ± 0.3	11.2 ± 0.2	1.5	129.1 ± 1.5	5.8 ± 0.4
0.7	128.8 ± 0.5	9.6 ± 0.3	1.1	135.9 ± 3.2	6.2 ± 0.9
	t_c [ns]	m		t_c [ns]	m
	8571.0	0.773 ± 0.003		8571.0	0.571 ± 0.004

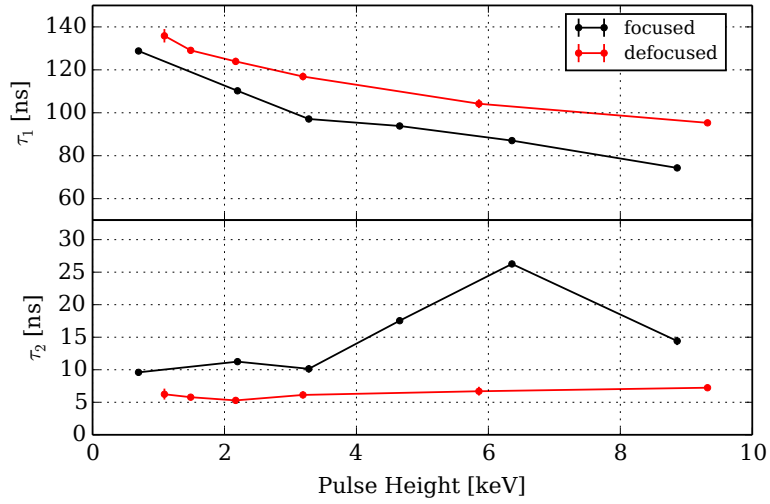

Figure 6.10: The varying time constants τ_1 and τ_2 of the additive exponential functions for sensor *P05_W81_Q10* as a function of the equivalent energy. As before, the black curves depict the fit values obtained for the in-focus data, the red curves for the out-of-focus measurements.

values for the fit parameters. Compared to the results of the broken exponential model, the values obtained for τ_1 are very similar, but τ_2 is noticeable shorter in all cases. The energy dependence of the two time constants is illustrated in Fig. 6.10. The long time constant shows the same behaviour as before. τ_2 is more or less constant in the out-of-focus case but shows an increase at intermediate equivalent energies. This may be an effect of the fast rise of the signal after the previously identified break, which is sampled poorly with a data point spacing of only 10 ns. As the best-fit values for τ_2 are in the same order between 5 ns and 25 ns, the values for τ_2 should be taken very carefully by not interpreting them too much. In fact, they depend very much on the value of t_c. For the fits presented here, t_c was frozen to a value of 8571, which has been taken from the broken exponential fit results. Otherwise, t_c would run towards the unphysical value of 8560 during the fit at the cost of infinitely small values for τ_2, taking advantage of the break in the definition of $S(t)$ at $t \geq t_c$. This could be improved in future measurements by sampling the rising edge with more data points.

The correlation between the time constants τ_1 and τ_2 for a certain energy in this model is

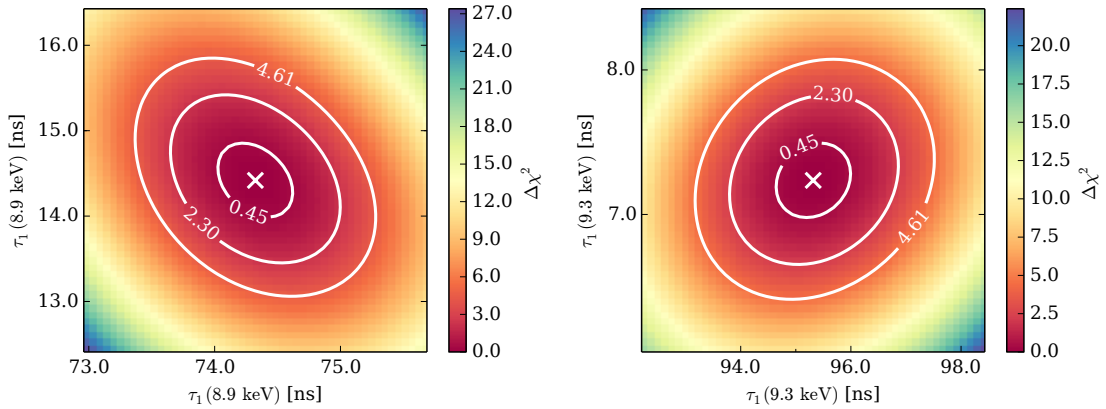

Figure 6.11: Exemplary two-dimensional χ^2-maps for the time constants τ_1 and τ_2. The white contours give the two-dimensional confidence regions of $\Delta\chi^2 = 0.45$ (0.25σ), $\Delta\chi^2 = 2.3$ (1σ) and $\Delta\chi^2 = 4.61$ (1.6σ) as described by Lampton et al. (1976). The white crosses depict the best-fit parameter combination. **Left**: χ^2-map for the focussed case at an equivalent energy of 8.9 keV. **Right**: χ^2-map for the defocussed case at an equivalent energy of 9.3 keV. Both cases exhibit a weak correlation between the two time constants.

weak, as the exemplary confidence maps in Fig. 6.11 show. This is a result of the simultaneous calculation of the best-fit parameters by using the data from several measurements at different energies at once. Due to the use of a single mixing factor m, the value of τ_1 at a given energy is not only coupled to τ_2 but also to the values of τ_1 at different energies. This multi-dimensional parameter coupling does not allow for strong correlations between two single parameters.

6.5 The Temporal Behaviour of *P05_WS80_Q10*

Overall, the data recorded for the sensor *P05_WS80_Q10* is very similar to the one for *P05_W81_Q10*. The brightness distribution for two example measurements can be seen in Fig. 6.12. As before, the laser was focussed onto pixel 05 during the in-focus measurements. The illumination pattern during the out-of-focus measurements is different to the pattern for sensor *P05_W81_Q10*, but again all pixels are illuminated. Figure 6.13 shows the signal height in pixel 05 for the in-focus data and for the out-of-focus data. Qualitatively, all features described for *P05_W81_Q10* can be found again in these plots. However, there is a minor difference: During the clear time interval, the signal peak seems not to drop completely to zero, especially for low equivalent energies. This property needs to be examined in the following analysis.

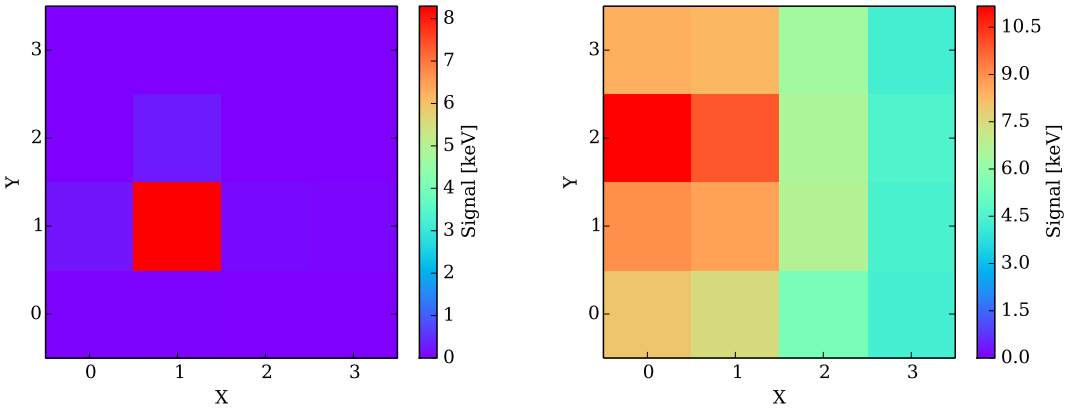

Figure 6.12: The equivalent energy distribution over the 16 pixels during the measurements `P05_WS80_Q10_160428_03` (**left**) and `P05_WS80_Q10_160429_05` (**right**) as in Fig. 6.6. The data taken on April 28 has been taken with the laser being in-focus on pixel 05. On the next day, the laser has been defocussed.

6.5.1 Asymmetry of the Noise Peak

The model which is used to explain the temporal behaviour of the DEPFET during the read-out assumes that the signal drops to zero if a photon hits the sensor when the clear is switched on. However, it has already been shown that even the high potential difference of the clear needs a certain time to remove the charge cloud from the pixel. In the case of sensor *P05_W81_Q10*, this effect causes the gradual rise at the end of the clear time which is modelled by exponential functions.

In the case of *P05_WS80_Q10*, even at the very beginning of the clear, a non-zero signal is measured, as can be seen in Fig. 6.13. This is most obvious for the lowest equivalent energies, underlining that it is a very small but systematic effect. To examine this feature in detail, a closer look needs to be taken at the noise peak of sensor *P05_WS80_Q10*. The height of the remaining signal during the time the clear is switched on is below the width of the noise peak itself. The left panel in Fig. 6.14 shows a zoomed-in view on the noise peak in the summed spectra of one measurement. It shows that the noise peak is asymmetric. Its right side is noticeably wider than the left side. Furthermore, a narrow, dip-like feature around channel 5375 can be seen. This feature is found to be at this place regardless of the peak's positions. Together with the very low width of the dip this means that the feature must be an effect from the read-out electronics, decreasing the efficiency of this channel. To quantify the asymmetry, an asymmetric Gaussian function can be fitted to the peak.

$$y(x) = \begin{cases} a \cdot \mathrm{e}^{-\frac{(x-x_\mathrm{c})^2}{2\sigma_1^2}} & , \; x < x_\mathrm{c} \\ a \cdot \mathrm{e}^{-\frac{(x-x_\mathrm{c})^2}{2\sigma_2^2}} & , \; x \geq x_\mathrm{c} \end{cases} \tag{6.6}$$

The resulting best-fit parameters are listed in Table 6.7. It shows that the right side is almost 1.5 times as wide as the left side. This asymmetry causes the peak-detection

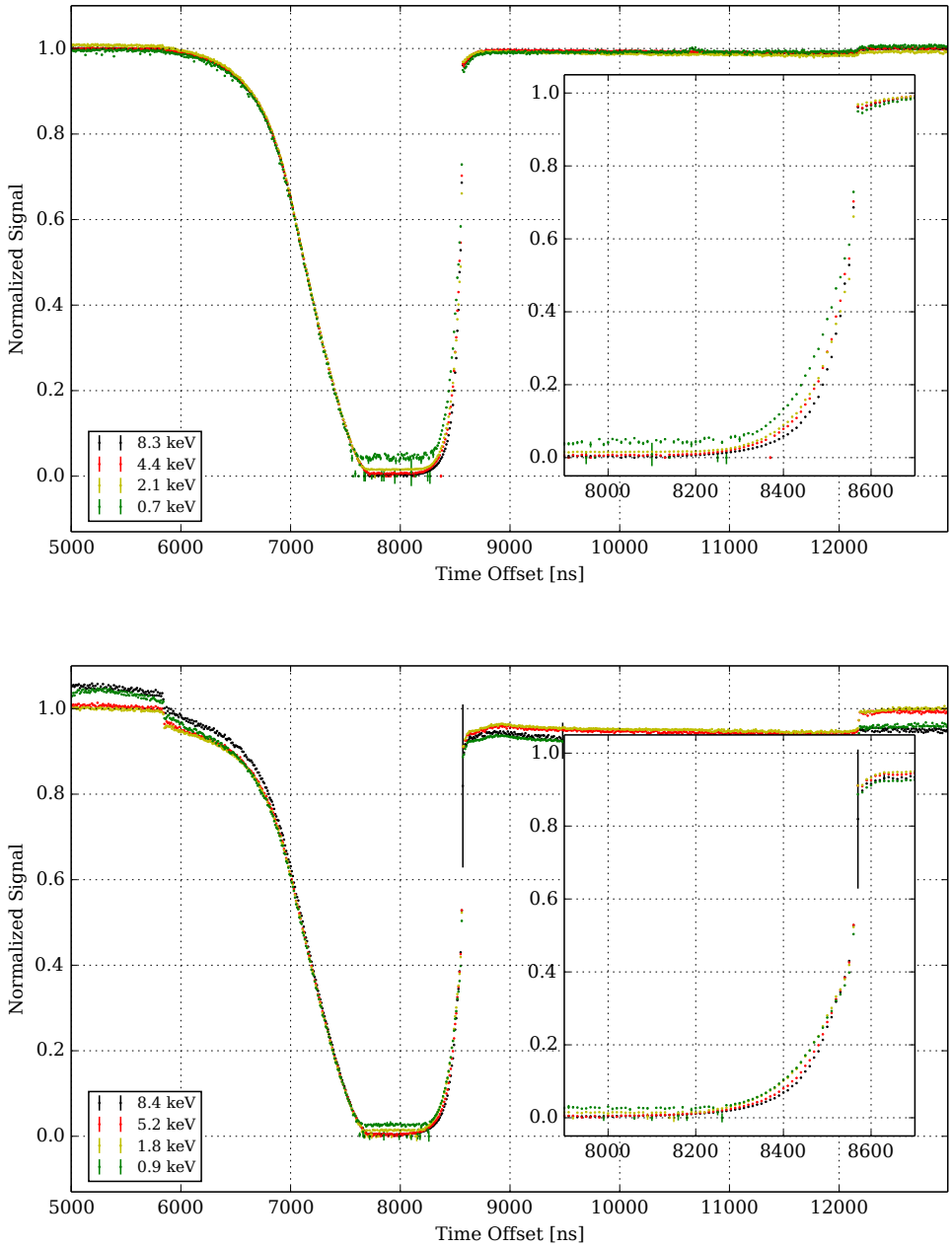

Figure 6.13: Top: The normalized reconstructed signal height of the sensor *P05_WS80_Q10* as a function of the energy deposition time during the read-out of the pixel. Like the measurements presented for the detector *P05_W81_Q10* in Fig. 6.5, the laser position is in-focus over pixel 05. **Bottom**: The normalized reconstructed signal height of the sensor *P05_WS80_Q10* as a function of the energy deposition time during the read-out of the pixel. The data represents the data for pixel 05 as before, but the laser being out-of focus, illuminating the whole pixel array.

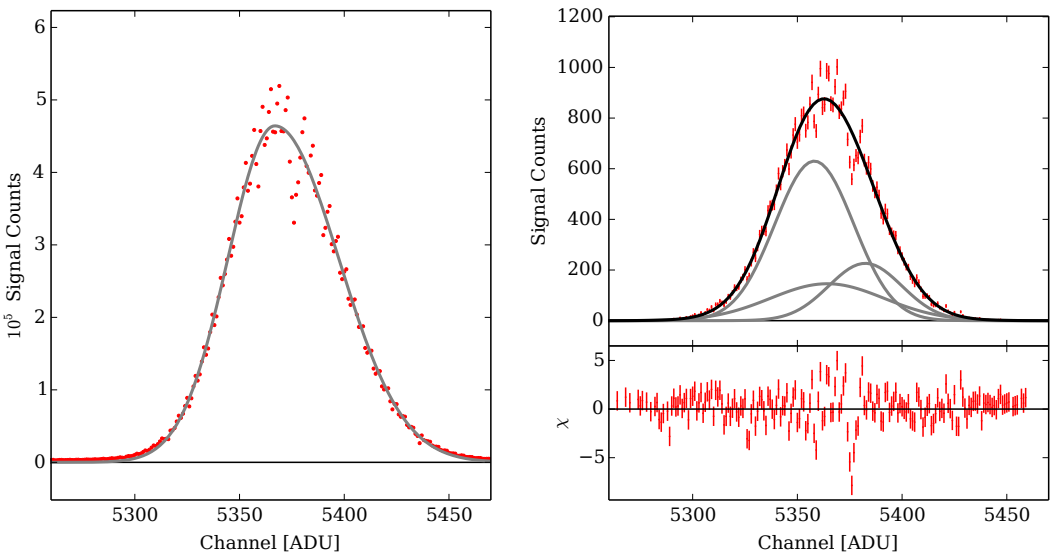

Figure 6.14: The asymmetric noise peak as measured for sensor *P05_WS80_Q10*. **Left**: The summed spectrum of the measurement `P05_WS80_Q10_160428_05` for pixel 05 around the position of the noise peak. The peak is slightly asymmetric, stretched towards the high channels. Additionally, there is a dip-like feature around the channel 5375, which is most likely caused by imperfections in the read-out electronics, as it was found to be located at the same channels even if the peak is shifted slightly. The deviation from a symmetric function can be characterised by an asymmetrical Gaussian function with the two widths $\sigma_1 = 22.4$ and $\sigma_2 = 30.5$, as the gray curve shows. The asymmetry causes the peak fitting algorithm to detect the signal peak at the bins next to the dip during the clear time interval, as the panel on the **right** shows for the spectrum at a time offset of 8020 ns. The gray lines show the individual components, the black line shows the total best-fit model.

Table 6.7: Best-fit parameters for an asymmetric Gaussian function fitted to the noise peak in the summed up spectrum of measurement `P05_W81_Q10_160428_05` for pixel 05.

Parameter	Value
x_c	5366.85 ± 0.05
$a/1000$	464.22 ± 0.11
σ_1	22.42 ± 0.04
σ_2	30.49 ± 0.04

algorithm to model the noise peak with up to three Gaussian components, as can be seen in the right panel of Fig. 6.14. A likely explanation for the asymmetry is similar to the effect which has been modelled before for the end of the clear time interval. In the case of sensor *P05_WS80_Q10*, the clear seems to be too weak to remove all charge during one read-out cycle, or the geometry of the electric field inside the pixel traps a small part of the charge, such that it is measured again in the next frame. This assumption is supported by the measured influence of the location in which the charge is produced.

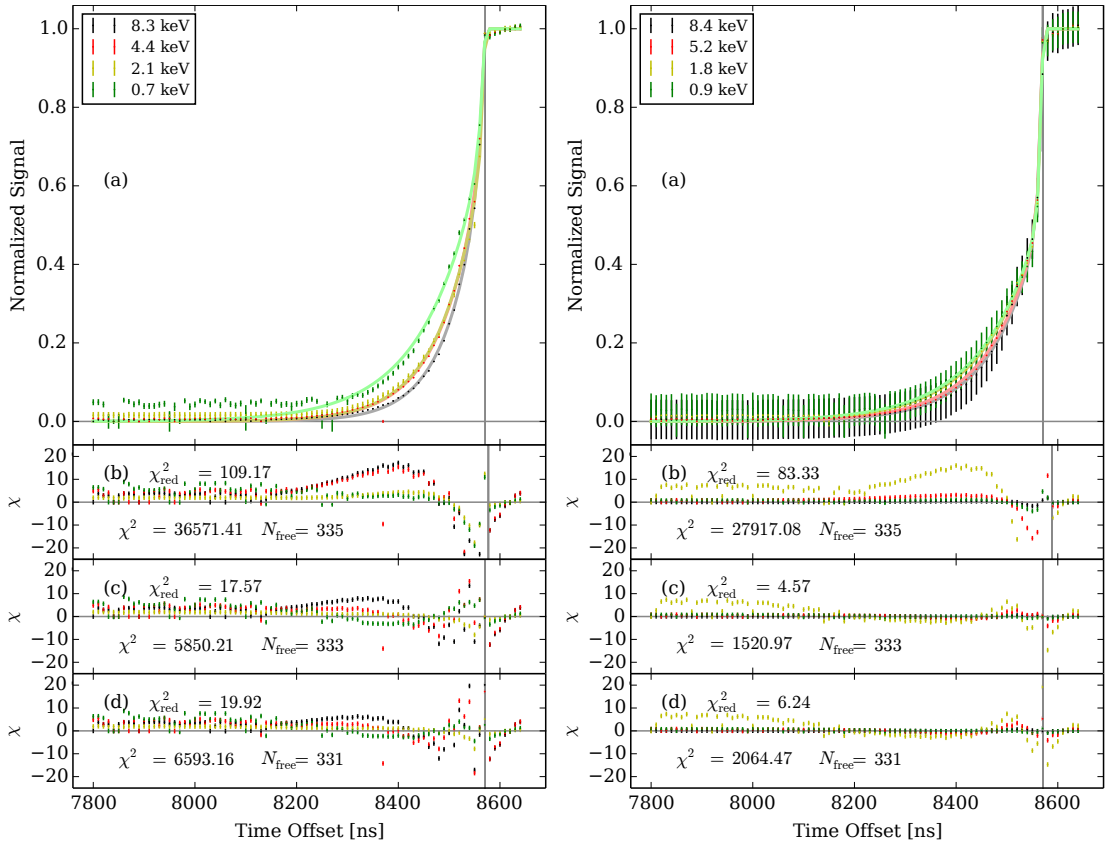

Figure 6.15: The results of fits of different functions to the rising edge of the signal curve of sensor *P05_WS80_Q10* at the end of the clear time interval. In the panel on the **left**, the data of the in-focus measurements are shown as markers for four different signal heights. Panel (a) depicts the best-fit curves for the additive exponential model. The solid lines are the respective best-fit curves. Panel (b) shows the residuals of the best-fit for the simple exponential model. Panel (c) shows the same for the broken exponential model. The residuals of the additive model are shown in panel (d). The vertical gray, solid lines marks the best-fit value for the end of the clear time interval of each model. The panel on the **right** depicts the same for the out-of-focus measurements.

6.5.2 Analysis of the Clear Time Constant

As discussed before in Sect. 6.4.1 for sensor *P05_W81_Q10*, the time constant at the end of the clear time interval is of particular interest. Using the knowledge gained for the first sensor, two models are fitted to the data. First, the simple exponential function from Eq. 6.3 is used, and fitted simultaneously to all measurements of either the in-focus or the out-of-focus data sets. The resulting best-fit parameters are given in Table 6.8, and the resulting residuals are shown in panel (b) of Fig. 6.15. The statements as for sensor *P05_W81_Q10* apply for *P05_WS80_Q10*. The residuals show a distinct, systematic deviation between the model and the data. For the fits to the *P05_WS80_Q10*-data, the reduced χ^2 is even worse than before, which is partially explained by the non-zero asymptote, as discussed in the previous section. The values of the time constants are shown as a

Table 6.8: Best-fit parameters for simultaneous fits of exponential functions to the end of the clear time interval for the sensor *P05_WS80_Q10*.

In-focus		Out-of-focus	
Parameter	Value	Parameter	Value
t_c	8577.2 ± 0.1 ns	t_c	8588.3 ± 0.1 ns
τ(8.3 keV)	55.2 ± 0.1 ns	τ(8.4 keV)	64.3 ± 2.7 ns
τ(4.4 keV)	62.8 ± 0.1 ns	τ(5.2 keV)	68.2 ± 0.4 ns
τ(2.1 keV)	61.5 ± 0.4 ns	τ(1.8 keV)	72.1 ± 0.2 ns
τ(0.7 keV)	83.2 ± 0.4 ns	τ(0.9 keV)	72.6 ± 2.3 ns

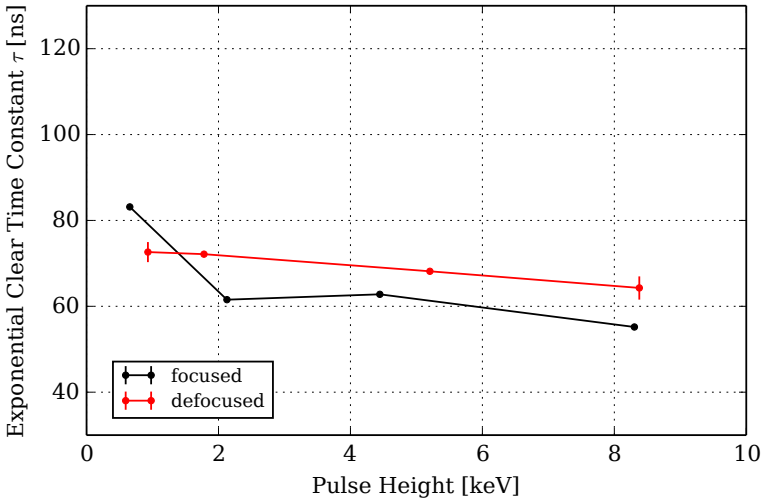

Figure 6.16: Time constant τ of the exponential functions for sensor *P05_WS80_Q10* as a function of the equivalent energy. The black curve depicts the fit values obtained for the in-focus data, the red curve for the out-of-focus measurements.

function of the equivalent energy in Fig. 6.16. Overall, with values between about 50 ns to 85 ns, they are slightly lower than the ones for sensor *P05_W81_Q10*, and the energy dependence is a bit smaller.

As the residuals of the simple exponential model show the same shape as for the previous sensor, the broken exponential model as described by Eq. 6.4 is also tested. Table 6.9 lists the best-fit parameter values for the model, and panel (c) of Fig. 6.15 illustrates the residuals. As before, the more complex model fits the data much better, with smaller residuals and lower χ^2_{red}-values. Another improvement which can also be seen for sensor *P05_W81_Q10* is the decreased difference between the fitted end of the clear time t_c for the in-focus and out-of-focus case, which is now within the parameter uncertainty. It is now nearly identical to the value obtained for sensor *P05_W81_Q10*, with approximately 8571 ns. This follows the expectation, because the sequence with which the DEPFET is controlled has been the same for both sensors and is of course independent from the laser's position. The agreement between these values is another indication that the broken exponential model is a good representation of the data, at least for the end of the clear interval.

The second time constant is much shorter in both cases, and affects the rise only for a very small time of around 15 ns, which is again a bit lower than measured for sensor

Table 6.9: Best-fit parameters for simultaneous fits of broken exponential functions to the end of the clear time interval for the sensor *P05_WS80_Q10*.

In-focus		Out-of-focus	
Parameter	Value	Parameter	Value
t_c	8570.37 ± 0.03 ns	t_c	8570.60 ± 0.04 ns
t_{break}	15.4 ± 0.1 ns	t_{break}	12.9 ± 0.1 ns
τ_1(8.3 keV)	63.5 ± 0.1 ns	τ_1(8.4 keV)	87.8 ± 6.2 ns
τ_1(4.4 keV)	76.8 ± 0.2 ns	τ_1(5.2 keV)	93.8 ± 0.9 ns
τ_1(2.1 keV)	79.0 ± 0.8 ns	τ_1(1.8 keV)	106.0 ± 0.4 ns
τ_1(0.7 keV)	114.4 ± 0.8 ns	τ_1(0.9 keV)	110.1 ± 5.7 ns
τ_2	30.3 ± 0.1 ns	τ_2	18.0 ± 0.1 ns

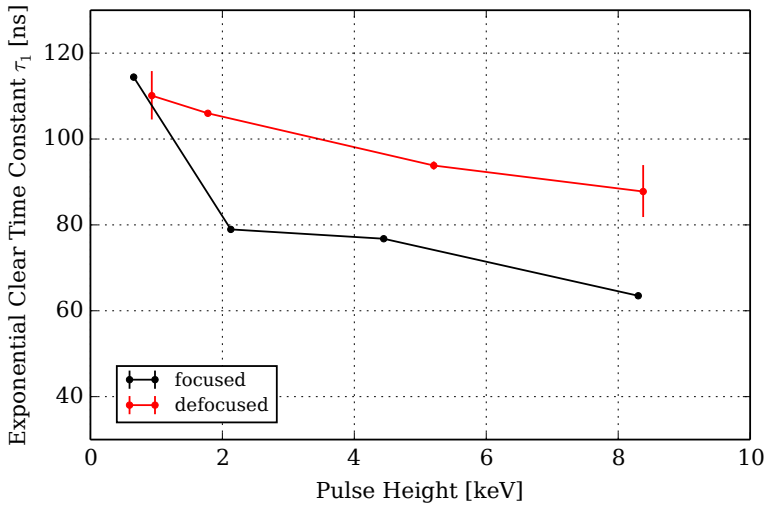

Figure 6.17: Time constant τ_1 of the broken exponential functions for sensor *P05_WS80_Q10* as a function of the equivalent energy. As in Fig. 6.16, the black curve depicts the fit values obtained for the in-focus data, the red curve for the out-of-focus measurements.

P05_W81_Q10. Figure 6.17 shows the energy dependence of the first time constant. As seen before, the varying first time constant τ_1 is significantly larger than the time constant in the simple model, reaching from over 60 ns up to almost 115 ns. Except for the data points at the lowest equivalent energy which underlie the highest influence of the non-zero baseline, the in-focus time constant is again lower than the respective out-of-focus value by around 20 ns.

As discussed for sensor *P05_W81_Q10*, the broken model is problematic for physical reasons. The additive model described by Eq. 6.5 is more reasonable, even if it still comes without a theoretical foundation for the processes inside the pixel. The sample point spacing of 10 ns for the measurements of *P05_WS80_Q10* is identical to the ones for *P05_W81_Q10*, so the value for the end of the clear time t_c is again required to be known and frozen during the fit. The value is once more set to 8571 ns as for *P05_W81_Q10*, which is justified by the results of the broken exponential fit as described before. Figure 6.15 shows the best-fit model curves for the in-focus and the out-of-focus data, Table 6.10 lists the best-fit parameter values.

For sensor *P05_WS80_Q10*, the additive model yields slightly worse statistics than the

Table 6.10: Best-fit parameters for simultaneous fits of additive exponential functions to the end of the clear time interval for the sensor *P05_WS80_Q10*.

In-focus			Out-of-focus		
E [keV]	τ_1 [ns]	τ_2 [ns]	E [keV]	τ_1 [ns]	τ_2 [ns]
8.3	66.5 ± 0.2	10.1 ± 0.1	8.4	91.3 ± 5.6	7.0 ± 2.4
4.4	77.9 ± 0.2	9.7 ± 0.2	5.2	96.6 ± 0.9	6.9 ± 0.3
2.1	78.9 ± 0.7	5.8 ± 0.4	1.8	107.4 ± 0.4	6.1 ± 0.1
0.7	108.9 ± 0.7	10.0 ± 0.5	0.9	110.8 ± 5.1	5.6 ± 1.4
	t_c [ns]	m		t_c [ns]	m
	8571.0	0.725 ± 0.004		8571.0	0.546 ± 0.003

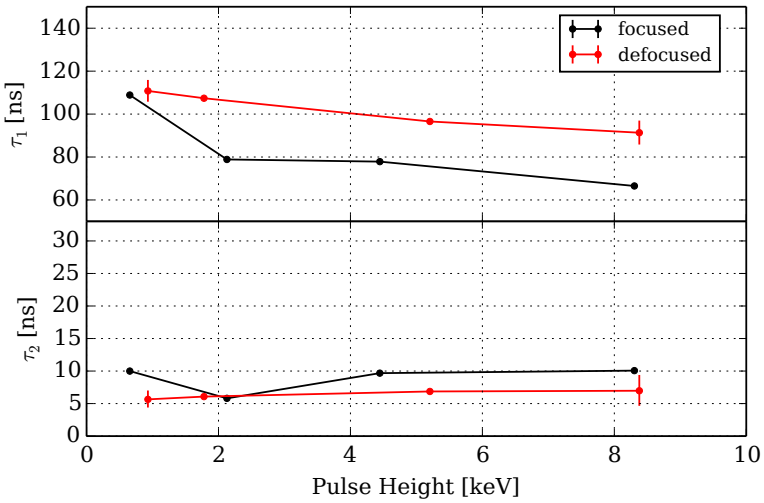

Figure 6.18: Time constants τ_1 and τ_2 of the additive exponential functions for sensor *P05_WS80_Q10* as a function of the equivalent energy. As in Fig. 6.16, the black curves depict the fit values obtained for the in-focus data, the red curves for the out-of-focus measurements.

broken model. However, the absolute parameter values for τ_1 are very similar between both models, and have the same dependence on the equivalent energy, as Fig. 6.18 shows. The second time constant is nearly identical to τ_2 found for *P05_W81_Q10*, but does not show the rise at around 6 keV for the in-focus data.

6.6 Discussion and Comparison of the two Sensors

In the last sections the two sensors *P05_W81_Q10* and *P05_WS80_Q10* have been analysed for their temporal behaviour, especially during the end of the time in which the clear removes charge from the pixel. It has been shown that a simple, exponential model is not enough to describe the processes happening to the charge during this time. Actually, the fine sampling of the sweep measurements with the SPIX II-setup showed the presence of two time constants. As the laser signal is injected more and more to the end of the clear time, the measured signal rises with a rather slow time constant of around 100 ns. During the final ten to 20 nanoseconds before the clear is turned off, the rise accelerates and jumps to an effective time constant of some 10 ns. At this transition, around one half

of the full signal is measured. This complex behaviour has been modelled with both, a broken exponential function as well as an additive model composed from two continuous exponentials. The residuals for both sensors and models are comparable.

Additionally, both sensors show the same reciprocal dependence of the long time constant on the signal's equivalent energy. It has been found that the more charge is induced, the faster it can be removed during the first phase. The origin of this behaviour is yet unclear and may be explained by detailed charge propagation simulations in the future. The dependence of the geometrical extent of the charge cloud on the clear process may play a vital role, as the different measurements for the in-focus and out-of-focus laser positions show. While the charge cloud induced by the laser should be of discrete size in the centre of the pixels for the in-focus measurements, it is a homogeneous distribution over the whole pixel array for the out-of-focus measurements. This difference has shown to have a strong impact on the clear process, as the different values for the time constants indicate. In general, the charge produced in the out-of-focus measurements is removed slower than in the in-focus case, which matches to a basic expectation from the distance between the point of production and the clear. The clear is attached to the gate of the DEPFET and is thus located near the centre, which is the area where the charge is injected in the case of the in-focus measurements. In the out-of-focus measurements, a part of the charge is also generated in the outer regions of the pixel, from which it needs to travel a longer distance to the clear, which leads to a longer delay. For the WFI on *Athena*, the out-of-focus measurements are more applicable. The pixel size of the WFI of 130 μm, which equals 2.2″ on the sky, oversamples the planned PSF of the mirror with a HEW of 5″ (below 8 keV) such that even for point sources, a larger number of pixels are illuminated over their whole surface. This resembles closely the defocussed measurements presented in this chapter.

The absolute values of the time constants are similar but not identical between the two sensors. Overall, the time constants for sensor *P05_W81_Q10* are slightly higher than for *P05_WS80_Q10*. However, it has been found that the latter sensor has a strongly asymmetric noise peak. This can be explained by an incomplete charge removal during the clear. A small amount of the charge produced during one frame is not removed by the clear, but is measured again in the next frame, before it is finally completely cleared. This effect might become important for continuum spectra ranging over one and more decades in energy. One photon could lead to a second measured event with very low energy, which could also pile up further with a photon of the next frame. This would affect the overall quality of the spectrum, which is why such partial charge removals have to be avoided for the final detector design. Sensor *P05_W81_Q10* shows that this is not a general problem of DEPFETs but can be excluded by the details of the sensor design and operation parameters.

With respect to the second purpose of the measurements, the description of the clear period for SIXTE, much has been learned. The fits presented in the previous sections show that overall, the exponential model as newly implemented in the software is a good first-order approximation of the real sensor's behaviour. The detailed differences of this model to the behaviour as measured for the two prototype sensors are small compared to the intrinsic dependencies on the equivalent energy and the geometrical distribution

of the charge. However, these dependencies vary between the two sensors examined in the course of this work. They will be even more different to the final sensor for the WFI, as the pixel size will be different and the read-out sequence will likely be optimized. This means that the real outcome of the examination for SIXTE is the discovery of the dependencies, but not the exact numbers. But with the help of this early analysis, the effects can be tracked as the detector development goes on and finally implemented in SIXTE.

Another effect yet to be described is the exact shape of the time dependence during the integration times. As discussed in Sect. 3.2.3, the expectation is a linear fall-of due to the constant integration factor over the time. However, the data measured for the two sensors consistently show a rather smooth transition. The smoothness is caused by the charge produced during the integration time being collected in the internal gate with a finite speed. This means that even after the time of the charge induction, it takes a small amount of time until the full charge is integrated. Until then, the integration measures only a part of the charge, and thus the curve measured during the integration period is below the expected one. The data presented for the two sensors show no energy dependence of this effect, but due to the complex shape, an appropriate parametrisation is still lacking. The effect caused by this process may be more important than the clear, as in the beginning of the first integration, the difference of E_{m} to E_{photon} is small, so it will cause an effective widening of the main peak in the sensors response to lower energies, which is equivalent to a slightly lower energy resolution. This will need to be addressed in the future to build a consistent model of the effective RMF.

7 Summary and Conclusions

When launched in 2028, the *Athena* X-ray mission will revolutionise our understanding of the cosmos. In the past decades our view on the universe has been extended to previously unobserved wavelengths and distances, bringing light into the development of the universe and the structures within.

Athena's Science Theme, the Hot and Energetic Universe, is meant to start where our current understanding ends. It will bring new information on the evolution of the large-scale structures which will improve the cosmological models developed in the last years. It will also refine our picture from the most energetic processes in the universe, the mass accretion on supermassive black holes in the centres of AGN. These objects with their extreme physical properties are not only interesting by themselves but are believed to have a strong influence on the development on the objects in the surrounding space due to feedback processes. As has been presented in Chapter 1, the science theme is structured in a multitude of science goals, all of which are designed to give us a better understanding of the evolution of our universe.

The *Athena* spacecraft as planned today and presented in Chapter 2 features a large effective area with good angular resolution and two highly capable instruments. The WFI provides a large field of view as well as the ability to observe bright sources up to 1 Crab and above with nearly unaffected spectral quality. The X-IFU extends the mission's capability to an unprecedented spectral resolution of 2.5 eV. This observatory is designed to answer the questions raised by the science goals, such that we can expect a better understanding of the cosmos at the end of the mission.

The performance required to give us the needed data is gained by using sensors with new technology. Both instruments on board the spacecraft rely on new sensor concepts. The WFI consists of a total of five DEPFET-sensors which enable an energy resolution better than a comparable CCD because of the direct, pixel-internal amplification of the charge produced in the pixel material instead of transporting it to the read-out electronics first. The possibility to address individual pixels also helps to increase the read-out speed, which results in the high count-rate capability of the sensor. The X-IFU further

improves the energy resolution by using an entirely different measurement concept. The TES-technology builds upon the transition from superconducting to normal material at very low energies. At temperatures around this transition, a strong increase in the sensor's resistivity can be observed and measured by elaborate read-out electronics. This effect can be used in X-ray detectors as each photon interacting with the sensor dumps energy into the material which heats the absorber. The technology has proven its capabilities already on board *Hitomi* (Hitomi Collaboration, et al., 2016). Both of the detector concepts have been described in more detail in Chapter 3. The work presented in this thesis is the result of detector simulations performed with SIXTE. This simulation software package has been developed mostly for CCD sensors, so some work has been invested to implement the detector effects of DEPFETs and TESs. The properties of these effects and their implementation have also been described in Chapter 3.

The progressing design of the spacecraft and its instruments requires to regularly test if the science goals can be achieved, otherwise design parameters need to be changed. Such a test has been performed for the science goal of detecting WHIM filaments. WHIM filaments consist of hot plasma with temperatures between $10^5 - 10^7$ K. Due to their low emission, they are best traced by their absorption lines in the spectra of bright background sources. The *Athena* Mission Proposal requires the detection of such lines in the spectra of GRB afterglows as well as of AGN. In Chapter 4 simulations have been performed to specifically address the observatory's ability to detect such lines in the line of sight of GRB afterglows. To test this ability, a simple model has been set up for the filament's absorption spectrum and a large number of observations with the X-IFU have been performed and analysed with a blind-line search. It has been shown that under favourable observational circumstances which allow for the longest possible exposure time of about 100 ks, WHIM filaments with intermediate absorption strength can be detected to a limit of 3×10^{-11} erg cm^{-2} s^{-1} for the starting flux of the afterglow.

Another routinely performed test has been presented in Chapter 5. The bright source performance study tests the instrument's capability to observe sources with high fluxes, resulting in high count rates on the detector. As has been described, high count rates can get problematic as the event pattern generated on the detector can not be reconstructed unambiguously. The pattern reconstruction software needs to assume certain conditions which leads to either a strong drop in throughput or a increasing confusion of the photon's energy caused by pile-up. Both of these effects decrease the instrument's performance. A drop in throughput effectively blinds the detector for bright sources. The misreconstruction of the photon's energy leads to a distortion of the measured energy spectrum, which may cause a misinterpretation of the data. The simulations performed for the WFI show that the large chip in a 16-row window mode can perform observations of sources with a brightness of approximately 20 mCrab. For higher fluxes, the pile-up rises above the 1% limit and the throughput drops considerably. The simulations also show that defocussing helps to distribute the high number of photons over a larger number of pixels, reducing the probability of pile-up. Using the large detector in a 64-row window mode, defocussing increases the bright source capability of approximately one order in magnitude of the source flux. This effect is used to optimise the position of the WFI's small sensor. The simulations lead to the conclusion that an out-of-focus position

of 35 mm above the focal plane is the optimum for the current configuration. Mounted in this position, the WFI can observe sources with a brightness of around 10 Crab. This position for the small sensor has already been adopted in the baseline configuration of the instrument.

To further refine the simulation algorithms, measurements of real prototype detectors for the WFI have been performed at the MPE. Two relatively similar 4×4-DEPFET matrices have been examined for their response during the read-out. Photons hitting a pixel during its active time during the read-out may cause energy misfits, which are events with falsely reconstructed energies. If not calibrated properly, such events lead to a deformation of the measured energy spectrum similar to pile-up. To the date of the measurements, the details of the energy response of DEPFET sensors during the read-out have not been covered. Using an optical laser to inject energy into the pixels which in turn generates a charge cloud at clearly defined times, the time-dependent response of two DEPFET sensors during the clear process have been measured. Chapter 6 describes these measurements and the analysis of the data in detail. Both sensors show a similar behaviour. The time dependence of the measured signal during the clear follows a broken or additive exponential rise with energy dependent time constants. In first order, this can also be modelled by a simple exponential function. In future simulations, this and other details of the detectors need to be implemented to increase the simulation's realism. With this kind of continuous interaction between simulations and hardware development, the quality of the observatory will reach a very high standard and promises to answer the questions raised by the Science Theme.

Bibliography

Agostinelli S., Allison J., Amako K., et al., 2003, Nuclear Instruments and Methods in Physics Research Section A: Accelerators, Spectrometers, Detectors and Associated Equipment, 506, 250

Aird J., Comastri A., Brusa M., et al., 2013, ArXiv e-prints, 1306.2325

Alam S., Ata M., Bailey S., et al., 2016, ArXiv e-prints, 1607.03155

Allison J., Amako K., Apostolakis J., et al., 2006, IEEE Transactions on Nuclear Science, 53, 270

Angulo R.E., Springel V., White S.D.M., et al., 2012, MNRAS, 426, 2046

Arnaud K.A., 1996, In: Jacoby G.H., Barnes J. (eds.) Astronomical Data Analysis Software and Systems V, Astronomical Society of the Pacific Conference Series, 101, 17

Ayre M., Bavdaz M., Ferreira I., et al., 2016, In: den Herder J.W.A., Takahashi T., Bautz M. (eds.) Space Telescopes and Instrumentation 2016: Ultraviolet to Gamma Ray, Proc. SPIE, 9905, 990526

Bähr A., 2010, Diplomarbeit, Hochschule für angewandte Wissenschaften-FH München

Barret D., 2016, Modification of the baseline for the pixel configuration of the TES array, Technical Report XIFU-MG-MAN-004-IRAP, IRAP

Barret D., Bautz M., Bookbinder J., et al., 2011, IXO: Revealing the physics of the hot Universe, `http://sci.esa.int/science-e/www/object/doc.cfm?fobjectid=48361`

Barret D., Lam Trong T., den Herder J.W., et al., 2016, In: den Herder J.W.A., Takahashi T., Bautz M. (eds.) Space Telescopes and Instrumentation 2016: Ultraviolet to Gamma Ray, Proc. SPIE, 9905, 99052F

Barthelmy S.D., Barbier L.M., Cummings J.R., et al., 2005, Space Sci. Rev., 120, 143

Berti E., Volonteri M., 2008, ApJ, 684, 822

Borm K., Reiprich T.H., Mohammed I., Lovisari L., 2014, A&A, 567, A65

Boylan-Kolchin M., Springel V., White S.D.M., et al., 2009, MNRAS, 398, 1150

Branchini E., Ursino E., Corsi A., et al., 2009, ApJ, 697, 328

Brand T., 2011, Bachelorarbeit, Friedrich-Alexander-Universität Erlangen-Nürnberg

Brand T., Dauser T., Peille P., Wilms J., 2016a, SIXTE MANUAL - Description of the SIXTE simulator, Technical Report SIXTE-MANUAL (v1.1), ECAP

Brand T., Dauser T., Wilms 2016b, Athena X-IFU WHIM simulations, Technical Report ECAP-XIFU-WHIM-3, ECAP

Brand T., Dauser T., Wilms J., Willingale R., 2015, Impact of defocusing on the Athena WFI, Technical Report WFI-ECAP-DEFOC-20150727, ECAP

Brand T., Wilms J., Dauser T., et al., 2016, In: den Herder J.W.A., Takahashi T., Bautz M. (eds.) Space Telescopes and Instrumentation 2016: Ultraviolet to Gamma Ray, Proc. SPIE, 9905, 99055F

Cappi M., Done C., Behar E., et al., 2013, ArXiv e-prints, 1306.2330

Ceballos M.T., Cobo B., Peille P., et al., 2015, In: Ehle M. (ed.) Exploring the Hot and Energetic Universe: The first scientific conference dedicated to the Athena X-ray observatory, 69

Cen R., Ostriker J.P., 2006, ApJ, 650, 560

Charles I., Daniel C., André J., et al., 2016, In: den Herder J.W.A., Takahashi T., Bautz M. (eds.) Space Telescopes and Instrumentation 2016: Ultraviolet to Gamma Ray, Proc. SPIE, 9905, 99052J

Chertok B., Siddiqi A., 2005, Rockets and People, Vol. Bd. 1 of *NASA SP*, NASA SP, Bd. 1, US National Aeronautics and Space Admin

Churazov E., Sunyaev R., Isern J., et al., 2014, Nature, 512, 406

Collon M.J., Vacanti G., Günther R., et al., 2016, In: den Herder J.W.A., Takahashi T., Bautz M. (eds.) Space Telescopes and Instrumentation 2016: Ultraviolet to Gamma Ray, Proc. SPIE, 9905, 990528

Croston J.H., Sanders J.S., Heinz S., et al., 2013, ArXiv e-prints, 1306.2323

Dauser T., Brand T., Wilms J., 2015, Bright Source Performance of the Athena WFI, Technical Report WFI-BSR-04, ECAP

Dauser T., García J., Wilms J., 2016, Astronomische Nachrichten, 337, 362

Davis J.E., Bautz M.W., Dewey D., et al., 2012, In: Takahashi T., Murray S.S., den Herder J.W.A. (eds.) Space Telescopes and Instrumentation 2012: Ultraviolet to Gamma Ray, Proc. SPIE, 8443, 84431A

De Marco B., Ponti G., Miniutti G., et al., 2013, MNRAS, 436, 3782

Decourchelle A., Costantini E., Badenes C., et al., 2013, ArXiv e-prints, 1306.2335

den Hartog R., Peille P., Dauser T., et al., 2016, In: den Herder J.W.A., Takahashi T., Bautz M. (eds.) Space Telescopes and Instrumentation 2016: Ultraviolet to Gamma Ray, Proc. SPIE, 9905, 99055T

Dennerl K., Burkert W., Burwitz V., et al., 2012, In: Takahashi T., Murray S.S., den Herder J.W.A. (eds.) Space Telescopes and Instrumentation 2012: Ultraviolet to Gamma Ray, Proc. SPIE, 8443, 844350

Dornberger W., 1952, V2 - der Schuss ins Weltall: Geschichte einer grossen Erfindung, Bechtle Verlag

Dovciak M., Matt G., Bianchi S., et al., 2013, ArXiv e-prints, 1306.2331

Eggert T., Boslau O., Kemmer J., et al., 2006, Nuclear Instruments and Methods in Physics Research A, 568, 1

Einstein A., 1905, Annalen der Physik, 322, 891

Emmanoulopoulos D., McHardy I.M., Papadakis I.E., 2011, MNRAS, 416, L94

Ettori S., Pratt G.W., de Plaa J., et al., 2013, ArXiv e-prints, 1306.2322

Evans P.A., Beardmore A.P., Page K.L., et al., 2009, MNRAS, 397, 1177

Evans P.A., Beardmore A.P., Page K.L., et al., 2007, A&A, 469, 379

Fabian A.C., Zoghbi A., Ross R.R., et al., 2009, Nature, 459, 540

Fan W.C., Drumm C.R., Roeske S.B., Scrivner G.J., 1996, IEEE Transactions on Nuclear Science, 43, 2790

Fano U., 1947, Phys. Rev., 72, 26

Forman W., Jones C., Cominsky L., et al., 1978, ApJS, 38, 357

Friedman H., Lichtman S.W., Byram E.T., 1951, Physical Review, 83, 1025

Fürmetz M., Pietschner D., Meidinger N., 2016, In: den Herder J.W.A., Takahashi T., Bautz M. (eds.) Space Telescopes and Instrumentation 2016: Ultraviolet to Gamma Ray, Proc. SPIE, 9905, 99052E

Gatti E., Rehak P., 1984, Nuclear Instruments and Methods in Physics Research, 225, 608

Geller M.J., Huchra J.P., 1989, Science, 246, 897

Georgakakis A., Carrera F., Lanzuisi G., et al., 2013, ArXiv e-prints, 1306.2328

George I.M., Arnaud K.A., Pence B., 2007, The Calibration Requirements for Spectral Analysis, Technical Report OGIP Calibration Memo CAL/GEN/92-002, NASA/GSFC

Giacconi R., 1980, Scientific American, 242, 80

Giacconi R., Branduardi G., Briel U., et al., 1979, ApJ, 230, 540

Giacconi R., Gursky H., Paolini F.R., Rossi B.B., 1962, Phys. Rev. Lett., 9, 439

Giacconi R., Kellogg E., Gorenstein P., et al., 1971, ApJ, 165, L27

Giacconi R., Murray S., Gursky H., et al., 1974, ApJS, 27, 37

Giacconi R., Murray S., Gursky H., et al., 1972, ApJ, 178, 281

Heger A., Fryer C.L., Woosley S.E., et al., 2003, ApJ, 591, 288

Henke B.L., Gullikson E.M., Davis J.C., 1993, Atomic Data and Nuclear Data Tables, 54, 181

Hillebrandt W., Kromer M., Röpke F.K., Ruiter A.J., 2013, Frontiers of Physics, 8, 116

Hitomi Collaboration, Aharonian F.A., Akamatsu H., et al., 2016, ArXiv e-prints, 1607.07420

Houck J.C., Denicola L.A., 2000, In: N. Manset, C. Veillet, & D. Crabtree (ed.) Astronomical Data Analysis Software and Systems IX, Astronomical Society of the Pacific Conference Series, 216, 591

Jackson B.D., van Weers H., van der Kuur J., et al., 2016, In: den Herder J.W.A., Taka-

hashi T., Bautz M. (eds.) Space Telescopes and Instrumentation 2016: Ultraviolet to Gamma Ray, Proc. SPIE, 9905, 99052I

Janesick J., Elliott T., Bredthauer R., et al., 1988, In: Golub L. (ed.) X-ray instrumentation in astronomy II, Proc. SPIE, 982, 70

Jansen F., Lumb D., Altieri B., et al., 2001, A&A, 365, L1

Kaastra J., Finoguenov A., Nicastro F., et al., 2013, ArXiv e-prints, 1306.2324

Kauffmann G., Colberg J.M., Diaferio A., White S.D.M., 1999, MNRAS, 303, 188

Kemmer J., Lutz G., 1987, Nuclear Instruments and Methods in Physics Research Section A: Accelerators, Spectrometers, Detectors and Associated Equipment, 253, 365

Kennedy G., 2006, Germany's V-2 Rocket, Schiffer military history, Schiffer Publishing Ltd.

Knoll G., 2010, Radiation Detection and Measurement, John Wiley & Sons

Lam Trong T., 2016, In: den Herder J.W.A., Takahashi T., Bautz M. (eds.) Space Telescopes and Instrumentation 2016: Ultraviolet to Gamma Ray, Proc. SPIE, 9905, 99052G

Lampton M., Margon B., Bowyer S., 1976, ApJ, 208, 177

Lauf T., Andritschke R., 2014, Nuclear Instruments and Methods in Physics Research Section A: Accelerators, Spectrometers, Detectors and Associated Equipment, 762, 142

Lechner P., Andricek L., Heinzinger K., et al., 2006, In: 2006 IEEE Nuclear Science Symposium Conference Record, 3, 1595

Macculi C., Argan A., D'Andrea M., et al., 2016, In: den Herder J.W.A., Takahashi T., Bautz M. (eds.) Space Telescopes and Instrumentation 2016: Ultraviolet to Gamma Ray, Proc. SPIE, 9905, 99052K

Margutti R., Zaninoni E., Bernardini M.G., et al., 2013, MNRAS, 428, 729

Matt G., Perola G.C., 1992, MNRAS, 259, 433

Meidinger N., Eder J., Eraerds T., et al., 2016, In: den Herder J.W.A., Takahashi T., Bautz M. (eds.) Space Telescopes and Instrumentation 2016: Ultraviolet to Gamma Ray, Proc. SPIE, 9905, 99052A

Meidinger N., Eder J., Fürmetz M., et al., 2015, In: Siegmund O.H. (ed.) UV, X-Ray, and Gamma-Ray Space Instrumentation for Astronomy XIX, Proc. SPIE, 9601, 96010H

Mitchell R.J., Culhane J.L., Davison P.J.N., Ives J.C., 1976, MNRAS, 175, 29P

Nandra K., Barcons X., den Herder J.W., et al., 2014, Athena: The Advanced Telescope for High Energy Astrophysics: A mission addressing The Hot and Energetic Universe science theme, `http://www.the-athena-x-ray-observatory.eu/images/AthenaPapers/The_Athena_Mission_Proposal.pdf`

Nandra K., Barret D., Barcons X., et al., 2013, The Hot and Energetic Universe: A White Paper presenting the science theme motivating the Athena+ mission, ArXiv e-prints, 1306.2307

Peille P., Ceballos M.T., Cobo B., et al., 2016, In: den Herder J.W.A., Takahashi T., Bautz M. (eds.) Space Telescopes and Instrumentation 2016: Ultraviolet to Gamma Ray, Proc. SPIE, 9905, 99055W

Planck M., 1901, Annalen der Physik, 309, 553

Planck CollaborationAde P.A.R., Aghanim N., et al., 2016, A&A, 594, A13

Plattner M., Albrecht S., Bayer J., et al., 2016, In: den Herder J.W.A., Takahashi T., Bautz M. (eds.) Space Telescopes and Instrumentation 2016: Ultraviolet to Gamma Ray, Proc. SPIE, 9905, 99052D

Porro M., Bianchi D., De Vita G., et al., 2014, In: Takahashi T., den Herder J.W.A., Bautz M. (eds.) Space Telescopes and Instrumentation 2014: Ultraviolet to Gamma Ray, Proc. SPIE, 9144, 91445N

Predehl P., Andritschke R., Böhringer H., et al., 2010, In: Arnaud M., Murray S.S., Takahashi T. (eds.) Space Telescopes and Instrumentation 2010: Ultraviolet to Gamma Ray, Proc. SPIE, 7732, 77320U

Protassov R., van Dyk D.A., Connors A., et al., 2002, ApJ, 571, 545

Rataj M., Polak S., Palgan T., et al., 2016, In: den Herder J.W.A., Takahashi T., Bautz M. (eds.) Space Telescopes and Instrumentation 2016: Ultraviolet to Gamma Ray, Proc. SPIE, 9905, 990568

Rau A., Nandra K., Aird J., et al., 2016, In: den Herder J.W.A., Takahashi T., Bautz M. (eds.) Space Telescopes and Instrumentation 2016: Ultraviolet to Gamma Ray, Proc. SPIE, 9905, 99052B

Röntgen W.C., 1896, Sonderabbdruck aus den Sitzungsberichten der Würzburger Physik.-medic. Gesellschaft 1895,

Schmid C., 2012, Ph.D. thesis, Friedrich-Alexander-Universität Erlangen-Nürnberg

Schmid C., Smith R., Wilms J., 2013, SIMPUT - A File Format for SIMulation inPUT, `http://hea-www.harvard.edu/heasarc/formats/simput-1.1.0.pdf`

Shull J.M., Smith B.D., Danforth C.W., 2012, ApJ, 759, 23

Sijacki D., Springel V., Di Matteo T., Hernquist L., 2007, MNRAS, 380, 877

Smith R., 2013, SIMX: Event simulator, Astrophysics Source Code Library

Smith S.J., Adams J.S., Bandler S.R., et al., 2016, In: den Herder J.W.A., Takahashi T., Bautz M. (eds.) Space Telescopes and Instrumentation 2016: Ultraviolet to Gamma Ray, Proc. SPIE, 9905, 99052H

Springel V., White S.D.M., Jenkins A., et al., 2005, Nature, 435, 629

Strüder L., Briel U., Dennerl K., et al., 2001, A&A, 365, L18

Tanaka Y., Inoue H., Holt S.S., 1994, PASJ, 46, L37

Turner M.J.L., Abbey A., Arnaud M., et al., 2001, A&A, 365, L27

Ueda Y., Akiyama M., Hasinger G., et al., 2014, ApJ, 786, 104

Ueda Y., Akiyama M., Ohta K., Miyaji T., 2003, ApJ, 598, 886

Urry C.M., Padovani P., 1995, PASP, 107, 803

Uttley P., Cackett E.M., Fabian A.C., et al., 2014, The Astronomy and Astrophysics Review, 22, 72

Volonteri M., Dubois Y., Pichon C., Devriendt J., 2016, MNRAS, 460, 2979

Weisskopf M.C., Tananbaum H.D., Van Speybroeck L.P., O'Dell S.L., 2000, In: Truemper J.E., Aschenbach B. (eds.) X-Ray Optics, Instruments, and Missions III, Proc. SPIE, 4012, 2

Whelan J., Iben, Jr. I., 1973, ApJ, 186, 1007

Wille E., Bavdaz M., Collon M., 2016, In: den Herder J.W.A., Takahashi T., Bautz M. (eds.) Space Telescopes and Instrumentation 2016: Ultraviolet to Gamma Ray, Proc. SPIE, 9905, 990529

Wilms J., Allen A., McCray R., 2000, ApJ, 542, 914

Wilms J., Brand T., Barret D., et al., 2014, In: Takahashi T., den Herder J.W.A., Bautz M. (eds.) Space Telescopes and Instrumentation 2014: Ultraviolet to Gamma Ray, Proc. SPIE, 9144, 91445

Wilms J., Smith S.J., Peille P., et al., 2016, In: den Herder J.W.A., Takahashi T., Bautz M. (eds.) Space Telescopes and Instrumentation 2016: Ultraviolet to Gamma Ray, Proc. SPIE, 9905, 990564

Wölfel S., 2007, Ph.D. thesis, Universität Siegen

Wolter H., 1952, Annalen der Physik, 445, 94

Woosley S.E., Weaver T.A., 1986, ARA&A, 24, 205

Yoshikawa K., Yamasaki N.Y., Suto Y., et al., 2003, PASJ, 55, 879

A Appendix

A.1 Operating Voltages for the SPIX II-Measurements

In the following table, the operating voltages for the two detectors *P05_W81_Q10* and *P05_WS80_Q10* as used for the measurements presented in Chapter 6 are listed.

Table A.1: Operating Voltages for sensors *P05_W81_Q10* and *P05_WS80_Q10* as used in the measurements presented in this thesis.

Voltage Designation	Value [V] (*P05_W81_Q10*)	Value [V] (*P05_WS80_Q10*)
Base Board		
FPGA Baseboard	5.0	5.0
VDDF–switcher	3.0	3.0
GND–switcher	−7.0	−7.0
V_REF	−3.7	−3.7
Veritas		
VSS	−1.7	−1.7
VDD	1.7	1.7
VSSD	−1.7	−1.7
VDDD	1.7	1.7
VSS_Buf	−1.7	−1.7
VDD_Buf	1.7	1.7
V_REF	−0.1	−0.1
DEPFET (Periphery)		
Guard	−20	−20
OS	5.0	5.0
Ch_Sep	−14.5	−15.0
IS	5.0	2.0
MOS–Gate	2.0	1.9
DEPFET (Clocked)	(high/low)	(high/low)
Clear	18.0/−0.15	18.0/−0.3
Clear–Gate	8.5/−1.85	8.5/−2.0
Gate	5.5/−3.3	5.5/−3.0
DEPFET (Source & Drain)		
VSSS	12.3	12.5
Drain	−7.0	−6.5
DEPFET (Backside)		
Vback	−140	−130

Acknowledgements

First of all, I'd like to thank my advisor, Jörn Wilms, for giving me the opportunity to work in astronomy since my Bachelor's thesis and to allow me to become a part of *Athena*'s development team. I am very grateful for him teaching us the methods of clean scientific work and for motivating us to use new methods for data analysis. Furthermore, I'd like to thank him for his support and patience in the case of difficulties.

Secondly, I'd like to thank Norbert Meidinger for the great collaboration, in general for the past three years as well as for providing me with the possibility to perform the measurements for the prototype sensors as presented in this thesis. For the support during this very productive and informative stay at the MPE, I'd like to thank Robert Andritschke, Alexander Bähr, Johannes Müller-Seidlitz and all the others who worked side-by-side in the lab and who included me into the team immediately.

I'd like to thank my present and former colleagues at the Dr. Karl Remeis-observatory for the friendly and productive atmosphere. Christoph Grossberger listened to every problem I encountered during the past years, gave me fruitful input for various kinds of data analysis and helped me with software problems. Thomas Dauser spent the last three years with me working on SIXTE and provided me with support and help for the software development and the instrument studies. Christian Schmid programmed SIXTE, taught me how to use and modify it and always answered my questions about programming and space telescopes. Ingo Kreykenbohm introduced me into astronomical programming at the start of my Bachelor's thesis and ceaselessly provided me with help on this and other topics since then. Together with Fritz-Walter Schwarm and Thomas Dauser, he also manages the computers without which the whole work would not have been possible. My office mates, Ralf Ballhausen, Tobias Hain and Florian Erbesdobler made working in the office a pleasure. I'd also like to thank Michael Wille for his help with background simulations and programming questions in general, as well as Matthias Bissinger for many interesting discussions about light curves and accretion dynamics.

I'd also like to thank all colleagues at other places who supported me in the collaborations for *Athena* and eROSITA. Arne Rau always answered my questions regarding the newest developments at the WFI. Philippe Peille worked together with me on the X-IFU and supported our programming team. I'd like to thank Roland den Hartog and Jelle de Plaa for their collaboration on the X-IFU-simulations. Richard Willingale provided us with the data from the ray-tracing simulations of *Athena*'s mirror system. Hermann Brunner supplied me with new information on eROSITA, and Konrad Dennerl gave me an introduction on the data calibration algorithm for the eROSITA detectors and provided us with calibration files.

A big thank you goes to Macarena Sagredo and Thomas Dauser and Janina Lange who provided me with comments on the draft for this thesis. Last but not least, I'd like to thank Janina Lange and my family for their constant support during the past years.